University of California
Santa Barbara

Structure-Property Relationships in Semiconducting Polymers and Small Molecules Probed by Synchrotron X-ray Methods

A dissertation submitted in partial satisfaction
of the requirements for the degree

Doctor of Philosophy
in
Materials

by

Gregory M. Su

Committee in charge:

Professor Michael L. Chabinyc, Chair
Professor Glenn H. Fredrickson
Professor Rachel A. Segalman
Professor Tresa M. Pollock

December 2015

The Dissertation of Gregory M. Su is approved.

Professor Glenn H. Fredrickson

Professor Rachel A. Segalman

Professor Tresa M. Pollock

Professor Michael L. Chabinyc, Committee Chair

November 2015

Structure-Property Relationships in Semiconducting Polymers and Small Molecules
Probed by Synchrotron X-ray Methods

by

Gregory M. Su

Acknowledgements

There are many people I am grateful for during my Ph.D. Of course, my advisors Profs. Michael Chabinyc and Ed Kramer, and the rest of my committee. Special remembrance for Ed, who passed in December 2014, but was always there for advice and support and made sure his students performed careful, thorough work. Michael has been an incredible mentor, always knowing the important questions to ask and problems to solve, and allowed me the freedom to pursue my interests, which has made graduate school a very enjoyable experience.

I also thank members of the Chabinyc and Kramer groups over the years that have helped me learn, answered questions, been companions during beam times, and friends in general. Additionally, the research scientists, development engineers, and lab managers in the CNSI and MRL shared experimental facilities have been extremely helpful in training and upkeep on relevant equipment. Staff and administrators have, among many other things, processed travel reimbursements and made sure everyone gets paid on time.

I have worked significantly at national user facilities and am especially grateful to the scientists there that have been so helpful and collaborative. David Prendergast at the Molecular Foundry allowed me to utilize computational methods to help with experiments. Beamline scientists, Cheng Wang, Tony Young, and David Kilcoyne among others, who go far above and beyond the requirement to make sure our experiments get done.

My friends in the Santa Barbara area have made the last five years truly memorable. I have been fortunate to enjoy numerous adventures, yes, a large fraction of which were to go climbing, and many of you have caught me when I fell, literally.

Finally, I thank my family which has always been so supportive throughout my life. I could not ask for better!

Curriculum Vitæ

Gregory M. Su

Education

2010 - 2015	Ph.D. in Materials (Expected), University of California, Santa Barbara.
2006 - 2010	B.S. in Chemical Engineering, University of Massachusetts Amherst.

Experience

2010 - 2015	Graduate Student Researcher, Materials Department, University of California, Santa Barbara.
Fall 2011	Teaching Assistant for Materials Department Graduate course 200A –Thermodynamic Foundation of Materials, University of California, Santa Barbara.
Jan - June 2013	Mentor for undergraduate researcher through the Center for Energy Efficient Materials (CEEM), University of California, Santa Barbara.
2011 - 2015	Graduate Students for Diversity in Science, University of California, Santa Barbara.

Awards

2015	American delegate of the 65th Lindau Nobel Laureate Meeting
2015	U.S. Department of Energy Office of Science Graduate Student Research (SCGSR) Program
2014 - 2015	Advanced Light Source Doctoral Fellowship, Lawrence Berkeley National Laboratory
2014	Materials Research Society Fall Meeting Best Presentation Award, Symposium Q: Fundamentals of Organic Semiconductors: Synthesis, Morphology, and Theory
2014 - 2015	UC Santa Barbara Graduate Division Fellowship
2010	NSF Graduate Research Fellowship Program

Selected Publications

G. M. Su, S. N. Patel, C. D. Pemmaraju, D. Prendergast, and M. L. Chabinyc, First-Principles Predictions of X-ray Absorption Spectroscopy for Characterization of Semiconducting Polymers, *In Preparation.*

C-K. Mai, T. Arai, X. Liu, S. L. Fronk, G. M. Su, R. A. Segalman, M. L. Chabinyc, and G. C. Bazan, Electrical Properties of Doped Conjugated Polyelectrolytes with Modulated Density of Ionic Functionalities, *Chem. Commun.*, **2015**, *51*, 17607-17610

S. N. Patel, G. M. Su, C. Luo, M. Wang, L. A. Perez, D. A. Fischer, D. Prendergast, G. C. Bazan, A. J. Heeger, M. L. Chabinyc, and E. J. Kramer, NEXAFS Spectroscopy Reveals the Molecular Orientation in Blade-coated Pyridal[2,1,3]thiadiazole-containing Conjugated Polymer Thin Films, *Macromolecules*, **2015**, *48*, 6606-6616

C. W. Pester, J. E. Poelma, B. Narupai, S. N. Patel, G. M. Su, T. E. Mates, Y. Luo, C. K. Ober, C. J. Hawker, and E. J. Kramer, Ambiguous anti-fouling surfaces: Facile synthesis by light-mediated radical polymerization, *J. Polym. Sci. A Polym. Chem.*, **2015**, DOI: 10.1002/pola.27748

G. M. Su, E. Lim, E. J. Kramer, and M. L. Chabinyc, Phase Separated Morphology of Ferroelectric-Semiconductor Polymer Blends Probed by Synchrotron X-ray Methods, *Macromolecules*, **2015**, *48*, 5861-5867

G. M. Su, E. Lim, A. R. Jacobs, E. J. Kramer, and M. L. Chabinyc, Polymer Side Chain Modification Alters Phase Separation in Ferroelectric - Semiconductor Polymer Blends for Organic Memory, *ACS Macro Lett.*, **2014**, *3*, 1244-1248

C-K. Mai, R. A. Schlitz, G. M. Su, D. Spitzer, X. Wang, S. Fronk, D. G. Cahill, M. L. Chabinyc, and G. C. Bazan, Optimizing Thermoelectric Properties of Self-Doped Narrow Band Gap Conjugated Polyelectrolytes via Side Chain Modifications, *J. Am. Chem. Soc.*, **2014**, *136*, 13478-13481

G. M. Su, T. V. Pho, N. D. Eisenmenger, C. Wang, F. Wudl, E. J. Kramer, and M. L. Chabinyc, Linking Morphology and Performance of Organic Solar Cells Based on Decacyclene Triimide Acceptors, *J. Mater. Chem. A*, **2014**, *2*, 1781-1789

Y. Huang, X. Liu, C. Wang, J. T. Rogers, G. M. Su, M. L. Chabinyc, E. J. Kramer, and G. C. Bazan, Structural Characterization of a Composition Tolerant Bulk Heterojunction Blend, *Adv. Energy Mater.*, **2014**, *4*, 1301886

T. V. Pho, F. M. Toma, B. J. Tremolet de Villers, S. Wang, N. D. Treat, N. D. Eisenmenger, G. M. Su, R. C. Coffin, J. D. Douglas, J. M. J. Frchet, G. C. Bazan, F. Wudl, and M. L. Chabinyc, Decacyclene Triimides: Paving the Road to Universal Non-Fullerene Acceptors for Organic Photovoltaics, *Adv. Energy Mater.*, **2014**, *4*, 1301007

N. D. Eisenmenger, G. M. Su, G. C. Welch, C. J. Takacs, G. C. Bazan,

E. J. Kramer, and M. L. Chabinyc, Effect of bridging atom identity on the morphology of solution-processed small molecule bulk heterjunction photovoltaics, *Chem. Mater.*, **2013**, *25*, 1688-1698

M. A. Brady, G. M. Su, and M. L. Chabinyc, Recent Progress in the Morphology of Bulk Heterojunction Photovoltaics, *Soft Matter*, **2011**, *7*, 11065-11077

G. M. Su, K. Best, T. Ranganathan, T. Emrick, and A. J. Crosby, Tailored Nanoparticles for Enhancing Polymer Adhesion, *Macromolecules*, **2011**, *44*, 5256-5261

Fields of Study

Major Field: Organic Electronics

Structural characterization of organic semiconductors for solar cells, memory devices, and transistors (Professors Michael L. Chabinyc and Edward J. Kramer)

First-principles predictions of X-ray absorptions spectra of organic semiconductors (Professor Michael L. Chabinyc and David Prendergast)

Abstract

Structure-Property Relationships in Semiconducting Polymers and Small Molecules
Probed by Synchrotron X-ray Methods

by

Gregory M. Su

Organic semiconductors are an exciting class of materials that have potential to produce low-cost, printable, and flexible electronic devices. Moving to the next generation of organic semiconductors that will result in greater efficiency requires advancements in the areas of materials chemistry, molecular assembly, predictive modelling, and device optimization. Here, we focus on morphology and demonstrate how it is linked to each of these areas. Understanding the connections among chemistry, thin film microstructure, and charge transport remains a major challenge in the field. We examined materials systems relevant to organic solar cells, memory devices, and transistors, with a focus on synchrotron-based X-ray techniques. For a blend of a polymer and small molecule, applicable to solar cells, control of molecular orientation in the small molecule is especially important for non-fullerene based molecules that exhibit anisotropic charge transport. In ferroelectric-semiconductor polymer blends used in organic memory, improved control over phase separation length scales is achieved by altering the chemistry of the semiconducting polymer to tune polymer-polymer interactions. Complementary simulations can facilitate characterization of organic semiconductors. First-principles predictions of X-ray absorption spectroscopy are applied to semiconducting polymers, and prove critical for understanding complex experimental data related to molecular orientation and electronic structure in general. Overall, these studies provide insights into key factors that should be considered in the development of new organic semiconductors.

Contents

List of Figures

Chapter 1

Introduction

Organic-based semiconducting materials, including polymers and small molecules, are attractive building blocks for a variety of electronic applications as they provide the potential for inexpensive and flexible devices that can be fabricated via large-area processing methods such as roll-to-roll printing. Efforts in recent years have focused on developing organic semiconductors to be the active component in light-emitting diodes (LEDs), transistors, solar cells, thermoelectrics, and memory elements, and significant progress has been made on many of these fronts [1, 2, 3, 4, 5, 6, 7]. Typical organic semiconductors consist of a carbon-based conjugated core, which imparts semiconducting properties, and pendant side chains that improve solubility, and affect intermolecular packing. One advantage of these materials is that synthetic procedures allow them to be easily functionalized to tune optoelectronic and physical properties for specific applications.

The development and advancement of organic semiconductor materials involves efforts from many scientific angles, including synthesis of new materials, computational theory and modelling, characterization of morphology and microstructure, and device fabrication and optimization. Each of these areas is very involved in its own right, and progress in advancing organic semiconductors requires a multidisciplinary approach. Although each of these aspects is important, this work focuses on characterizing and understanding the thin film morphology of semiconducting polymers, small molecules, and their complex blends, which is critically linked to charge transport and device performance.

1.1 Importance of Morphology in Organic Electronics

Semiconducting polymers, polymer:polymer, and polymer:small molecule blends tend to form complicated morphologies in solid-state thin films, often consisting of multiple phases, amorphous and crystalline regions, and vertical stratification. The final blend morphology of these solution-cast thin films is affected by many parameters, from molecular aspects such as conjugation length, planarity, and side chain architecture [8], to processing conditions including spin-coating parameters, substrate surface properties, and solvents [9, 10, 11]. Nevertheless, in order for devices to function properly, charge carriers must travel long distances between electrodes, for example, laterally in a transistor geometry or vertically through the film thickness for solar cells. It is well known that various aspects of the microstructure, for example, crystallinity and crystallite orientation, phase separation, and surface segregation can have a significant impact on the ability of charges to separate and/or transport through the film [12]. The ability to characterize, understand, and control the morphology of organic semiconductor thin films has remained one of the main challenges in the field.

Most organic semiconductors exhibit anisotropic charge transport properties, both for a single molecule or polymer chain and within ordered or crystalline domains [13]. As a result, the ability to probe and control molecular orientation is essential. Charge

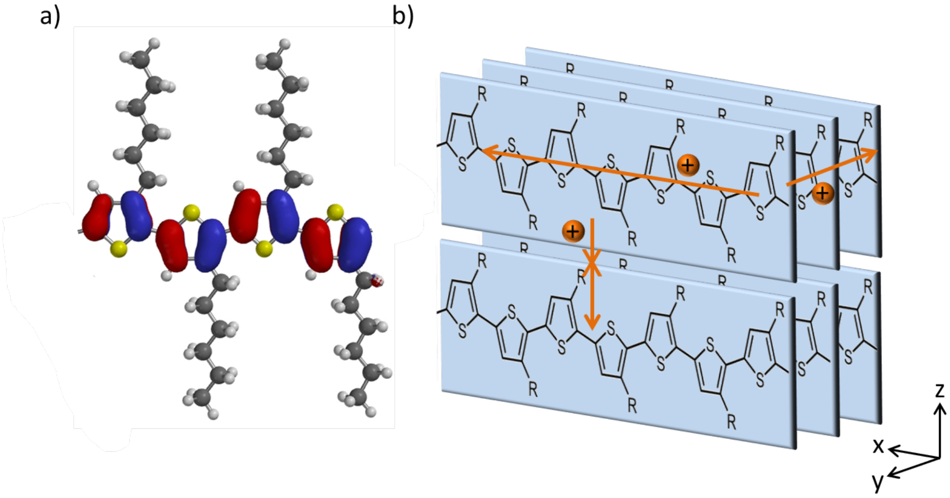

Figure 1.1: Model structure and packing in a thiophene-based polymer reveals that charge transport is good along the conjugated backbone and the $\pi-\pi$ stacking direction, but blocked along the side chain stacking extent.

transport is typically best along the conjugated backbone (for the case of polymers), or between adjacent molecules via cofacial $\pi-\pi$ stacking. Side chains are typically insulating hydrocarbons, so charge transport is effectively blocked along the side chain stacking extent. An example for a thiophene-based polymer is shown in Figure 1.1. For polymers of sufficiently high molecular weight, tie-chains are thought to be critical for allowing charges to travel among separated aggregated domains [13]. Blends of two components are required for certain organic electronic devices, adding complexities to the active layer morphology, including phase separation length scales, domain purity and connectivity, and interfacial segregation. All of these aspects also impact charge transport and device performance.

1.2 Overview of Synchrotron X-ray Techniques

It is important to be able to non-invasively characterize the microstructure and molecular ordering over a large range of length scales (from Angstroms to many micrometers).

Synchrotron-based X-ray spectroscopy, microscopy, and scattering provide a suite of complimentary techniques that can probe this span of length scales [14]. The work presented here focuses on how synchrotron X-ray methods, in combination with other characterization, device properties, and first-principles methods, can reveal important insights that link together molecular structure, morphology, and charge transport. The main techniques employed in this work are near edge X-ray absorption fine structure, scanning transmission X-ray microscopy, resonant soft X-ray scattering, and grazing incidence X-ray scattering.

1.2.1 Near Edge X-ray Absorption Fine Structure (NEXAFS)

Near-edge X-ray absorption fine structure (NEXAFS) spectroscopy is a technique based on transitions of core-shell electrons to unoccupied molecular orbitals. It is sensitive not only to specific elements in a sample, but also the local structure and bonding.

In the soft X-ray regime (∼50 to 2000 eV), light can either scatter or undergo photoabsorption/ionization with atoms. These two major interactions are represented by the complex atomic scattering factor: $f = f_1 + if_2$, and in this energy range, absorption (f_2) is much more likely. Both f_1 and f_2 undergo large changes near the absorption edges of different elements [15]. However, besides the obvious change in absorption due to the photo-ionization threshold of a specific element, electrons can undergo many other transitions to empty states near the ionization edge, resulting in a highly featured energy-dependant absorption spectra.

NEXAFS spectroscopy probes transitions of core electrons to antibonding orbitals. A transition to an unoccupied state will occur if the incoming photon has an energy that exactly matches the energy difference between the two states. For these many-atom molecules, there are numerous unoccupied states near the ionization threshold.

The peaks in NEXAFS spectra essentially correspond to transitions of a core electron to these empty states, as shown in Figure 1.2. For most organic semiconductors, the lowest energy feature in the carbon K edge regime corresponds to a transition to a π^* anitbonding orbital, which sits below the ionization potential due to electron-hole Coulomb interaction [16]. Transitions to σ^* states are found at higher energies, often above the vacuum level.

For surface-sensitive NEXAFS measurements, absorption is determined by detection of either a fluorescence photon or an Auger electron. When the incident X-ray beam hits the sample, a core electron is excited out of its original energy level (photoelectron). This produces a core hole. An electron at a higher occupied level can drop down to fill the core hole, releasing energy radiatively in the form of a fluorescence photon or non-radiatively as an Auger electron. Both the fluorescence photon and Auger electron are direct measures of X-ray absorption. In fluorescence yield (FY) mode, the fluorescence photons are detected. This detection mode is better suited for looking at liquid samples and into the bulk, up to about 100 nm below the surface. Due to the limited kinetic energy of emitted Auger electrons, only those near to the surface are able to escape and be picked up by the detector. In the total electron yield (TEY) mode, all electrons that emerge from the surface are detected. Alternatively, in partial electron yield (PEY), a screening bias is placed in front of the detector to repel lower kinetic energy electrons, meaning only those emerging from the outermost surface layer ($\sim$2 nm) are detected. Degree of surface sensitivity can be tuned by changing the bias [17].

NEXAFS can probe molecular orientation due to the inherent polarization of the X-ray beam and the tunability of the incident angle. Organic semiconductors often have anisotropic molecular orbitals and transitions to these orbitals can have dipole moments in a specific direction [18, 19]. A π^* transition can typically be described by a vector that is perpendicular to the conjugated ring plane. The intensity of this peak will be greatest

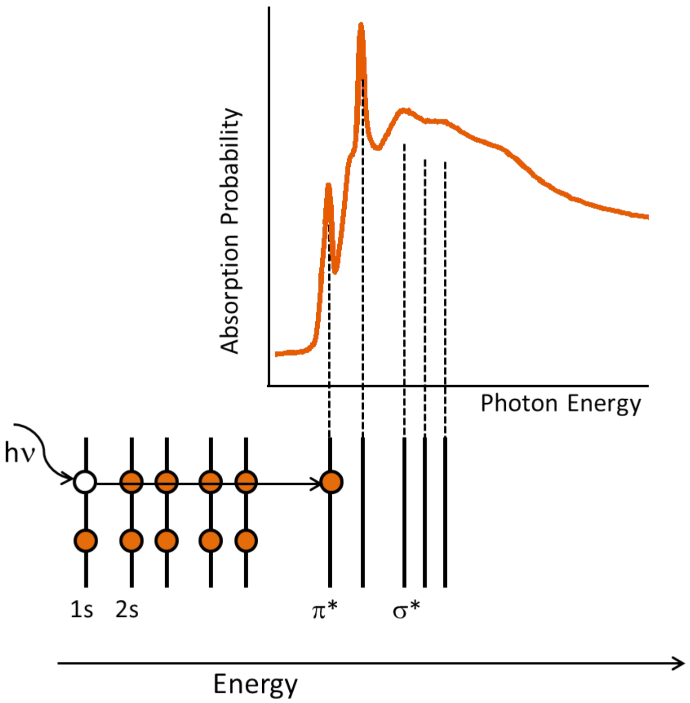

Figure 1.2: Schematic showing how peaks in a NEXAFS spectra correspond to transitions of core electrons to unoccupied orbitals.

when the electric field vector of the incoming X-ray is directionally aligned with the transition dipole moment vector of the π^* transition, and lowest when these two vectors are perpendicular. Hence, overall molecular orientation can be probed by observing the change in intensity of a specific peak as a function of incident angle.

1.2.2 Transmission Soft X-ray Microscopy and Resonant Scattering

Resonant soft X-ray scattering (RSoXS) is a relatively novel technique for probing structure of organic materials. RSoXS combines the abilities of small-angle scattering and the energy-dependent absorption properties obtained from NEXAFS to enhance contrast and selectivity when studying organic semiconductors [20, 21, 14]. Hard X-rays probe differences in electron density, which makes studying blends of similar systems, such as a

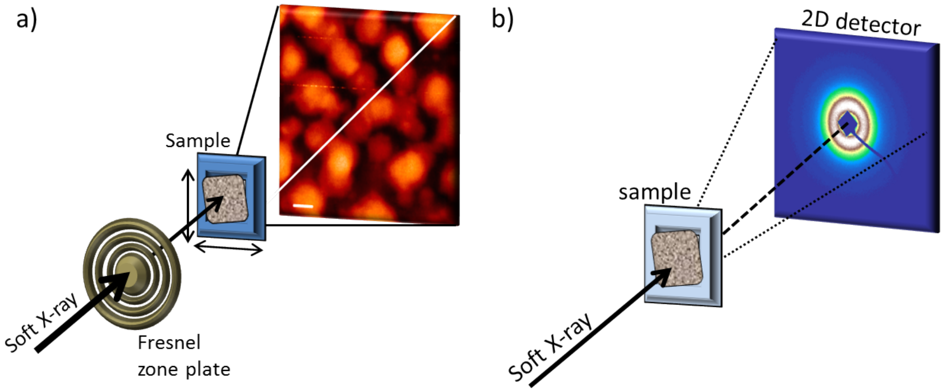

Figure 1.3: Schematic showing the experimental geometry for (a) scanning transmission X-ray microscopy and (b) transmission resonant X-ray scattering.

polymer/polymer blend, difficult. RSoXS utilizes soft X-rays, where the scattering contrast factor, $\Delta f_1^2 + \Delta f_2^2$, is typically dominated by the absorptive part, f_2. Furthermore, since the incident X-ray energy is tunable, one can select an energy that allows for either greatest overall contrast or scattering dominated by one component in a blend. Since NEXAFS tells how f_2 of a material depends on energy, it is essential to have NEXAFS data of the different components in a blend to better understand RSoXS data at a given energy. It is important to note that RSoXS does not probe just crystalline regions, but amorphous ones as well. At certain transition resonances, RSoXS is sensitive to molecular orientation, allowing for contrast even in a single component film [22]. The enhanced contrast attainable with soft X-rays allows samples to be studied in transmission, which can ease data analysis.

In scanning transmission X-ray microscopy (STXM), the incoming X-ray beam is focused down to a small point (∼30 nm diameter) with a Fresnel zone plate and scanned through the sample and the transmitted intensity recorded (Figure 1.3) [23, 24]. If the sample is translated, then a spatial map can be achieved. By tuning the X-ray energy to where absorption is dominated by one component, in-plane spatial composition maps of blends can be achieved.[25] Since this technique is done in transmission, vertical

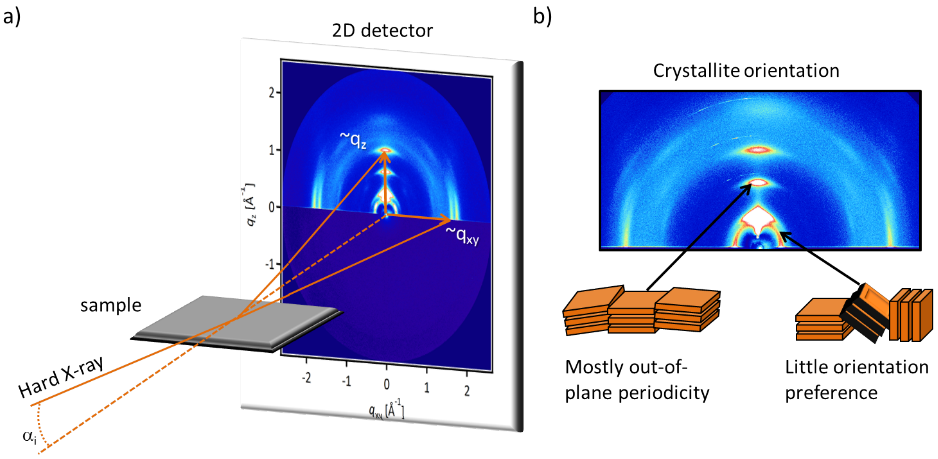

Figure 1.4: Schematic showing the experimental geometry for grazing incidence X-ray scattering with a two-dimensional detector

composition changes are difficult to attain, although three-dimensional reconstruction with tomography is possible.[26]

1.2.3 Grazing Incidence Wide Angle X-ray Scattering

Grazing Incidence Wide Angle X-ray Scattering (GIWAXS) is one of the most common X-ray techniques to probe order and crystallinity in organic semiconductor thin films [14, 12]. GIWAXS is typically done with hard X-rays, and probes length scales from a few Angstroms to a few nanometers within crystalline regions. WAXS can be done with point detectors, usually to obtain in-plane or out-of-plane information, but it is common to use a two-dimensional (2D) area detector which allows for rapid data collection over a range of scattering angles allowing for simultaneous viewing of scattering that originates from both out-of-plane and in-plane periodicities. However, 2D data collection comes at the expense of reduced accuracy and resolution. Incident X-rays are diffracted by periodic planes of atoms or molecules, which cause periodicities in electron density. For semicrystalline organic semiconductors, these length scales are relevant to probing the distances between adjacent molecules in the crystalline regions. 2D GIWAXS is typically used to obtain information on periodic spacings from the peak positions, correlation lengths or crystallite size from the peak widths, and crystallite orientation, or texture, based on intensity distributions [14, 27].

1.3 Permissions and Attributions

1. The content of chapter 2 is taken from previously published material. G. M. Su, T. V. Pho, N. D. Eisenmenger, C. Wang, F. Wudl, E. J. Kramer and M. L. Chabinyc, *J. Mater. Chem. A*, **2014**, *2*, 1781, DOI: 10.1039/C3TA14839D - Reproduced by permission of The Royal Society of Chemistry

2. Portions of chapter 3 are reprinted with permission from G. M. Su, E. Lim, A. R. Jacobs, E. J. Kramer, and M. L. Chabinyc, *ACS Macro Lett.*, **2014**, *3*, 1244-1248. Copyright 2014 American Chemical Society. Remaining portions of chapter 3 are reprinted with permission from G. M. Su, E. Lim, E. J. Kramer, and M. L. Chabinyc, *Macromolecules*, **2015**, *48*, 5861-5867. Copyright 2015 American Chemical Society.

3. Portions of chapter 4 are reprinted with permission from S. N. Patel, G. M. Su, C. Luo, M. Wang, L. A. Perez, D. A. Fischer, D. Prendergast, G. C. Bazan, A. J. Heeger, M. L. Chabinyc, and E. J. Kramer, **2015**, *48*, 6606-6616. Copyright 2015 American Chemical Society.

   Other portions of chapter 4 will be submitted as a manuscript: G. M. Su, S. N. Patel, C. D. Pemmaraju, D. Prendergast, and M. L. Chabinyc, First-Principles Predictions of X-ray Absorption Spectroscopy for Characterization of Semiconducting Polymers, *In Preparation.*

Chapter 2

Linking Morphology and Performance of Organic Solar Cells Based on Decacyclene Triimide Acceptors

2.1 Introduction

Photovoltaics based on conjugated organic polymers and small molecules have been the focus of intense study in recent years. Technological progress has resulted in organic photovoltaics (OPVs) with high power conversion efficiencies (PCEs). To date, nearly all OPVs utilize a fullerene derivative such as [6,6]-phenyl-C_{61}-butyric acid methyl ester (PCBM) as the electron accepting material, and these acceptors have been the champion performers resulting in PCEs greater than 10% [28]. Acceptors such as PCBM have the advantages of large electron affinity and good electron mobility [29]. However, they suffer from weak absorption in the visible region of the solar spectrum compared to many donors and a large electron affinity that limits the open circuit voltage (V_{OC}). Therefore, there is an impetus to develop non-fullerene based materials that are simpler to synthesize and have a more tunable energy bandgap to complement fullerenes as acceptor molecules.

Although there has been significant progress in non-fullerene based bulk heterojunction (BHJ) solar cells [30], non-fullerene polymer:small molecule OPVs still typically have PCEs of about 1% - 2% [31, 32, 33, 34], and have only recently reached ∼4% [35]. All-polymer based solar cells have also seen noticeable improvements reaching efficiencies of about 4% as well [36, 37, 38, 39]. Geometrically, these materials are different from fullerenes because they are not nearly spherically symmetric molecules. Therefore, the self-assembly and transport properties of non-fullerene acceptors are fundamentally different. This provides unique opportunities to study charge generation originating from light absorption in the acceptor and charge transfer to the donor [40, 41, 42]. In order to fabricate more efficient devices, it is essential to better understand the assembly and morphological properties of this class of materials, and to date, there is a very limited understanding on the link between variation in photovoltaic performance and structural changes in non-fullerene acceptors compared to the extensive number of reviews focusing on the P3HT:PCBM system [12, 43, 29, 44, 45].

Here, we show how performance in non-fullerene based solar cells is closely linked to molecular orientation and organization. The acceptor in this study is based on a decacyclene triimide core functionalized with octyl side groups, which will be referred to as DTI. The molecular structure is shown in Figure 2.1. The synthesis and initial performance of a BHJ solar cell consisting of a blend of DTI and the well-studied polymer, poly(3-hexylthiophene) (P3HT), were recently reported [31]. Decacyclene and DTI have been shown to form stacked columns with the π-π stacking direction down the length of the column [31, 46, 47]. Large steric interactions that lead to significant twisting of the molecular core can disrupt packing, as shown recently for truxenone-based acceptors

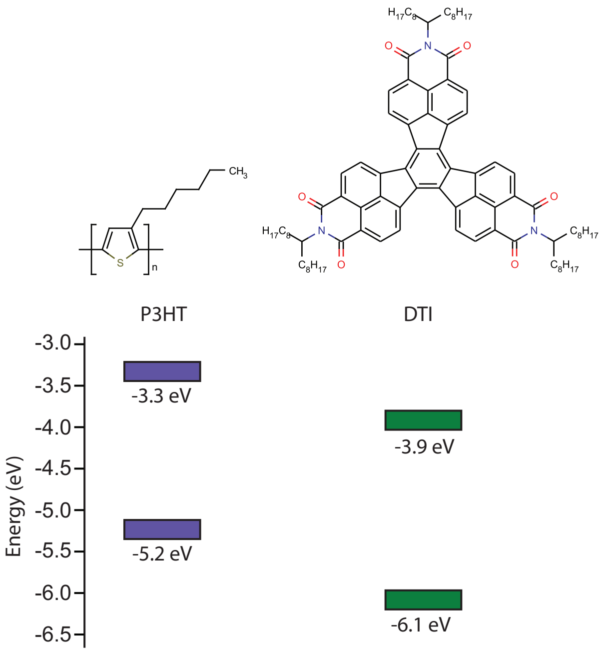

Figure 2.1: Molecular structures and approximate highest occupied molecular orbital and lowest unoccupied molecular orbital energy levels for P3HT and DTI.

[34]. However, both decacyclene and DTI have a gently twisted propeller geometry (see Figure A.1) that maintains good π-π stacking among molecules. It is expected that there is sufficient orbital overlap and charge conduction in the π-π stacking direction, but limited conduction perpendicular to the π-π stacking direction. These anisotropic transport properties of DTI make it an ideal material to study the interplay between molecular orientation and solar cell performance.

It is known that polycyclic aromatic hydrocarbons and discotic columnar liquid crystals, similar to decacyclene, often pack into columns that can arrange hexagonally [48, 49]. Techniques including thermal treatment and altering growth kinetics have been used to impart control over the orientation of columns between homeotropic (columns perpendicular to the substrate) and planar (columns in-plane with the substrate) arrangements [50, 51, 52]. Further studies have shown that discotic liquid crystals have the capability for high time-of-flight mobilities on the order of 10^{-1} $cm^2V^{-1}s^{-1}$ [53, 54].

In order for such discotic materials to properly transport charge in OPVs, they must maintain satisfactory orientation and charge carrier properties when blended with a second material. Blending a columnar discotic liquid crystalline material with an amorphous polymer can lead to geometric confinement that alters the spatial correlation lengths of the columnar structures, hence changing their optical and electronic transport properties [55]. Although blends with amorphous polymers reveal interesting physics, OPVs require these discotic materials to be mixed with semiconducting polymers or small molecules and maintain proper electrical function. This has been shown for a hexabenzocoronene based discotic liquid crystal that self-assembles into vertical stacks when blended with a perylene dye and exhibits a photovoltaic response with a power efficiency maximum of 1.95% and an external quantum efficiency over 34% at 490 nm [48]. Also, solar cells consisting of a trisubstituted decacyclene acceptor and poly[2-methoxy-5-(2'-ethylhexyloxy)-1,4-phenylenevinylene] (MEH-PPV) as the donor have been demonstrated [56]. These devices attained a high V_{OC} (1.3 V), but the overall PCE of 0.14% under 500 nm monochromatic light was limited due to a poor short circuit current (J_{SC}) of 3.6 μAcm^{-2} and a fill factor (FF) of 0.22.

DTI also shows promise as a successful discotic-based photovoltaic material. The P3HT:DTI solar cells studied here exhibit good as-cast performance (PCE = 1.6%) with high FF. Interestingly, the efficiency degrades significantly when thermally annealed. P3HT:PCBM-based devices, on the other hand, can reach efficiencies up to $\sim$5% with thermal treatment [29, 57]. Soft X-ray spectroscopy and grazing incidence scattering reveal that thermal annealing induces DTI to orient and assemble such that vertical charge transport is hindered, limiting solar cell performance. These results provide insight into the fundamental relations between morphology and electronic performance in non-fullerene acceptors and the subtleties and important parameters involved in designing such materials.

2.2 Experimental

DTI was synthesized as reported previously [31], and P3HT obtained from Rieke Metals (Sepiolid P200). All solutions were prepared with a total concentration of 20 mg mL^{-1} in o-dichlorobenzene and stirred at 80 °C. Thin films were prepared by spin-casting at 1000 rpm for 60 s and then 2000 rpm for 10 s. Near edge X-ray absorption fine structure (NEXAFS) spectroscopy was performed at beamling U7A at the National Synchrotron Light Source (NSLS), grazing incidence wide angle X-ray scattering (GIWAXS) at beamline 11-3 at the Stanford Synchrotron Radiation Lightsource (SSRL), and resonant soft X-ray scattering (RSoXS) at beamline 11.0.1.2 at the Advanced Light Source (ALS). Further experimental details on device fabrication and testing and characterization methods are provided in Appendix A.

2.3 Results and Discussion

2.3.1 Thermal Annealing Reduces Solar Cell Performance

Many organic solar cells require thermal annealing to improve efficiency, however, thermal annealing greatly reduces the performance of P3HT:DTI-based solar cells. Here, we focus on how this can be understood through changes in blend morphology. First, it is of interest to determine directly how thermal treatment influences solar cell performance. Conventional P3HT:DTI-based BHJ solar cells consisting of a PEDOT:PSS hole transport layer and LiF/Al top contacts exhibited a respectable PCE of 1.6% resulting from a J$_{SC}$ of 4.87 mA cm^{-2}, a V$_{OC}$ of 0.58 V, and a FF of 0.57. Interestingly, annealing at 120 °C, a temperature chosen because it is above the thermal transitions of DTI but below the melting point of P3HT, causes a detrimental decrease in performance (PCE $\approx$ 0.3%), as shown in Figure 2.2a. Annealing at various other temperatures in the range of 50 °C

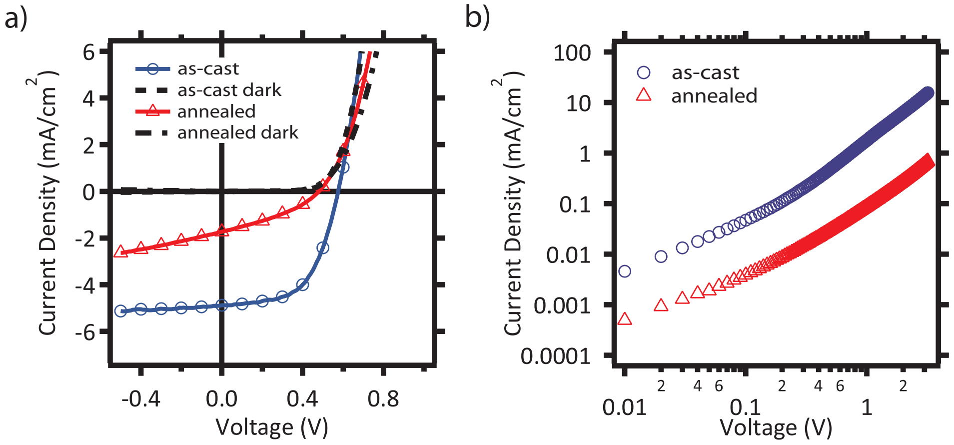

Figure 2.2: (a) Current density vs. voltage plot for an as-cast P3HT:DTI solar cell (blue curve) and a solar cell annealed at 120 °C for 20 min (red curve). The dark current curves for the as-cast and annealed devices are shown with the dotted and dotted-dashed lines, respectively. (b) Current density vs. voltage plot taken in the dark for a P3HT:DTI electron-only device. The as-cast device is given by the blue circles, and the annealed device by the red triangles.

to 120 °C also results in significant drops in PCE (Figure A.2). This is in contrast to P3HT:PCBM solar cells which typically require thermal annealing to optimize efficiency [58, 29]. In fact, many of the previously reported non-fullerene acceptors require thermal annealing to optimize efficiency with P3HT [59, 60, 32, 61]. Additionally, the current-voltage (J-V) characteristics of an electron-only device (Al/P3HT:DTI/Ca/Al) show that the electron current is much lower, about one order of magnitude, in the annealed device (Figure 2.2b). Also, the electron mobility dropped from about 4.1×10^{-6} $cm^2V^{-1}s^{-1}$ in the as-cast film to about 1.8×10^{-7} $cm^2V^{-1}s^{-1}$ in the annealed film. However, no such decrease in the hole current is observed (Figure A.12). This suggests that it is changes in the morphology of DTI acceptor molecules that are mostly responsible for the decreased performance upon annealing.

Despite the drastic decrease in the performance of thermally annealed solar cells, photoluminescence (PL) quenching experiments suggest no appreciable decrease in charge transfer from P3HT to DTI upon annealing, and even a significant improvement in charge transfer from DTI to P3HT (greater degree of PL quenching) after annealing (Figure A.5). The small decrease in charge transfer from P3HT to DTI upon annealing is likely a result of slightly larger P3HT crystallites and suggests no extensive change in the exciton diffusion length within P3HT. Conversely, the drastic improvement in charge transfer from DTI to P3HT after annealing indicates a potential change in the exciton diffusion length in DTI, which has been shown to be quite large in ordered discotic liquid crystals along the transport direction [62]. Energy transfer is also possible since the emission of DTI overlaps with the absorption of P3HT. Furthermore, it is reasonable to expect good exciton splitting at a P3HT-DTI interface if the molecules adopt a cofacial alignment to maximize electronic interactions, and these interfacial interactions may improve in annealed films. Nevertheless, these PL results also point toward changes in morphology as the main reason for hindered charge transport and reduced efficiency in annealed solar cells.

2.3.2 Thermal Annealing has Limited Effect on Vertical Stratification

Considering the severe decrease in photovoltaic performance upon thermal annealing, it is important to determine if significant changes in the vertical segregation of P3HT:DTI blends occurs. For blends of flexible polymers, surface segregation depends strongly on the surface energy of the polymers [63, 64, 65]. It is known that vertical phase segregation can occur in polymer-small molecule blends with a preference of one material to segregate to the film/air or film/substrate interface. Recent studies have shown that in a blend of a semiconducting small molecule and a binder polymer, the segregation of the small molecule to either the film/air, the film/substrate or both interfaces can be tuned. This depends on the polymer molecular weight and the type of polymer, where effects such as confinement entropy, interaction energy, and solidification could all play a role [66, 67]. Furthermore, the presence of an insulating polymer does not necessarily reduce the charge transport capabilities of a semiconducting polymer, and can even enhance it [68, 69]. Vertical segregation could potentially be harmful to charge collection in solar cells. An excess of the electron transport material near the hole-collecting interface may reduce device characteristics. An excess of the hole transport material at the electron-collecting interface may also limit performance, but is potentially less detrimental [70]. However, the overall effects of vertical phase segregation in BHJ solar cells are not very well understood, and in some cases may not result in significant changes in performance [71, 72].

To examine the vertical profile in these materials, depth profiling dynamic secondary ion mass spectrometry (DSIMS) was performed on as-cast and annealed P3HT:DTI blends. P3HT can be tracked in the active layer through the $^{34}S^{-}$ (m/z = 34) mass fragment, since sulfur is not present in DTI, and DTI is tracked with the CN^{-} (m/z = 26) ion. Figure 2.3 shows the vertical profile of the P3HT:DTI active layer region and underlying Si/PEDOT:PSS substrate. A 150 nm polystyrene films was floated on top of the active layer to allow the O_2^+ beam to establish a steady-state damage profile before the top interface of the blend is reached. The etch rate is estimated to be ∼0.45 nm/s based on the initial thickness of the polystyrene film. It should be noted that the absolute intensity of the CN^{-} signal and the $^{34}S^{-}$ signal are not directly related since the formation probability of CN^{-} is much higher than $^{34}S^{-}$.

The DSIMS data do not reveal extensive changes in the vertical composition profile between as-cast and annealed films. Looking at the as-cast film, there is a very slight excess of P3HT at the film surface relative to the amount of P3HT in the interior of the film. There also is a greater excess of P3HT at the buried interface between the active layer and the PEDOT:PSS layer. Interestingly, the profile of DTI suggests that it is

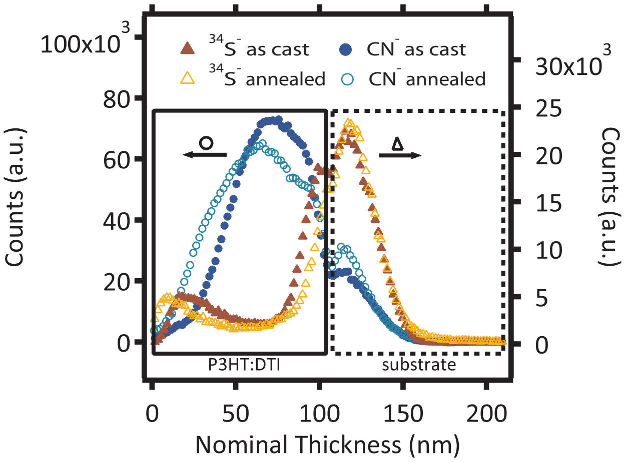

Figure 2.3: Depth profiling DSIMS data for as-cast and annealed (120 °C) P3HT:DTI blend films. The $^{34}S^-$ signal (triangles) corresponds to P3HT and its intensity is plotted on the right axis. DTI is tracked through the CN^- signal (circles) with corresponding intensity plotted on the left axis. The boxed regions indicate approximately where the P3HT:DTI film and underlying Si/PEDOT:PSS substrate reside.

mostly concentrated in the bottom half of the film, without significant excess close to either interface relative to the bulk.

The annealed film exhibits an overall similar profile as the as-cast one. There is still a very slight excess of P3HT at the film/air interface, however there is less of an excess at the BHJ/PEDOT:PSS interface. Correspondingly, there is a slight shoulder in the DTI profile toward the BHJ/PEDOT:PSS interface suggesting there is some additional DTI at the bottom of the film compared to the as-cast case. As alluded to earlier, this vertical segregation profile may reduce charge extraction, but the change in vertical composition is not significant enough for it to be a major cause for the limited performance in annealed devices.

The surface topography of the blend films determined from atomic force microscopy (AFM) shows little change with annealing besides a slight increase in root mean squared (rms) roughness from about 2.1 nm to 2.8 nm for the as-cast and annealed films, respectively (Figure A.3). However, the tendency of the alkyl side chains of both components to inhabit the film/air interface to minimize surface energy could lead to similar film surface structures.

Previous work on polymer-small molecule blends suggests that small molecules tend to segregate to interfaces. However, this can be suppressed by using a semicrystalline polymer with fast crystallization [66]. It is possible that a similar phenomenon is occurring in the P3HT:DTI system where P3HT crystallizes before DTI. This is evident because the crystallization onset temperature of P3HT does not increase when DTI is introduced (Figure A.20), which would be expected if DTI acted as a nucleating agent [73].

2.3.3 Changes in Molecular Orientation and Domain Size Reduce Solar Cell Performance

Considering the geometry and stacking motif of DTI, where good charge transport is possible in the π-π stacking direction, it is reasonable to expect that the orientation of these columnar structures would have a direct impact on electron transport and efficiency. Here, we use a combination of near edge X-ray absorption fine structure (NEXAFS) spectroscopy and X-ray scattering to elucidate the effects of thermal annealing on molecular orientation and order. NEXAFS utilizes polarized soft X-rays where the incident energy can be tuned to specific atomic transitions [15]. Overall molecular orientation can be determined by examining the intensity dependence as a function of incident angle for a specific transition [15, 16, 74, 75, 76, 77, 17]. The application of NEXAFS to examine the tilt of the conjugated core in organic semiconductors has proven to be successful [78, 79, 14, 80, 81].

Here, we focus on molecular orientation of as-cast and annealed P3HT:DTI blends, relevant to photovoltaic devices. Similar trends in molecular orientation were observed for

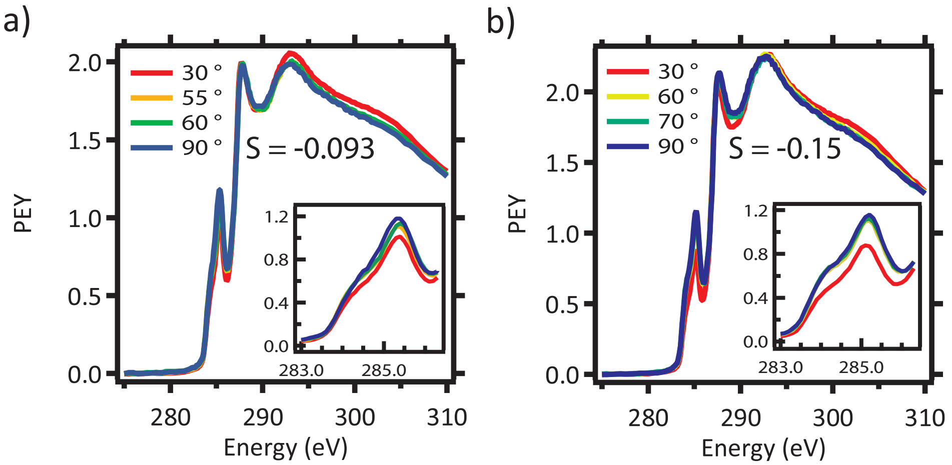

Figure 2.4: Partial electron yield carbon 1s NEXAFS spectra taken at various incident angles for a) an as-cast P3HT:DTI film and b) a P3HT:DTI film annealed at 120 °C. The insets depict a zoom-in of the π^* transitions near 285 eV. The value of the orientation order parameter, S, is indicated.

the bulk of the film, determined from the fluorescence yield (FY) data, as for the surface-sensitive partial electron yield (PEY) data presented here. FY data and orientation analysis for pristine DTI films are shown in Figures A.9 and A.10. PEY data for as-cast and annealed (120 °C) films of P3HT:DTI blends taken at various incident angles are shown in Figure 2.4. In both cases, it is evident that the intensity of the C 1s $\rightarrow \pi^*$ transition near 285 eV increases and is greatest at an incident angle of 90°. However, this effect is stronger in the annealed film. In this experimental geometry, 90° corresponds to the electric field vector in-plane with the substrate surface (incident X-ray normal to the substrate surface). This result suggests that the 1s $\rightarrow \pi^*$ transition vector is mostly parallel to the substrate. The average orientation of the conjugated plane of the molecules can be quantified by an orientation order parameter, S, which ranges from +1 for a vertical transition (face-on) to -1/2 for a horizontal transition (edge-on) [17]. S decreases from -0.093 in the as-cast sample to -0.15 in the annealed sample (Figure 2.4), suggesting more edge-on character in the annealed blend. It is difficult to separate the contributions from P3HT and DTI to this overall orientation change. NEXAFS analysis on a pristine

DTI film shows that DTI has little orientation preference as-cast ($S = -0.0038$), but is very edge-on after thermal annealing ($S = -0.33$), as shown in Figure A.9. DTI becomes significantly more edge-on after annealing than what is expected for P3HT, and this is supported by X-ray scattering data discussed later. Therefore, it is suspected that the DTI molecules are the main contributor to the observed overall orientation change in the blends. If this is true, then the increase in the amount of DTI character in the π^* peak when going from 30° to 90° should be greater for the annealed blend compared to the as-cast blend. Indeed, this trend is observed (Figure A.11).

A simple conclusion that can be drawn is that the molecules, especially DTI, adopt a more edge-on orientation after thermal annealing. The anisotropic charge transport of DTI suggests that this reorientation is a culprit for the reduced performance in thermally annealed solar cells.

Crystallinity is a critical component in organic solar cells, and the ability to probe the crystalline regions in the film and distinguish between changes occurring in both DTI and P3HT is essential. Grazing incidence wide angle X-ray scattering (GIWAXS) is able to probe order and orientation of the crystalline regions of organic semiconductor thin films [14, 12, 82, 83]. GIWAXS experiments were performed on pristine DTI and P3HT:DTI films to further examine the formation and orientation of ordered DTI structures. Figure 2.5a and 2.5b show 2D GIWAXS patterns of as-cast and thermally annealed DTI films. A broad, diffuse scattering ring at $\sim$1.5 Å^{-1}, typical for amorphous scattering, is clearly visible and suggests low overall crystallinity. There is also a strong reflection at $\sim$0.3 Å^{-1}. Since it is quite broad (FWHM $\approx$ 0.07 Å^{-1}) and the intensity is relatively distributed over all polar angles, it is most likely due to small DTI aggregates or crystals with no preferred orientation.

Scattering reveals noticeable changes in DTI films with thermal annealing, as shown in Figure 2.5b. The broad amorphous ring has mostly disappeared, suggesting greater

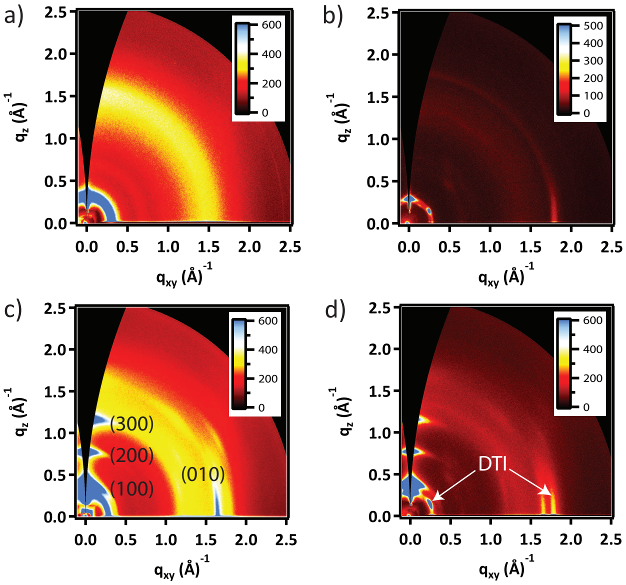

Figure 2.5: Two-dimensional GIWAXS images of pristine DTI a) as-cast and b) annealed, and P3HT:DTI blend films c) as-cast and d) annealed. The characteristic reflections for P3HT are labelled in (c). The missing wedge along q_z represents the inaccessible region of the Ewald sphere in grazing incidence geometry [84].

relative crystallinity. A unique feature of the annealed films is the appearance of a reflection centered at 1.8 Å^{-1}, with greatest intensity in-plane with the substrate, along q_{xy}. This corresponds to a d-spacing of 0.35 nm, typical of a π-π stacking distance in conjugated organics [14]. The fact that the intensity of this reflection is concentrated along q_{xy} reveals that stacks of DTI molecules are predominantly oriented with the π-π stacking direction parallel to the substrate, i.e. most molecules in crystalline regions are edge-on to the substrate. Furthermore, in the annealed film, the main reflection, centered at $q_z = 0.29$ Å^{-1}, has become narrower, indicative of larger crystallites. Interestingly, the intensity distribution for this reflection is not constant. There is a spot of enhanced intensity in the nearly out-of-plane direction and another 60° from the surface normal. Considering the gentle propeller geometry of a DTI molecule, it is expected that they would stack one on top of the other, with adjacent molecules rotating to reduce steric interactions. DTI has been observed to stack into long columns when drop-cast from tetrahydrofuran [31]. The hexagonal pattern seen in GIWAXS suggests that annealing causes separate DTI columns to adopt a hexagonal packing motif and lie parallel to the substrate, a morphology that has been observed for discotic hexagonal columnar liquid crystals [48, 49, 51]. Based on the reflection at 0.29 Å^{-1}, the hexagonal lattice can be described by a parameter, $a_{hex} = 2.47$ nm, which is the distance between adjacent columns.

It is important to see if the packing of DTI is disrupted when blended with P3HT. The scattering from P3HT:DTI blends reveals the characteristic reflections for P3HT, as seen in Figure 2.5c and 2.5d. The as-cast blend film exhibits the typical out-of-plane (100), (200), and (300) reflections of P3HT located close to the q_z axis at $0.38, 0.77$, and 1.17 Å^{-1}, respectively, that correspond to stacking along the hexyl side chain extent. There is also an in-plane peak at 1.65 Å^{-1} corresponding to the π-π stacking distance [85]. The as-cast film shows noticeable amorphous scattering, and an isotropic reflection at 0.29 Å^{-1} originating from the DTI molecules. Similar to the NEXAFS data, GIWAXS results show that upon casting, DTI has little preferred orientation, even when mixed with P3HT. The annealed P3HT:DTI film shows a qualitatively similar scattering from P3HT, but the main DTI reflection at 0.29 Å^{-1} reveals a hexagonal pattern once again, and the in-plane π-π stacking peak for DTI appears as well. This suggests that annealing mostly affects the formation and assembly of DTI crystallites, as the scattering pattern from P3HT remains qualitatively similar. The GIWAXS data is in agreement with the NEXAFS results indicating that thermal annealing leads to an increased degree of edge-on orientation of DTI that hinders electron transport.

Wide angle X-ray scattering can be used to estimate crystallite sizes. Crystallite correlation lengths, which are related to crystallite size, were determined from the width of the diffraction peaks using Scherrer analysis [27, 86]. Correlation lengths along the alkyl chain stacking direction were determined in the nearly out-of-plane (close to q_z)

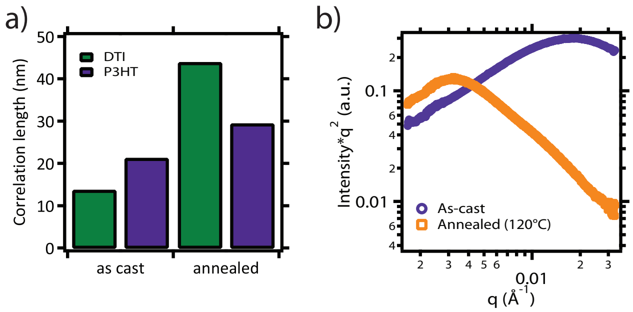

Figure 2.6: a) Crystallite correlation lengths in the nearly out-of-plane direction determined for the hexagonal reflection of DTI and the (100) reflection of P3HT. b) Transmission RSoXS scattering profile taken at 284.4 eV of P3HT:DTI blend film both as-cast (purple circles) and annealed (gold squares) at 120 °C. The data is plotted with a Lorentz correction ($I \times q^2$).

direction for the low-q reflections of P3HT and DTI. For the as-cast P3HT:DTI blend, the out-of-plane correlation length of DTI is relatively small ($\sim$14 nm), suggesting aggregates of only several molecules high. The vertical correlation length for P3HT crystallites is about 21 nm determined from the (100) alkyl stacking reflection. In the annealed P3HT:DTI blend, the correlation length for P3HT remained somewhat similar. However, the correlation length for DTI crystallites increased noticeably to nearly 45 nm (Figure 2.6a). This is significant considering the film thickness is $\sim$100 nm. This suggests that thermal annealing leads to separate parallel columns of DTI that stack quite high. It is likely that the thermally induced reorientation allows multiple nearby columnar aggregates to stack together, hindering vertical electron transport in annealed films. Less dramatic changes were observed for the in-plane (π-π stacking reflection) correlation lengths (Figure A.18).

Periodicities on a larger length scale, often relevant to domain size or phase separation, can be accessed with small angle X-ray scattering. However, the similar electron density between P3HT and DTI make typical hard X-ray small angle scattering experiments difficult. To overcome this, we utilized transmission resonant soft X-ray scattering (RSoXS), which takes advantage of the absorption difference near elemental edges (e.g.

carbon K edge) between materials to enhance scattering contrast [15]. RSoXS data on as-cast and annealed P3HT:DTI blends suggest that the average in-plane separation between DTI-rich domains increases with thermal annealing. As shown in Figure 2.6b, the main peak in the scattering curve shifts from about 0.015 Å^{-1} ($\sim$40 nm) in the as-cast blend to about 0.0033 Å^{-1} ($\sim$190 nm) in the annealed blend. This indicates an increase in the overall domain separation distance and agrees with the large DTI crystallites formed in annealed films.

Morphological characterization reveals significant changes in P3HT:DTI blend films with thermal annealing. Cross-sections of as-cast and annealed films are shown schematically in Figure 2.8. In as-cast films, aggregates of DTI are relatively small and have little preferential orientation, providing potential pathways for electrons to travel to the electrodes. In thermally annealed films, larger stacks of DTI crystallites pack hexagonally with the π-π stacking direction mostly in-plane. This orientation hinders vertical electron transport and reduces solar cell performance. Furthermore, a larger separation distance between DTI domains also limits charge transport.

2.3.4 *In Situ* Experiments Reveal Cold Crystallization of DTI

It is clear that annealing at 120 °C leads to significant changes in the assembly of DTI molecules and the corresponding solar cell performance. However, it was found that annealing at lower temperatures (50 °C) also resulted in greatly diminished performance. This brings to question what temperature is required to cause DTI to form the planar columnar structures that limit charge extraction. Differential scanning calorimetry (DSC) was performed on P3HT:DTI blends and is shown in Figure 2.7a. DSC data on pristine P3HT and DTI is provided in Figure A.20. Upon heating the blend, there is a subtle exothermic peak around 50 °C which appears right before an endothermic transition at

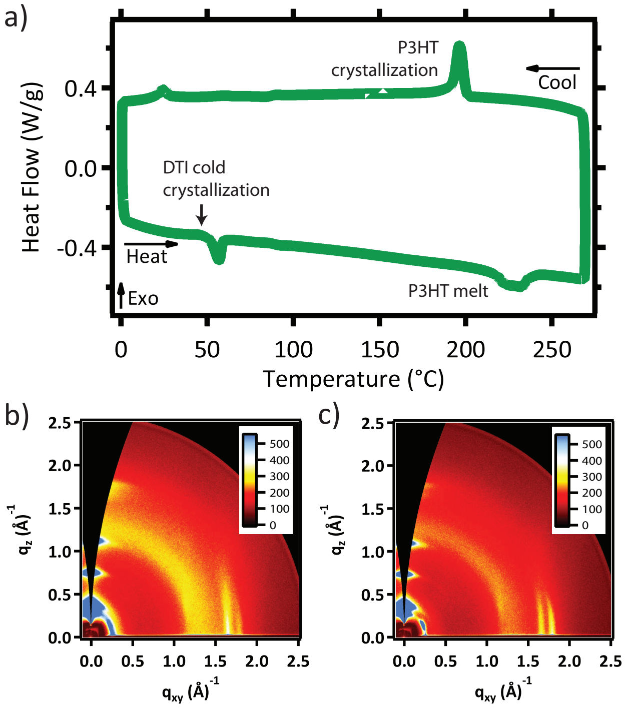

Figure 2.7: a) Differential scanning calorimetry data for a P3HT:DTI blend. *In situ* GIWAXS data collected at b) 60 °C and c) 80 °C during heating.

57 °C. This exothermic peak is probably due to cold crystallization of DTI, or ordering that occurs due to heating. Interestingly, no other melting-type transitions occur even far above 120 °C until the melting temperature of P3HT at about 230°C. On cooling, there is a characteristic crystallization peak for P3HT at 200 °C, and an additional exothermic transition at 25 °C. The main endothermic transition during heating at 57 °C is likely not a melting transition of DTI to an isotropic liquid since GIWAXS scans taken at elevated temperatures well above 57 °C show diffraction patterns of ordered structures, as seen in Figures A.14 and A.15. This peak, and the corresponding exothermic transition at 25 °C, could be due to disordering and reordering of the octyl side chains of DTI.

In order to better understand the structural transitions of DTI, *in situ* GIWAXS experiments were performed at various temperatures during heating. In this way, the sample was heated to a specific temperature and a GIWAXS scan taken. The sample was

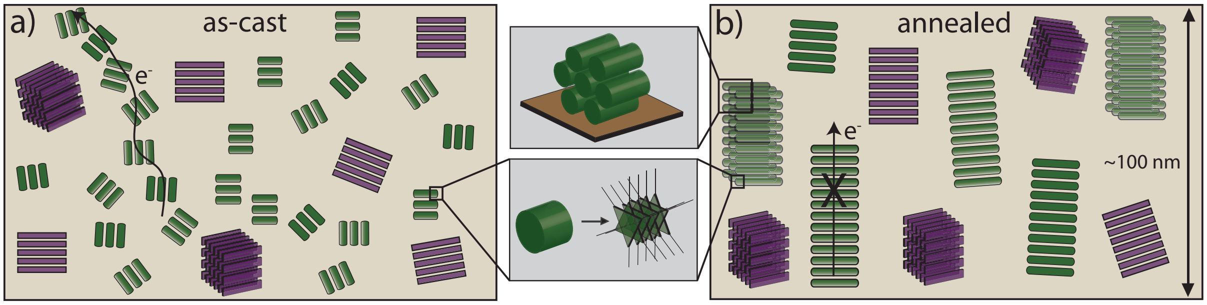

Figure 2.8: Schematic representation of cross sections of (a) an as-cast P3HT:DTI film and (b) a thermally annealed P3HT:DTI film. Stacks of DTI molecules are represented as green pillars, and P3HT crystallites as stacked purple rectangles. The panels in the middle depict close-ups of the hexagonal packing among separate stacks of DTI and how each of the pillars represents a stack of multiple DTI molecules.

then incrementally heated to higher temperatures where additional scattering patterns were obtained at temperature. After starting at room temperature (RT), where the GIWAXS pattern is very similar to that shown in Figure 2.5c, the hexagonal pattern and in-plane π-π stacking start to become visible at 60 °C (Figure 2.7b). This becomes more clear at 80 °C (Figure 2.7c), and even sharper at higher temperatures (Figure A.14). This *in situ* study is in agreement with the GIWAXS data in Figure 2.5, which indicates that annealing leads to hexagonally packed DTI columns with a predominantly in-plane π-π stacking direction. Furthermore, *in situ* scattering reveals that this critical reorientation can occur at a much lower temperature than 120 °C. In fact, for a pristine DTI film, the characteristic pattern of an annealed film is seen even at 40 °C (Figure A.16). P3HT only marginally inhibits the thermally-induced ordering of DTI, and it is likely that the softening of P3HT allows DTI to have reasonable mobility in the blend. These results suggest that the exothermic peak at about 50 °C in the DSC is likely cold crystallization, which is where the DTI molecules have enough thermal energy to order and orient. The *in situ* experiments bring to light the importance of controlling the ordering transitions in these types of discotic columnar materials.

2.3.5 Conclusion

Morphology and molecular orientation are critically important for efficient charge extraction and operation of organic photovoltaics based on non-fullerene acceptors due to their anisotropic charge transport properties. Our study here of a model BHJ with a decacyclene triimide-based acceptor clearly demonstrates how morphological changes upon annealing can be directly related to the PCE. Using a combination of X-ray scattering methods, spectroscopy and device measurements, we find that thermal processing leads to an increase in DTI crystallite size, molecular reorientation, and an increase in overall domain separation distance at relatively low temperatures and short annealing times. The reorientation of DTI molecules to a predominantly edge-on orientation with the π-π stacking direction in-plane with the substrate inhibits electron transport in solar cells.

The results highlight the importance of control over thermal transitions and molecular orientation of novel materials for successful use in BHJ photovoltaic devices. As evident here, the possibility for non-fullerene molecules to change orientation and influence electron transport at relatively low temperatures ($\sim$60 °C) is a potential disadvantage in real-world solar cells that could reach such temperatures under ambient sunlight. Molecular design becomes critical in tailoring the thermodynamics and kinetics of such structural rearrangements associated with these transitions to improve the properties of photovoltaics based on future decacyclene-based or other non-fullerene acceptors.

Chapter 3

Phase Separated Ferroelectric-Semiconductor Polymer Blends for Organic Memory

3.1 Introduction

Polymers offer a unique platform for creating low-cost, solution-processable, and flexible electronics [1, 2, 3, 4, 5]. Semiconducting polymers are essential for these electronics, but ferroelectric polymers have also proven to be useful components in some applications. For example, ferroelectric polymers have been shown to increase the power conversion efficiency of organic photovoltaics [87, 88, 89, 90, 91]. One application in particular that has been of recent interest is organic-based non-volatile memory devices [6, 92, 93], including ferroelectric transistors and diodes [7, 94].

The working mechanism of organic ferroelectric devices relies on the fact that certain polymers, such as those based on poly(vinylidene fluoride), have intrinsic permanent dipole moments that can be oriented by an applied electric field, leading to ferroelectric

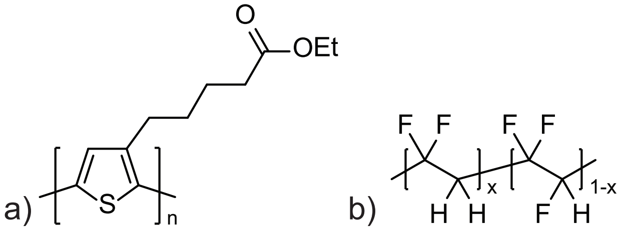

Figure 3.1: Chemical structures of (a) P3EPT and (b) PVDF-TrFE.

behavior [95, 96]. Ferroelectric resistive switches can be fabricated by blending a ferroelectric polymer and a semiconducting polymer, first demonstrated by Asadi et al [97]. Because dissimilar polymers phase separate, thin film blends have distinct ferroelectric and semiconducting regions. Understanding how this phase separation occurs during solidification and subsequent processing is important because the morphology defines the pathways for charge transport and the switching characteristics.

Blends of ferrorelectric polymers and semiconducting polymers provide an interesting opportunity to examine fundamental processes of phase separation in thin films of semicrystalline polymers from solution. Here, we examine the effects of altering the side chain structure of the semiconducting polymer on the phase separation and molecular order in a ferroelectric-semiconductor polymer blend. We find that modification of side chains is a useful route to achieve reliable nanoscale phase separation in thin films while maintaining ferroelectric switching behavior.

The operation of ferroelectric diodes depends critically on the morphology of the phase separated ferroelectric-semiconductor blend film. Charge carriers only travel through the semiconducting polymer and the ferroelectric polymer determines the switching behavior of the device. It is believed based on experimental data and device models that the stray field of the positively (negatively) poled ferroelectric polymer lowers (increases) the barrier to charge injection into the semiconductor phase resulting in greater (decreased) current in the ON (OFF) state [98, 99]. The charge carriers travel predominantly near the semiconductor-ferroelectric domain interfaces [100]. Semiconductor domains that are too large will reduce domain interfacial area and overall current. On the other hand, the stray field lines of the poled ferroelectric act against the direction of charge transport, and this can reduce the current if semiconductor domains are too small. A competition between these two effects results in an optimum lateral size for the semiconductor domains, suggested to be about 50-100 nm [99]. Therefore, an optimal device would have as large a volume fraction as possible of $\sim$50 nm size domains of semiconducting polymer surrounded by ferroelectric polymer domains (the minimum size of the ferroelectric domains has not yet been studied).

It is important to understand the morphology and phase separation of ferroelectric-semiconductor polymer films both at the surface and in the bulk. Charges need to travel through the vertical extent of the film via semiconducting pathways, but differences in morphology between the surface (or buried interface) and bulk could play an important role in charge carrier transport and overall device performance. An idealized structure of these polymer blends is one where the semiconducting polymer forms straight, cylindrical domains through the vertical extent of the film, as shown in Figure 3.2a. However, in reality, the semiconducting domains may deviate from this simplified picture. Previous studies with techniques such as atomic force microscopy (AFM) have revealed that semiconducting polymer domains can form either convex protrusions from the film surface, or concave depressions [100]. Moreover, AFM experiments conducted on blend films where either the semiconducting or ferroelectric component was removed by washing with a selective solvent show that some domains do not go through the entire film thickness, and these partial height domains are undesirable because they do not contribute to overall current [101]. Furthermore, it is difficult to predict the spreading of domains near the film interfaces, and an example of spreading near the film surface is shown schematically in Figure 3.2b. It is expected that a layer rich in the insulating ferroelectric polymer

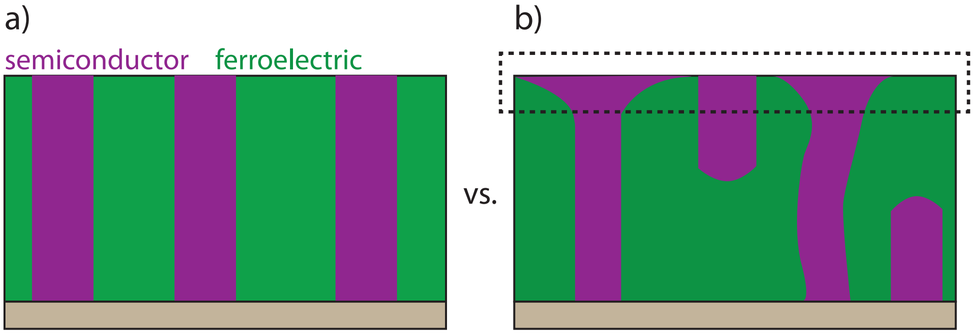

Figure 3.2: Schematic of the cross-section of a semiconductor:ferroelectric polymer blend thin film. An idealized structure with straight, columnar semiconductor domains that extend through the vertical extent of the film is shown in **(a)**. A more realistic structure may consist of features such as semiconductor domains of partial height and/or spreading at the film interface, as shown in **(b)**. This could lead to differences in composition between the surface and bulk, as indicated by the dotted region.

(PVDF-TrFE) at either the film surface or buried interface could be detrimental to device performance since it would block the injection of charges into the semiconducting P3EPT, and/or the collection of charges at the top electrode. On the other hand, an interface layer rich in semiconductor (P3EPT) should be less harmful. However, an excess of semiconducting domains that may result from spreading at an interface could be problematic to efficient charge transport, since parasitic charges may need to traverse laterally through the film before being transported vertically. There is still a need to properly characterize the bulk and surface of ferroelectric-semiconductor polymer thin films, and these differences have not been studied in detail for the P3EPT:PVDF-TrFE system. Soft X-ray based methods can be used to probe both the bulk and surface of P3EPT:PVDF-TrFE thin films.

Soft X-rays can be used to attain materials contrast and chemical sensitivity needed for noninvasive characterization of polymer blend thin films [15, 20, 25, 102]. Most polymers have similar electron densities, making it difficult for hard X-ray small angle scattering and electron microscopy to achieve high scattering contrast [15]. Neutron scattering can provide useful information on polymers, but chemical modification such as deuteration is typically required. Energy-tunable soft X-rays can overcome many of these issues. Soft X-rays span an energy range (about 100 eV to 5 keV) that includes the core-level absorption energies of many of the elements that comprise most polymers, for example, carbon, nitrogen, oxygen, and fluorine [103]. By tuning the incident X-ray to specific energies near the appropriate elemental absorption edge, large absorption differences and high scattering contrast can be attained between different polymers. This enables the use of characterization methods in addition to soft X-ray absorption spectroscopy, including transmission X-ray microscopy [104, 25] and soft X-ray small angle scattering [102]. In combination with hard X-ray wide angle scattering that is sensitive to the crystalline regions of the polymer film, this collection of techniques can probe length scales ranging from Angstroms to microns, allowing for thorough morphology characterization.

3.2 Experimental Methods

Solutions of a concentration of 20 mg/mL were made by dissolving P3EPT (Rieke Metals) or PVDF-TrFE (Piezotech LLC) in 2-methyl-tetrahydrofuran, and mixing at appropriate ratios to form polymer blend solutions. Thin film samples were fabricated by spin coating solutions at 2000 rpm for 60 s onto silicon or glass/ITO substrates. Samples were thermally annealed at 135 °C for 3 hours and slowly cooled to room temperature. Thermal annealing near the melting point of PVDF-TrFE is required to stabilize the ferroelectric β-phase. For transmission experiments, spun cast films were floated off in water and transferred onto Si_3N_4 windows or copper TEM grids.

Soft X-ray absorption spectroscopy experiments were conducted at beamline 11.0.1.2 at the Advanced Light Source, or beamline U7A at the National Synchrotron Light Source. Transmission soft X-ray scattering was performed at beamline 11.0.1.2 and X-ray mircoscopy at beamline 5.3.2.2 at the Advanced Light Source. Two-dimensional hard X-ray grazing incidence wide angle scattering was performed at beamline 11-3 at the Stanford Synchrotron Radiation Lightsource or beamline 7.3.3 at the Advanced Light Source.

Additional experimental details are given in Appendix B.

3.3 Results and Discussion

3.3.1 Modifying Side Chain Chemistry Alters Phase Separation at the Film Surface

A well-defined phase separated structure with easily tunable domain sizes is required for better understanding of fundamental links between morphology and electrical properties. It is difficult to predict polymer-polymer interaction parameters, making it challenging to reduce the domain size of polythiophene based blends well below even a micron when relying on spontaneous phase separation [105], and previous work that utilized regio-irregular poly(3-hexylthiophene) (rir-P3HT) blended with the typical ferroelectric polymer, poly(vinylidene fluoride-*co*-trifluoroethylene) (PVDF-TrFE), showed large-scale phase separation between polymers [105]. Top-down physical patterning methods such as nanoimprint lithography can be used to achieve higher storage densities and smaller switching voltages [106], however such additional processing steps would complicate large-scale production of these devices using printing methods. Semiconducting polymers other than polythiophenes can also be used, and proper choice of solvent and deposition method can produce smoother, thinner films with reduced switching voltages [107]. Incorporation of an insulating, amorphous polymer can also improve the ferroelectric and dielectric performance of ferroelectric polymers [108].

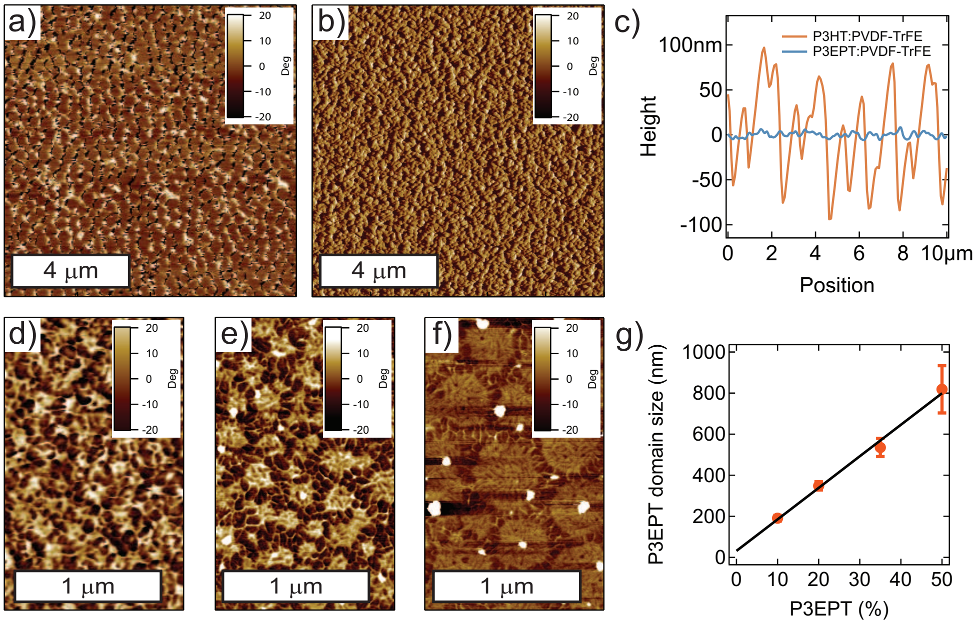

Figure 3.3: AFM phase images of (a) a 10:90 P3HT:PVDF-TrFE blend and (b) a 10:90 P3EPT:PVDF-TrFE blend which shows much smaller phase separation length scales. Additionally, P3EPT based blends result in much smoother films as shown in (c). P3EPT domain size is tunable through variation of P3EPT content, examples of (d) 10 wt%, (e) 20 wt%, and (f) 35 wt% P3EPT are shown. The linear dependence of P3EPT domain size with P3EPT content is shown in (g).

In order to tune the phase separation of ferrelectric-semiconductor polymers blends, we sought to modify the polymer-polymer interactions. It is important to choose a polymer that has a low surface interaction energy with PVDF-TrFE, because a thermal annealing step is required after deposition of the polymer blend film that could lead to coarsening. There is a certain degree of phase separation that occurs during solvent evaporation and solidification of the films during the spin coating process. However, good working devices cannot be made from as-cast films because the paraelectric α-phase of PVDF-TrFE is more stable at room temperature. In order to achieve this, we looked to use a semiconducting polymer that would potentially have more favorable polymer-polymer interactions with PVDF-TrFE. It is known that PVDF has a compatible Flory-Huggins interaction parameter with poly(methyl methacrylate) (PMMA) [109, 110]. In an effort to alter polymer-polymer interactions but maintain semiconducting and charge transport properties, a side chain structure was chosen that is similar to PMMA, while keeping the semiconducting thiophene backbone. The polythiophene used in this study is poly[3-(ethyl-5-pentanoate)thiophene-2,5-diyl], which will be referred to as P3EPT, shown in Figure 3.1. P3EPT is expected to have relatively similar electronic properties to P3HT, and thin film UV-Vis absorption shows a slight blue shift compared to P3HT (Figure B.1).

Blending P3EPT with PVDF-TrFE leads to small domain sizes. Morphology characterization was performed on blends of P3EPT and PVDF-TrFE that were dissolved together in a common solvent (ranging from 10-50 wt% P3EPT) and spin coated into thin films, followed by post-deposition thermal annealing at 135 °C, close to the crystallization temperature of PVDF-TrFE [111], for three hours and subsequent slow cooling to room temperature. This annealing step is required to stabilize and enhance the crystallinity of the ferroelectric β-phase of PVDF-TrFE. P3EPT based blends exhibit much smaller polythiophene domain sizes for a given blend ratio compared to blends of PVDF-TrFE and other semiconducting polymers such as regioregular P3HT (Figure 3.3), rir-P3HT [105] or Poly[(9,9-din-octylfluorenyl-2,7-diyl)-alt-(benzo[2,1,3]thiadiazol-4,8-diyl)] (F8BT) [100]. The phase separation at the film surface can be probed by atomic force microscopy (AFM), and it is clear that P3EPT-based films not only have smaller domains for a given weight fraction of polythiophene, but also a much smoother film surface compared to blends based on P3HT, as shown in Figure 3.3a-c. These are already notable advancements since the ideal semiconductor domain size is thought to be on the order of ∼50-100 nm, and it is often difficult to form smooth films of PVDF-TrFE via spin coating due to the large crystallites that can form, typically requiring more involved strategies such as rapid thermal treatment or blending with PMMA to reduce film roughness [67, 112].

To examine the origin of the observed domain structure, thin films of P3EPT:PVDF-TrFE were spun cast from solutions of varying weight % of P3EPT. AFM images clearly show that increasing the fraction of P3EPT results in an increase in domain size at the film surface, and this is shown in Figure 3.3d-f. The linear dependence of P3EPT domain size with P3EPT weight % (Figure 3.3g) suggests that the phase separated structure may form due to spinodal decomposition as opposed to nucleation and growth, similar to what has been observed in other PVDF-TrFE:semiconducting polymer blends [105, 107]. It is assumed that the regions of higher phase angle correspond to P3EPT domains since they increase in size with P3EPT content. A similar trend is seen in the AFM height topography as shown in Appendix B. AFM height profiles reveal that some P3EPT domains are convex, and protrude out from the film surface, while others are concave depressions. This may have an important impact on electrical properties. It has been shown in an F8BT:PVDF-TrFE system that convex semiconductor domains contribute much less current compared to concave domains, and convex domains are therefore undesirable. This is possibly due to a thin layer of PVDF-TrFE that may form on the bottom, buried interface of convex semiconductor domains, blocking charges from being injected into the semiconductor [100].

P3EPT and PVDF-TrFE are not completely miscible because a distinct phase separated structure forms in the blend, but interactions between the polymers could affect crystallite formation, and can be probed through thermal analysis. Differential scanning calorimetry (DSC) thermograms reveal the main melting and crystallization transitions for P3EPT and PVDF-TrFE (Figure B.5). P3EPT has an endothermic melting transition at around 188 °C, and an exothermic crystallization transition at 149 °C. Both of these transitions have two distinct peaks close together, and this is commonly seen for polythiophene derivatives and may be a result of ordering/disordering of two coexisting semicrystalline microstructures that could form during heating and cooling [113, 114]. PVDF-TrFE has a main melting endotherm at 151 °C and a crystallization exotherm at 131 °C. There is a noticeable shift in the peak position of the crystallization temperatures for both polymers when blended together (Figure B.5). For example, in a 50:50 P3EPT:PVDF-TrFE blend, the crystallization temperature of P3EPT is lowered by about 7 °C to 142 °C, and the transition for PVDF-TrFe is raised by about 2 °C to 133 °C. A similar trend is seen for other blend ratios. This suggests that mixing makes it more difficult for P3EPT to crystallize (more undercooling required), but once it does crystallize the domains may promote the formation of PVDF-TrFE crystallites. This differs from both regioregular P3HT and rir-P3HT. Regioregular P3HT has a higher crystallization temperature, around 200 °C [115], compared to P3EPT, whereas rir-P3HT does not crystallize.

3.3.2 Semicrystalline P3EPT Exhibits Unique Crystallite Orientations

Semiconducting polymers are typically semicrystalline, and this crystallinity can have an impact on charge transport. Therefore, it is important to determine the structural order of P3EPT and to determine if changes in the crystallites occur when it is mixed with PVDF-TrFE, which is also a semicrystalline polymer. Grazing incidence wide angle X-ray scattering (GIWAXS) was used to probe the crystalline nature of thin films of PVDF-TrFE, P3EPT, and their blends. The 2D GIWAXS pattern of PVDF-TrFE reveals a main scattering reflection at $q = 1.41$ Å^{-1}, corresponding to a spacing of ∼4.5 Å, similar to previous reports [105, 116]. The typical hexagonal structure of the PVDF-TrFE crystallites is also evident in the intensity distribution as a function of polar angle of the scattering peak (Figure B.4). GIWAXS of P3EPT has not been reported previously, and the scattering pattern indicates a relatively crystalline polymer. We assume a similar crystallographic assignment as commonly used for other semiconducting polymers where the a axis is along the side chain stacking and the b axis along the π-π stacking direction. The 2D GIWAXS of P3EPT shown in Figure 3.4a depicts three orders of reflections along the side chain stacking direction, which are the (100), (200), and (300) peaks located at 0.34 Å^{-1} (18.8 Å), 0.67 Å^{-1} (9.3 Å), and 1.0 Å^{-1} (6.3 Å), respectively. The d-spacing in the side chain stacking direction is greater than P3HT [115], as expected, but about 1.5 Å smaller than what has been reported for poly(3-octylthiophene) [117, 118, 119]. There is a (010) reflection located at 1.71 Å^{-1}, corresponding to a π-π stacking distance of ∼3.7 Å, about 0.2 Å shorter than typically observed in P3HT, but similar to other thiophene based polymers such as poly[5,5'-bis(3-dodecyl-2-thienyl)-2,2'-bithiophene] (PQT-12) [120]. The intensity distribution of the side chain stacking (h00) peaks suggests a bimodal distribution of crystallite orientations, in this case two main populations of crystallites that are either edge-on or face-on. This is seen based on the enhancement of intensity in both the nearly out-of-plane direction (along q_z) and the in-plane direction (along q_{xy}) for all three side chain stacking reflections. The (010) reflection shows the greatest intensity in the nearly out-of-plane direction, suggesting a relatively greater amount of face-on crystallites compared to other orientations. However, it is expected that the crystallite orientations determined from the π-π stacking reflection should match that of the side chain stacking reflection, i.e. the (010) peak should also show a bimodal distribution of orientations. This discrepancy could be a result of imperfect registry, e.g. slight changes in tilt angle, among molecules composing edge-on crystallites that disrupt π-π stacking but do not affect the side chain stacking distance.

In the P3EPT:PVDF-TrFE blend films, scattering features from both components are present and similar to their respective scattering patterns in the single component films. This trend persists for blends of varying P3EPT composition, as shown in both the 2D GIWAXS images (Figure 3.4c-d) and the line cuts along the nearly out-of-plane and in-plane directions (Figure 3.4e). The two regions of high intensity in the (h00) peaks of P3EPT that indicate bimodal crystallite distribution are also seen in the blend films, especially at higher P3EPT fraction, e.g. a 35:65 P3EPT:PVDF-TrFE blend, as shown in Appendix B.4. This suggests that the two polymers maintain their crystallinity when blended together, and the crystallites in the blend film are composed of either P3EPT or PVDF-TrFE. This is not surprising assuming that the polymers phase separate and form relatively distinct semicrystalline P3EPT and PVDF-TrFE domains, which is needed for functioning resistive switches. However, it is possible that some mixed amorphous regions exist, but this cannot be probed with GIWAXS.

The GIWAXS results show that alteration of polythiophene side chain structure can impact key features of the morphology, such as crystallite orientation and domain size. This opens up new avenues to explore the effect of semiconductor crystallite orientation on

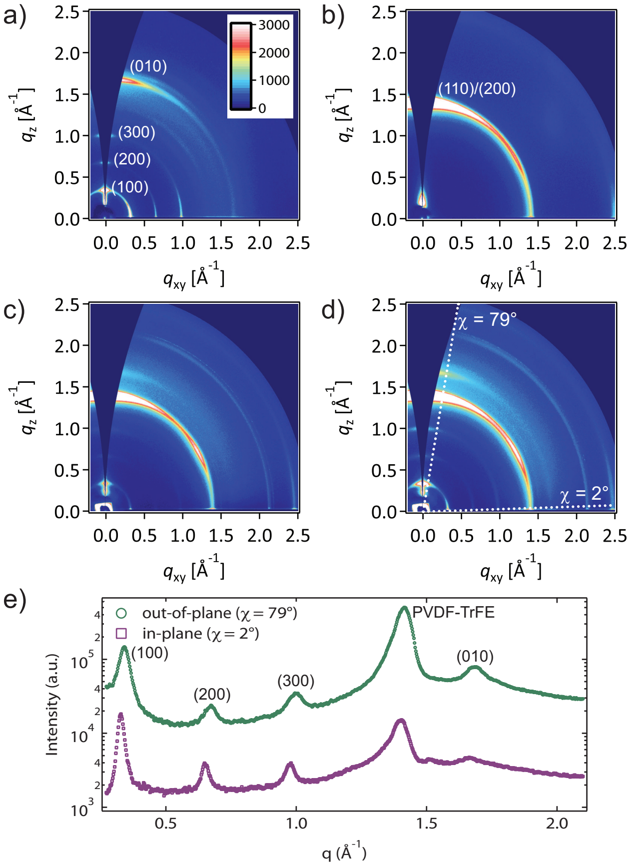

Figure 3.4: Two-dimensional GIWAXS images of (a) pristine P3EPT, (b) pristine PVDF-TrFE, (c) a 10:90 P3EPT:PVDF-TrFE blend and (d) a 20:80 P3EPT:PVDF-TrFE blend. The missing wedge along q_z represents the inaccessible region of the Ewald sphere in grazing incidence geometry[84]. Line-cut profiles at specific polar angles (χ) for the 20:80 blend are shown in (e). The profile at $\chi = 79°$ represents the scattering in the nearly out-of-plane direction, and the profile at $\chi = 2°$ represents scattering in the in-plane direction.

the performance of polymer ferroelectric resistive switches, and P3EPT shows promise as a semiconducting polymer where crystallite orientation can be tuned by changing simple processing or deposition methods.

3.3.3 P3EPT:PVDF-TrFE Blends Create Successful Resistive Switching Devices

In addition to the smaller phase separation length scales and high crystallinity that can be achieved with P3EPT compared to the less crystalline, regio-irregular polythiophene with hydrocarbon side chains (rir-P3HT), P3EPT can be easily incorporated into all-organic ferroelectric switches, as shown in Figure 3.5. A memory device must have distinct ON and OFF states, and Figure 3.5 reveals that P3EPT:PVDF-TrFE results in a much higher current density in the positively poled ON state compared to the negatively poled OFF state. The poling voltage used was ±20 V, corresponding to a field of about 10^8 V/m, similar to previous work [97]. P3EPT:PVDF-TrFE devices also show reasonable ON/OFF ratios (52 for a 10% P3EPT blend measured at 3 V). Successful devices were fabricated out of P3EPT:PVDF-TrFE blends ranging from 10%-50% P3EPT (Figure B.6). This highlights the potential versatility of blends of P3EPT with PVDF-TrFE and one of the benefits resulting from overall smaller dimensions of phase separation, as previous work using rir-P3HT only reported working devices with up to 10% rir-P3HT [97]. The current density (read at 3 V) of a device initially poled to the ON state then held at 0 V, decreased from about 2 A/m^2 shortly after poling to about 0.1 A/m^2 14 hours later, demonstrating reasonable retention times for these initial devices (Figure B.8). Future work will determine the best performing electrode layers for this materials system to optimize the switching and retention characteristics.

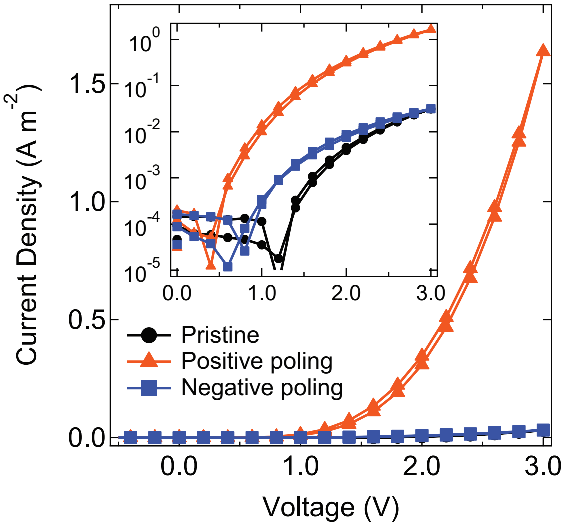

Figure 3.5: Electrical characteristics of ferroelectric resistive switches fabricated from a 10:90 P3EPT:PVDF-TrFE polymer blend. The device structure used was glass/ITO/P3EPT:PVDF-TrFE(∼200 nm)/Ca(10 nm)/Al(90 nm). Devices were poled with a ±20 V pulse. The current-voltage behavior is shown and it is clear that the positively poled ON state has greater current density compared to the negatively poled OFF state. Pristine refers to the device before any poling was applied. A semi-log plot is shown in the inset.

3.3.4 Soft X-ray Absorption Differences Provide Contrast and Chemical Sensitivity

The unique X-ray absorption spectra (XAS) of different polymers provides the basis for attaining contrast and successfully performing soft X-ray scattering and microscopy experiments. Furthermore, XAS itself can reveal useful information, for example, blend composition and molecular orientation [121, 15, 16, 74, 75, 77, 17]. The near edge X-ray absorption fine structure (NEXAFS) spectra around a specific elemental absorption edge reveals information about the bonding environment of each of the atoms of that type. This means that separate polymers, even ones composed of the same atomic elements, can have very different NEXAFS profiles. NEXAFS can be used as a way to “fingerprint” individual polymers [122]. These specific absorption differences allow for contrast in soft X-ray microscopy and scattering of polymer blends.

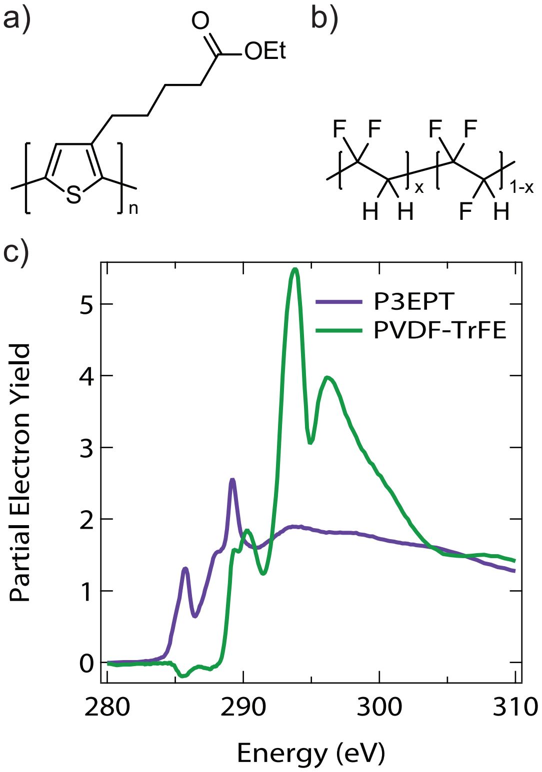

Figure 3.6: Chemical structures of (a) P3EPT and (b) PVDF-TrFE. (c) Partial electron yield carbon K edge NEXAFS of P3EPT and PVDF-TrFE reveals distinct differences in absorption.

The NEXAFS profiles near the carbon K edge of the ferroelectric (PVDF-TrFE) and semiconducting (P3EPT) polymers studied here are noticeably different, as shown in Figure 3.6, and this provides the ability to achieve good contrast in microscopy and scattering experiments. The partial electron yield (PEY) NEXAFS spectra of P3EPT reveals several dominant peaks that can be attributed to core level transitions. The first main transition at about 285.7 eV is typical for materials with C=C bonds and corresponds to a core level C1s → $\pi*_{C=C}$ transition. The peak near 288 eV is likely due to C1s → $\sigma*_{C-S}$ and C1s → $\sigma*_{C-H}$ transitions and is typically seen in similar materials like P3HT. The sharp peak at 289.2 eV arises from a C1s(C=O)→ $\pi*_{C=O}$ transition related to the carbonyl groups in the side chain. The NEXAFS of PVDF-TrFE reveals a very different carbon K edge absorption spectra. There is no peak in the 285 eV region, and this is expected since PVDF-TrFE does not contain C=C bonds. The first features in the profile of PVDF-TrFE (near 289-290 eV) result from the C1s → $\sigma*_{C-H}$ resonance. The next two prominent features occurring at around 293.5 eV and 296 eV, respectively, are due to the C1s → $\sigma*_{C-F}$ resonances. Moreover, PVDF-TrFE contains fluorine atoms so X-ray absorption near the fluorine edge (around 685-730 eV) is selective to PVDF-TrFE (Figure B.9). The differing X-ray absorption profiles between P3EPT and PVDF-TrFE make this an ideal system to utilize complementary soft X-ray microscopy and scattering for morphology characterization.

3.3.5 Transmission X-ray Microscopy and Scattering Reveal Phase Separation in the Bulk

A well-defined phase separated structure of ferroelectric and semiconductor domains is required for operation of organic ferroelectric resistive switches. It has been suggested with techniques such as AFM that noticeable phase separation occurs at the film surface for the P3HT:PVDF-TrFE system. The altered side chain structure of P3EPT tunes polymer-polymer interactions and results in smaller semiconductor domain sizes at the film surface compared to the P3HT-based system, making it potentially a more ideal polymer blend for organic memory applications. AFM and grazing incidence wide angle X-ray scattering (GIWAXS) suggest that P3EPT:PVDF-TrFE films phase separate to form relatively distinct domains [123]. Additionally, *in situ* GIWAXS experiments conducted during thermal annealing of a P3EPT:PVDF-TrFE thin film reveal changes in crystallinity that suggest thermal transitions, for example the melting points, occur at similar temperatures both in the bulk material and the thin film (Figure B.18). Phase separation that persists through the bulk is necessary for charge carriers to travel through the vertical extent of the film via pathways dictated by the semiconducting polymer. Previous work has demonstrated that soft X-ray scanning transmission microscopy (STXM) can successfully probe bulk morphology of P3HT:PVDF-TrFE blends [124]. Although the side chain chemistry of P3EPT alters domain sizes at the film surface, it is important to determine if this morphology is maintained in the bulk, and soft X-ray microscopy and scattering have not yet been done on P3EPT:PVDF-TrFE polymer blends.

STXM images of P3EPT:PVDF-TrFE blends reveal that a phase separated structure exists through the bulk of the film and circular domains are relatively pure in P3EPT. These general features are similar to what has been observed by STXM for P3HT:PVDF-TrFE [124]. Figure 3.7 shows STXM images of a P3EPT:PVDF-TrFE blend with 50 wt.% P3EPT. The 50 wt.% P3EPT blend forms larger domains that are easier to see in STXM images. A similar domain pattern is seen for blends with lower fractions of P3EPT (Figure B.11). By tuning the incident X-ray to energies where absorption is dominated by either P3EPT or PVDF-TrFE, chemical specificity can be achieved. Figure 3.7a shows an image taken at 287.4 eV, where absorption is highly dominated by P3EPT, and it is evident that the circular domains appear dark, corresponding to relatively greater absorption (less transmitted intensity) compared to the surrounding matrix. This verifies that the circular domains are composed primarily of P3EPT. On the contrary, at an energy of 691 eV (Figure 3.7b), which is near the fluorine edge where absorption is dominated by PVDF-TrFE, an inverse image is revealed. That is, the circular regions are now bright, corresponding to low absorption (high transmitted intensity) and the surrounding matrix is relatively darker. This confirms that the matrix polymer is rich in PVDF-TrFE and the circular domains are rich in P3EPT. Furthermore, separate STXM images of the same region of a film at two different energies, one where the materials have different mass absorption and another where they have similar mass absorption, can be used to estimate the composition (wt.%) of the two components [24, 125]. Figure 3.7c and 3.7d reveal that P3EPT domains can be quite pure, about 90-95 wt.% P3EPT in the central region of the polythiophene domains (Figure B.13). This is indicative of good phase separation between the distinct P3EPT and PVDF-TrFE polymers. Previous work based on STXM and transmission NEXAFS of a P3HT:PVDF-TrFE system revealed that P3HT domains were less pure (about 78 wt.% P3HT) [124] than the P3EPT domains considered here. However, because STXM probes the average composition through the thickness of the film, it is difficult to determine vertical changes in composition. Morphological effects mentioned earlier, for example, domain spreading at the surface or partial height domains, could effect the STXM composition values which correspond to an average through the film thickness. Evidence for this can be seen in Figure 3.7c, where some of the P3EPT domains have a reduced P3EPT composition at the edges compared to the central region. Considering the thickness of these films (about 200 nm), interface layers of about 5-10 nm rich in one component would still give vertically-averaged composition values similar to what was estimated. Differences between surface and bulk in P3EPT:PVDF-TrFE thin films are discussed more in the following section.

Transmission resonant soft X-ray scattering (RSoXS) provides information on charac-

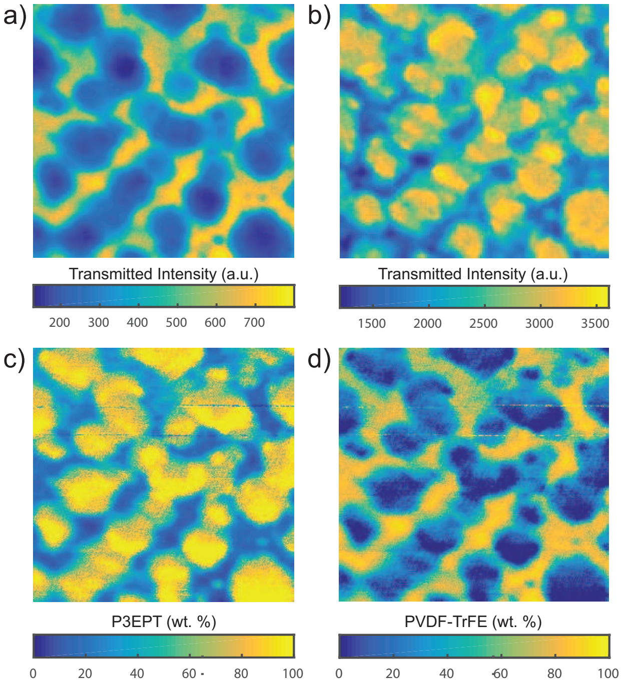

Figure 3.7: Transmission X-ray microscopy images of a P3EPT:PVDF-TrFE blend with 50 wt.% P3EPT taken at (a) 287.4 eV where absorption is dominated by P3EPT, and (b) near the fluorine edge at 691 eV, where absorption is dominated by PVDF-TrFE. Estimated film composition (wt.%) maps are shown in (b) and (c) for the same region of the 50 wt.% P3EPT blend film. The STXM images are 5 X 5 μm.

teristic length scales in the sample and supports the phase separated structure revealed by STXM. RSoXS takes advantage of differences between the complex index of refraction near absorption edges for separate polymers to attain good scattering contrast. This allows soft X-ray scattering to be done in a transmission geometry even for very thin polymer films [20]. Transmission RSoXS profiles of P3EPT:PVDF-TrFE blends with varying fraction of P3EPT are shown in Figure 3.8. It is evident even in the 2D scattering patterns (Figure 3.8a) that there is a ring of intensity that shifts to lower q values with increasing P3EPT content. The peak in scattering intensity is more easily seen in the circularly averaged, Lorentz corrected Iq^2 vs. q plots shown in Figure 3.8b. The clear peak in the scattering profiles is indicative of a characteristic spacing in the samples, which occurs at about 200 nm, 300 nm, and 440 nm for the 10 wt.%, 20 wt.%, and 35 wt.% P3EPT blends, respectively. This length scale likely is related to the average separation distance between P3EPT domains, and it is in reasonable agreement with what is seen in STXM and previously found on the film surface with AFM [123]. The broad, more subtle feature at higher q suggests the presence of order at smaller length scales. These higher q peaks correspond to length scales of about 80 nm, 150 nm, and 360 nm for the 10 wt.%, 20 wt.%, and 35 wt.% P3EPT blends, respectively (Figure B.14). These smaller length scale features do not seem to be higher order peaks since the length scale is not half that of the corresponding lower q peaks. The higher q peaks may correspond to length scales related to the lateral diameter of P3EPT domains. The images in Figure 3.8 were taken at 284.6 eV, an energy where absorption is dominated by P3EPT, as shown in Figure 3.6, and there is good contrast between the two polymers. Transmission RSoXS verifies that a periodicity, corresponding to separated domains, exists through the bulk of P3EPT:PVDF-TrFE films, and this separation increases with increasing P3EPT content. The relatively well-defined and tunable length scales afforded by the P3EPT:PVDF-TrFE system are advantageous for fabricating ferroelectric resis-

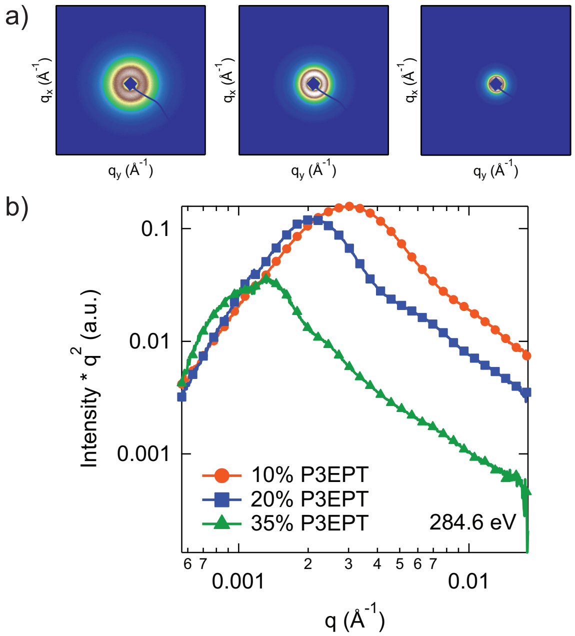

Figure 3.8: Soft X-ray transmission scattering profiles for P3EPT:PVDF-TrFE blends taken at 284.6 eV. (a) 2D scattering images of blends with 10 wt.%, 20 wt.% and 35 wt.% P3EPT, from left to right, respectively. (b) Circularly averaged data reveals a clear peak in the scattering profile that shift to lower q with increasing P3EPT content.

tive switches, and previous work has shown that successful memory devices can be made with a variety of P3EPT fractions [123].

3.3.6 Overall Fraction of Semiconducting Polymer Enhanced at the Film Surface

Differences between surface and bulk composition in these ferroelectric-semiconductor polymer blends may exist, and this could play an important role in charge carrier transport and overall device performance as discussed earlier. These differences are difficult to distinguish with transmission experiments, and surface-sensitive techniques are needed to probe film composition near the interface. Surface segregation of one component in a blend of two semiconducting polymers has been observed previously [126, 127, 128].

Furthermore, earlier work using STXM to characterize P3HT:PVDF-TrFE blends acknowledged the likelihood of a vertically dependent morphology, but this was not studied in detail [124]. A more comprehensive understanding of the surface composition of a thin film blend of a polythiophene and a ferroelectric polymer is still needed. Successful resistive switches can be fabricated with P3EPT:PVDF-TrFE blends for a variety of blend ratios [123], and this suggests it is unlikely that there is a large enhancement, or skin layer, of the insulating PVDF-TrFE at the interfaces to cover the semiconducting domains and block charge injection or collection. Additionally, it has been shown that when P3HT is cast from a solvent selective to the polythiophene (toluene) onto a patterned PVDF-TrFE substrate, the resulting P3HT film wets the PVDF-TrFE substrate [106]. The surface energies of PVDF and polythiophene (P3HT) thin films are reported to be very similar, both around 30 mJ m^{-2} [129, 130], suggesting that intricate polymer-polymer interactions can make it difficult to easily predict surface/interface segregation in these types of semicrystalline polymer blends.

Surface-sensitive PEY NEXAFS spectroscopy reveals a potential enhancement of P3EPT composition at the surface of P3EPT:PVDF-TrFE blend thin films. Figure 3.9a shows bulk-sensitive transmission NEXAFS data of P3EPT:PVDF-TrFE thin films cast from solutions containing 10 wt.%, 35 wt.%, or 50 wt.% P3EPT, or about 14.7 vol.%, 45.5 vol.%, or 60.8 vol.% P3EPT, assuming P3EPT and PVDF-TrFE densities of 1.15 g cm^{-3} and 1.78 g cm^{-3}, respectively. The overall composition of the blends can be estimated by fitting these spectra to a linear combination of transmission NEXAFS spectra of pure P3EPT and PVDF-TrFE films (Figure 3.9a). This method estimates compositions of 10%, 44%, and 64% P3EPT, similar to expected values of 14.7%, 45.5% and 60.8%, which are based on the approximate volume fractions of P3EPT in the solutions used for film casting. However, a similar composition analysis for the surface-sensitive PEY NEXAFS, which probes only the top 1-3 nm of the film [131], reveals surface compositions of about 51%, 79%, and 86% P3EPT. This is significantly higher than the bulk composition determined from transmission data, and suggests a tendency of P3EPT to inhabit the film surface. Although preferential orientation of molecules can affect the intensity of certain transitions, the spectra of the pure components and blends used for composition estimates were taken at the same incident angle, and it was assumed that the general molecular orientation distribution was the same between pure component and blend films. Additionally, preliminary water contact angle measurements on P3EPT, PVDF-TrFE and P3EPT:PVDF-TrFE blend films also imply an enrichment of P3EPT on the surface of the blend films, as shown in Figure B.20. These differences between surface and bulk could result in hindered vertical charge carrier transport and are important to consider for device performance. Taking into account the surface-sensitive and bulk characterization, it is evident that for the P3EPT:PVDF-TrFE system studied here, the morphology through the film is better represented by the schematic shown in Figure 3.2b, as opposed to the simplified view of straight, columnar semiconducting domains depicted in Figure 3.2a.

NEXAFS is useful to estimate film composition, but it cannot distinguish between amorphous and crystalline polymeric regions. Differences in the molecular order at the surface and in bulk are important due to the influence on charge transport. Grazing incidence wide angle X-ray scattering (GIWAXS) is a versatile technique used to probe crystalline regions in polymer thin films [14, 12], and the degree of surface or bulk sensitivity can be tuned by varying the incident angle [132, 133, 134]. For polymer thin films at the energy used for these experiments (12.7 keV), the critical angle for total external reflection (α_c) is close to 0.11° [134]. The penetration depth of X-rays remains small at angles below α_c, increases rapidly near α_c, and slowly grows with incidence angles well above α_c. An estimation of penetration depth as a function of incidence angle for a P3EPT:PVDF blend is shown in the Figure B.15. It is clear that at an incident angle

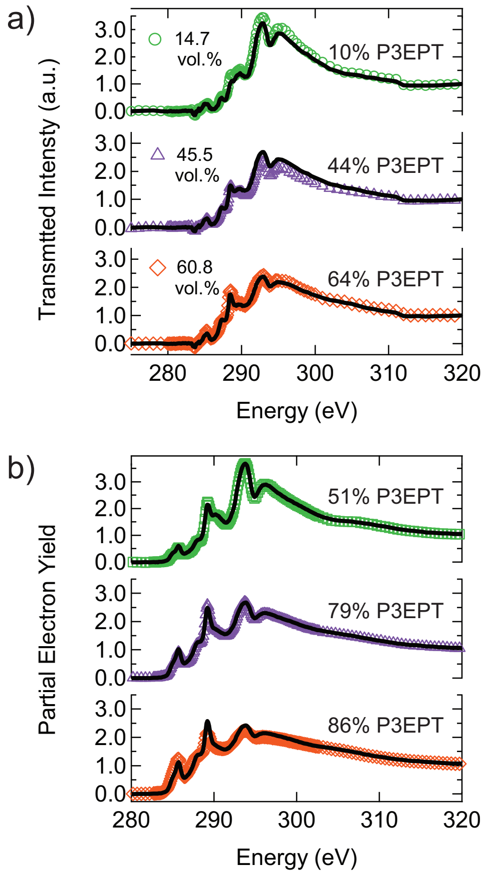

Figure 3.9: Carbon K edge NEXAFS spectra of P3EPT:PVDF-TrFE blends with varying P3EPT content. The graphs in (a) and (b) show experimental data for films cast from solutions with P3EPT contents of 10 wt.% (14.7 vol.%), 35 wt.% (45.5 vol.%), and 50 wt.% (60.8 vol.%), from top trace to bottom trace, respectively. The black fit curves to estimate composition were determined by a linear combination of the pure component spectra. Bulk sensitive transmission NEXAFS is shown in (a), and highly surface sensitive partial electron yield data is shown in (b).

of 0.08° the penetration depth is still very shallow (about 60 Å) and scattering results from near the film surface. An incident angle of 0.12° (greater than α_c) is considered bulk sensitive since it is in a region where the penetration depth is much greater and past the critical region where penetration depth varies extremely rapidly with incident angle. The inflection point in penetration depth and the maximum in transmittivity occur at α_c. However, the maximum scattered intensity of a structural feature depends on the electric field within the film and the film thickness, and it does not necessarily occur at α_c [133]. Figure 3.10 shows azimuthally integrated GIWAXS data of a 20 wt.% P3EPT blend film taken at 0.08° and 0.12°. The data was fit to a combination of peaks corresponding to the individual reflections of P3EPT and PVDF-TrFE, and a broad feature located at about 1.7 Å^{-1}, which is attributed to scattering from disordered regions of the film and side chains. As expected, the overall intensity of the 0.08° trace is noticeably lower since only the surface of the film is probed. The relative fraction of PVDF-TrFE crystallites to P3EPT crystallites can be estimated from the ratio of the area of the PVDF-TrFE reflection, located at 1.4 Å^{-1}, to the area of the P3EPT (100) reflection, located around 0.33 Å^{-1} (both shown in Figure 3.10). This ratio is about 5 for the 0.08° and 0.12° incident angles. Although NEXAFS reveals that there is an overall greater fraction of P3EPT at the film surface compared to the bulk, the relative amount of P3EPT crystallites to PVDF-TrFE crystallites does not change significantly between surface and bulk. This suggests that the excess P3EPT at the film surface may be more disordered. Furthermore, the GIWAXS reveals that the contribution to scattering from the broad, amorphous peak is significantly higher at the surface sensitive 0.08° angle compared to the more bulk sensitive 0.12°. This result refers to relative differences in the amount of scattering from crystallites of P3EPT compared to PVDF-TrFE in the blend film, and does not correspond to the overall crystallinity of each respective homopolymer.

Charge transport and the resulting device performance may be affected by both the

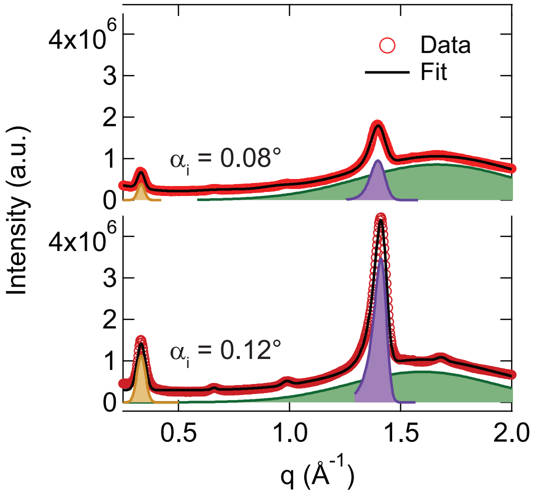

Figure 3.10: GIWAXS of a P3EPT:PVDF-TrFE blend film with 20 wt.% P3EPT at different incident angles. The top trace is at a surface sensitive incident angle of 0.08°, and the bottom trace at 0.12° where the penetration depth is much greater. The individual peaks of the P3EPT (100) reflection, PVDF-TrFE reflection, and amorphous scattering that contribute to the overall fit curve are shown.

differences in composition between the surface and bulk, which were discussed earlier and suggested by NEXAFS experiments, and differences in the molecular order of the semiconductor. It is known that crystallization reduces the ionization energy of P3HT by a few tenths of an eV relative to amorphous domains [135, 136]. Therefore, a decrease in the amount of crystallinity near the film surface could result in an effective energy barrier for extraction of holes near the interface for P3EPT. This surface layer is relatively thin (∼10 nm) and did not impede the operation of P3EPT:PVDF-TrFE diodes [123]. Further study of the details of the operation of transport within these devices will reveal the role of this interfacial region.

Differences between surface and bulk morphology can be expected to affect other materials systems with different semiconducting polymers, especially those containing similar polymers such as other functionalized polythiophenes. However, further work is required to better understand the universality of this trend as polymers with significantly different chemistries cannot be assumed to adopt a similar nanostructure as the

P3EPT:PVDF-TrFE system. Furthermore, the relatively well-defined phases formed in P3EPT:PVDF-TrFE blends provides opportunities to understand the competition between natural phase separation and directed assembly through, for example, patterned substrates to further optimize morphology for organic memory diodes.

3.4 Conclusion

Our work has shown that side chain modification of a semiconducting polymer can drastically change the phase separation of semiconductor-ferroelectric polymer blends. Specifically, compared to a polythiophene with a hydrocarbon side chain such as P3HT, a polythiophene with a side chain structure containing an ester functional group, P3EPT, results in smaller domain sizes and excellent domain size tunability when blended with the common ferroelectric polymer PVDF-TrFE. This is a significant improvement in realizing an ideal morphology for all-polymer ferroelectric resistive switches. P3EPT shows signatures of strong crystallinity, and its crystallites adopt a relatively bimodal distribution of edge-on and face-on orientations when spun cast. Furthermore, P3EPT:PVDF-TrFE blends produce working ferroelectric resistive switches over a range of P3EPT weight fractions with good ON/OFF ratios. This material provides a potential model system to understand fundamental effects of semiconductor domain size, crystallinity, and crystallite orientation on electrical properties for organic resistive switches. These studies provide insights into the subtleties of the effects of polymer side chain structure on polymer-polymer interactions, applicable to both the physics of ferroelectric-semiconductor polymer blends in general and the improvement of organic memory devices.

P3EPT:PVDF-TrFE polymer blends form a phase separated structure in the thin film that persists through the bulk. Soft X-ray spectroscopy reveals that P3EPT and PVDF-TrFE have distinct absorption profiles near the carbon K edge. Transmission soft

X-ray microscopy shows that P3EPT:PVDF-TrFE blend thin films consist of relatively well-defined regions of P3EPT surrounded by a matrix rich in PVDF-TrFE. Additionally, transmission soft X-ray scattering demonstrates a clear domain separation distance that increases with increasing P3EPT content. Furthermore, surface sensitive NEXAFS and grazing incidence X-ray scattering suggest a potential enhancement of P3EPT content at the film surface relative to the bulk, and that this surface region may be more amorphous in character. These results reveal the importance of both bulk and surface characterization of ferroelectric-semiconductor polymer blend thin films, especially with a semicrystalline polythiophene with a functionalized side chain structure. This opens the door for understanding how the three-dimensional microstructure of ferroelectric-semiconductor polymer blends influences the performance of ferroelectric resistive switches, and the important morphological features to control when designing organic memory devices.

Chapter 4

First-Principles Predictions of X-ray Absorption Spectroscopy for Characterization of Semiconducting Polymers

4.1 Introduction

Semiconducting polymers are promising materials for a variety of low-cost, solution-processable, and flexible organic electronic applications [3, 5, 2, 12, 1, 4]. The unique electronic structure of these conjugated materials allows for charge carriers to travel within a single polymer chain and also between adjacent chains. An understanding of the electronic structure, especially the unoccupied molecular orbtials, is needed to better understand and tailor the chemical structure for improved properties. Furthermore, most semiconducting polymers have a relatively rigid backbone and solubilizing side chains which results in anisotropic charge transport [13]. Charge carriers can typically travel more easily along the backbone direction and between separate polymers via cofacial π-π stacking, but transport is hindered through the insulating side chains. The intrinsic electronic properties and the packing and orientation of assemblies of semiconducting polymers in solid thin films is critical to charge transport on length scales ranging from the molecular level to device dimensions. Therefore, the ability to characterize both the electronic structure specific to a given material and the morphology of semiconducting polymer thin films is required.

Near edge X-ray absorption fine structure (NEXAFS) spectroscopy provides rich information on the electronic structure of materials, and it can be used to probe detailed morphological parameters, for example, molecular orientation in thin films of semiconducting polymers [137, 21, 138, 139, 140]. NEXAFS utilizes X-rays with energies close to the absorption edge of a specific element, and it probes transitions of core level electrons to unoccupied molecular orbitals. This makes NEXAFS unique in that it is sensitive to electronic structure not only due to the types of atoms present in a material, but also the bonding environment and specific chemical structure of a compound. The electronic structure information probed by NEXAFS is important for conjugated polymers, as the excited state electronic structure may reveal reasons for variations in device performance among these materials. Understanding of NEXAFS spectra could help elucidate connections between excited state delocalization and the formation of free charges versus excitons, which is still not well understood [141, 142, 143]. Additionally, polarized X-rays allow for determination of molecular orientation in thin films, and NEXAFS is critical in gaining contrast and interpreting data from techniques such as scanning transmission X-ray microscopy and resonant X-ray scattering [15]. NEXAFS has the ability to probe either through the bulk of organic thin films or be selective to the film surface depending on the type of detection mode used, for example, transmission or electron yield. This allows NEXAFS the ability to elucidate differences in certain parameters, e.g. molecular orientation or blend film composition, between the surface and bulk.

A general interpretation of the peaks observed in experimental NEXAFS spectra is often based on the so-called building block model, where complex molecular compounds are regarded as being composed of diatomic subunits [144, 145] that are summed together to understand the overall NEXAFS spectra. However, the building block model can be difficult to apply in larger, more complex molecules [146]. In these more intricate molecules, the specific bonding environment can result in noticeable X-ray absorption shifts, making the overall spectra challenging to decompose with the building block model. An additional factor to consider in semiconducting polymers is that despite the localization of a core hole, unoccupied molecular orbitals are often very delocalized. Some more complicated theoretical models have been developed and applied to polymers that show qualitative agreement with experiment [147, 148, 149]. Nevertheless, a deeper understanding of the exact transitions present requires proper calculations to complement experiment. Here, we show that first-principles predictions based on constrained-occupancy density functional theory (DFT) can be used to simulate core-level X-ray absorption spectra of semiconducting polymers. This is advantageous for understanding various aspects of experimental data, including the nature of specific transitions and details of angle-dependent measurements for orientation analysis.

Experimental NEXAFS has been applied extensively to polymers in general, and it has proven useful in determining surface composition and surface segregation in thin films [150, 151], domain composition in phase separated blends [24, 124], and the overall orientation, or tilt angle, of the backbone of semiconducting polymers [137, 21, 138, 139, 140]. For many of these typical analyses, experimental data is sufficient. However, more intricate analysis can be difficult based on experimental data alone. For example, certain semiconducting polymers have a twist angle between separate moieties in the backbone, and estimating the specific tilt angle of each subunit relative to the substrate is very challenging [139]. The absorption properties of polymers at energies near certain elemental edges, e.g. carbon, nitrogen, and oxygen, can be combined with microscopy or scattering to obtain spatial and morphological information. Scanning transmission X-ray microscopy (STXM) utilizes the absorption differences between distinct polymers to achieve high contrast real-space images that are useful for visualizing domain distribution [21, 25]. Polarized soft X-ray scattering (PSoXS) also takes advantage of the unique absorption spectra of polymers to gain good contrast between materials that have similar electron densities and would otherwise have low scattering contrast for hard X-rays [15, 20]. Moreover, PSoXS is sensitive to the direction of specific transition dipole moments and numerous factors, for example, domain separation distances in blend films and fluctuations in molecular orientation [22], can all contribute to the complex scattering patterns.

Efforts to calculate the NEXAFS spectra of polymers have shown to be helpful in understanding effects such as the number of subunits, core hole location, and molecular orientation [152, 153, 149, 147, 148], relevant when considering macromolecules. However, there are only very few reports of using simulations to estimate core-level spectroscopy of semiconducting polymers [143, 154, 138], and typically only fragments of a full polymeric chain are used in these calculations. An enhanced fundamental understanding of the proper models required to reliably predict NEXAFS transitions of conjugated polymers would greatly improve the ability to conduct and interpret experimental results. This is especially important with the recent growth in the use of techniques such as PSoXS to characterize semiconducting polymer films where a detailed understanding of X-ray absorption is required for proper analysis.

In this study, we demonstrate first-principles predictions of core-level X-ray absorption spectra of semiconducting polymers using the eXcited electron and Core Hole (XCH) approach [155] based on constrained-occupancy DFT methods. XCH has already been shown to work well for systems containing small organic molecules or periodic systems such as graphene [156, 157, 158, 159, 160]. We are specifically interested in simulation tools that are accessible and tractable to experimentalists and can be beneficial for improved data analysis. Thiophene is used as a model system considering its relatively simple structure and the breadth of work focused on poly(alkylthiophene)s experimentally. Many recent studies have focused on using the donor-acceptor class of semiconducting polymers, and poly[4-(4,4-dihexadecyl-4H-cyclopenta[1,2-b:5,4-b‘]dithiophen-2-yl)-alt-[1,2,5]thiadiazolo[3,4-c]pyridine] (PCDTPT) is used here as one model system for a donor-acceptor polymer. We show how predicted NEXAFS evolve as a function of the number of polymer repeat units and the length of attached side chains. These simulations are also used to demonstrate how to identify the nature of specific transitions in complicated spectra and the important effects of preferred orientation on relative peak intensities. Overall, we hope to reveal important aspects that should not be overlooked when dealing with NEXAFS spectra of conjugated polymers.

4.2 Experimental and Computational Methods

4.2.1 Computational Methods

Polymer fragments were modelled as an oligomer containing a specific number of repeat units. Typically, methyl groups replaced full hydrocarbon side chains to reduce computational time. The geometry of these fragments were optimized using density functional theory (DFT) with the B3LYP level of theory and a 6-31G(d) basis set using the Gaussian 09 package.

To create repeating segments that were used for periodic boundary conditions along the polymer chain axis direction, geometry was optimized for fragments consisting of the desired repeat structure with additional repeat units added to each end. The distance between the ends of the desired repeat unit were measured, and the additional end units removed. This distance was then used as the length of the unit cell when running XCH calculations. An example for a thiophene based polymer is shown in Figure C.1. Fragments used as unit cells for periodic boundary conditions were about 20 Å or greater in the direction along the chain axis. For example, a sexithiophene-based unit was used as the repeating unit cell for poly(thiophene) (Figure C.1), even though an identical repeating structure can be obtained based on a bithiophene unit cell. This was done because in the calculations, the specified atoms (typically in the center of the unit cell) are excited in every unit cell, and a critical unit size is needed to avoid simultaneously exciting atoms very close to each other. For simulations on isolated polymer fragments, the desired fragment, or oligomer, size was used, and the dimensions of the unit cell box persisted significantly beyond the extent (by about 5-10 Å) of the molecular dimensions to avoid interactions between neighboring molecules.

The resulting atom coordinates of the geometry-optimized molecular models were used as inputs for the XCH calculations that predict NEXAFS spectra. For this study, the atom coordinates remained fix during computations. Simulated NEXAFS spectra were calculated based on approximations to Fermi's golden rule. This study employed the eXcited electron and Core-Hole (XCH) approach [155, 158] based on constrained-occupancy DFT. In the XCH method, the lowest-energy excited state core-hole is accounted for by replacing the pseudopotential of the core-exicted atom with a core level potential that explicitly includes a core excitation. The screening presence from the excited electron is also included. Higher-energy states are estimated relative to the lowest core-excited reference state based on the unoccupied portion of the Kohn-Sham DFT eigenspectrum. Energy alignment was determined based on a previous method that references excited states to theoretical isolated atoms [161, 162]. In this case, simulated carbon K edge spectra were shifted by a value of 284.5, and nitrogen K edge spectra by a value of 396.5 to align calculated spectra with the units (eV) of experimental data. DFT within the Perdew-Burke-Ernzerhof (PBE) [163] generalized-gradient approximation is known to underestimate band gaps [164, 165], resulting in XAS calculations that are compressed with respect to the energy axis. Therefore, a dilation factor of 1.1 was applied to all carbon K edge simulations, and a dilation factor of 1.2 to the nitrogen K edge simulations. Simulated transitions are represented as Gaussian peaks with peak widths of 0.2 eV and heights proportional to the calculated oscillator strength of a given transition.

4.2.2 NEXAFS Spectroscopy Experiments

Samples for NEXAFS experiments were fabricated by basic spin coating of polymer solutions onto silicon substrates. Aligned PCDTPT samples were fabricated by blade-coating onto a nanogrooved substrate, as previously reported [166].

Samples for electron yield NEXAFS were prepared by spin-coating onto Si substrates. Partial electron yield NEXAFS experiments were performed at beamline U7A at the National Synchrotron Light Source (NSLS). The incident X-ray beam was elliptically polarized (polarization factor = 0.85) with the electric field vector predominantly in the plane of the storage ring. The incident angle, θ, was varied. 90° refers to an incident X-ray beam that is perpendicular to the substrate. A spherical grating monochromator was used to select soft X-rays in the energy range from 280 eV to 420 eV, corresponding to the carbon and nitrogen K edges. The partial electron yield (PEY) data was collected with a channeltron electron multiplier with an adjustable entrance grid bias that was set to -150 V. All experiments were done in a UHV chamber. Energy calibration is typically done by comparing to a polystyrene standard, where the $\pi^*_{C=C}$ for polystyrene is set to 285.5

eV. Carbon edge PEY data was normalized by subtracting a linear pre-edge baseline and setting the edge jump to unity at 320 eV. Additional electron yield NEXAFS experiments were performed at beamline 11.0.1.2 at the Advanced Light Source [23]. Total electron yield was determined based on the neutralization current.

4.3 Results and Discussion

4.3.1 Polymers Can be Approximated by Appropriately Sized Fragments for NEXAFS Simulations

Polymers are long chain molecules, and the wavefunctions in conjugated oligomers and polymers are delocalized over many repeat units [167]. It is therefore of underlying importance to know what size polymeric fragment is best suited for proper NEXAFS calculations. Due to the localized nature of the core hole formed in NEXAFS excitations, it is reasonable to expect that NEXAFS spectra can be adequately simulated from a molecular model of just a single or several polymer repeat units. However, the delocalized unoccupied states in semiconducting polymers could affect these transitions, which is important to consider when deciding the size of molecular models for predicting NEXAFS spectra. It is known that the excitation energies of π^* or non-bonding electrons to antibonding orbitals in conjugated systems depends on the chain length, and the band gap decreases with increasing conjugation length [168, 167]. The photoluminescence of single conjugated polymer chains depends strongly on chain conformation [169], and it is suggested that non-radiative decay processes following excitation of an electron in the valence band become more efficient with increasing conjugation length [170]. The unique features of semiconducting polymers related to conjugation length and orbital delocalization make it necessary to understand the effect of oligomer size (or full polymer) on predicted core level transitions. To provide insight into the effects of molecular size, XCH calculations were performed on small fragments (one or two repeat units), intermediate oligomers, and infinitely long chains.

We examined the evolution of XCH-predicted spectra as a function of chain length for a common conjugated polymer based on poly(thiophene) and found that intermediate sized fragments are suitable for simulating experimental NEXAFS spectra. The predicted carbon K edge spectra for a thiophene based system is shown in Figure 4.1. XCH calculations were performed using planar thiophene-based models containing methyl side chains (Figure 4.1b). Unless otherwise indicated, the first-principles results assume no specific orientation, and equal contributions are taken for an electric field vector pointed along the x, y, or z directions (see coordinate system in Figure 4.5a). Each calculated core level transition is represented as a Gaussian lineshape at that energy with a full width at half maximum of 0.2 eV and a peak height proportional to the predicted oscillator strength. The sum of all of the Gaussian peaks is what is depicted as the overall simluated spectra. It is evident that the predicted NEXAFS spectra for bi(3-methylthiophene) differs noticeably from that of sexi(3-methylthiophene) and poly(3-methylthiophene), both in terms of peak positions and relative intensities. This difference is likely related in part to the presence of carbon atoms on the edge positions, which are a significant contribution in the bithiophene model. These edge atoms have a different bonding environment than carbon atoms bonded directly to other thiophene units, and corresponding changes in the spectra are expected. Furthermore, certain unoccupied molecular orbitals (MOs), for example π^* MOs shown in Figure 4.1b, are quite delocalized and the limited size of the bithiophene unit limits the ability of these MOs to delocalize to the extent possible on a polymer chain, and this could change the energy of the MO. The altered simulated spectra of the bithiophene-based model relative to the spectra from larger fragments demonstrates that in certain cases, molecular models that are too small may not adequately approximate a polymer.

The predicted spectra of sexi(3-methylthiophene) and poly(3-methylthiophene) are very similar, suggesting that the intermediate sized sexithiophene-based model is adequate to approximate a very long polymer chain for this system. For calculations of sexi(3-methylthiophene) and poly(3-methylthiophene), only carbon atoms on the two central thiophene units were excited, avoiding contributions from edge atoms and interactions with excited atoms in adjacent unit cells. As seen in the MOs shown in Figure 4.1b, the larger size of these units allows the π^* orbitals more space to delocalize. The C 1s → π^* transitions, which are the peaks between 284 and 286 eV, show highest intensity around 285.8 eV, with reduced intensity features at lower energy. These characteristics in the π^* region are also evident in the experimental spectra of poly(3-hexylthiophene) (P3HT), as seen in Figure 4.6, indicative that both of these models approximate real polymers quite well. These separate π^* peaks arise from excitations of distinct carbon atoms on the thiophene unit. It is especially important to be able to simulate the π^* transitions in semiconducting polymers since π^* peaks are typically used for orientation analysis, which is a critical parameter related to charge transport.

Many recent semiconducting polymers are in the class of low-bandgap donor-acceptor polymers [171], which typically have more intricate structures than polythiophenes. It is important to be able to predict X-ray absorption spectra of this class of polymers not only at the carbon K edge, but also other relevant absorption edges such as the nitrogen K edge, as they often contain additional elements such as nitrogen, oxygen, and sulfur. Experimental and simulated nitrogen K edge NEXAFS of PCDTPT is shown in Figure 4.2 (carbon K edge spectra shown in Figure C.2). Initial XCH-based calculations of PCDTPT were first shown in a recent contribution [166]. Evolution of calculated spectra is shown from a single donor(CDT)-acceptor(PT) unit, to an intermediate sized CDT-PT-CDT-PT fragment, and a fully periodic PCDTPT based on a unit cell containing

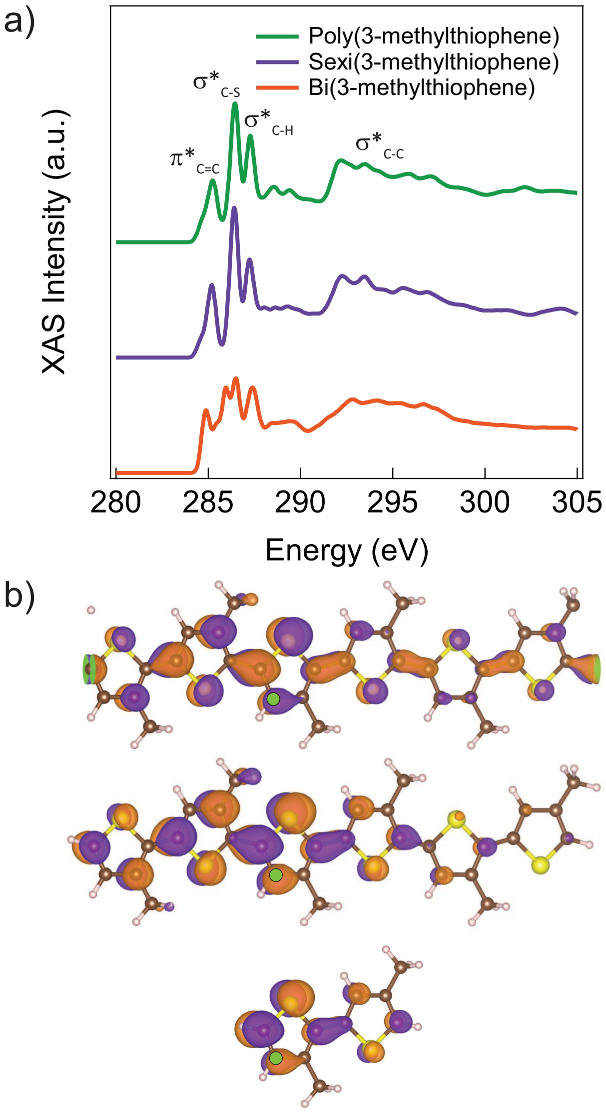

Figure 4.1: Evolution of XCH-predicted carbon K edge NEXAFS as a function of number of repeat units for a 3-methylthiophene based system. Simulated spectra of small bi(3-methylthiophene), intermediate sized sexi(3-methylthiophene), and infinitely long poly(3-methylthiophene) models are shown in (a). Structures of the different molecular models are shown in (b). Bi(3-methylthiophene) (bottom), sexi(3-methylthiophene) (middle) and a poly(3-methylthiophene) based on a sexi(3-methylthiophene) unit cell (top). Electron density distributions of the lowest unoccupied molecular orbitals overlay the molecular models. The excited atom is shown in green.

four CDT and four PT units (Figure 4.2b). The simulated nitrogen K edge NEXAFS for all three model sizes are very similar, especially the CDT-PT-CDT-PT model and the PCDTPT model. Differences in the relative peak intensities are noticeable in the smaller CDT-PT system. The relative peak positions of the experimental data compared to each of the calculated spectra agree quite well. The experimental NEXAFS shows that the first two most obvious peaks are at around 400 eV and 403 eV. However, there is noticeable absorption intensity between these two peaks, suggesting the presence of additional transitions between them. The simulations reveal that there are two additional peaks, at about 401.5 eV and 402 eV, between the main features at 400 eV and 403 eV. These distinct transitions are present in the simulations for all three different models of different lengths, however the relative intensities of these peaks vary slightly among the different models. The discrepancy in relative peak intensities between the experiment and the simulated spectra is likely due to preferred orientation of the PCDTPT sample. This is not taken into account for the simulated spectra shown in Figure 4.2, and will be discussed later.

Donor-acceptor polymers may have more localized MOs that tend to reside either mostly on the donor unit or the acceptor unit [143]. This may partly explain why smaller molecular fragments, in terms of number of repeat units, are sufficient for reasonable calculations compared to a polymer like a poly(3-alkylthiophene). As we previously reported, PCDTPT is interesting in that the degree of delocalization of the lowest unoccupied molecular orbital (LUMO) depends on which nitrogen atom is excited [166]. For PCDTPT, all of the nitrogen atoms reside on the PT acceptor subunit. Furthermore, the side chains are only attached to the CDT donor unit, and there are no nitrogen atoms on the side chains. These factors help simplify considerations with regards to nitrogen K edge spectra of PCDTPT, making this polymer a good model system for demonstrating the ability of the XCH method to handle nitrogen K edge simulations of donor-acceptor polymers. The XCH method shows the potential to properly simulate the NEXAFS spectra of a variety of donor-acceptor polymers. Additional examples of PDPP2FT and P(NDIOD-T2) are shown in Appendix C.

Considering the localized nature of a core hole, but the often highly delocalized MOs in semiconducting polymers, NEXAFS spectra can be modelled by appropriately sized molecular fragments using the XCH approach. Moreover, the pseudopotential-based DFT and planewave basis sets employed in XCH render this method suitable for efficiently modelling X-ray absorption spectroscopy of full polymer chains. This is advantageous since using periodic boundary conditions itself does not incur much additional computational expense. If the appropriate unit cell for periodic boundary conditions has a similar number of atoms as an oligomer, for example sexithiophene vs. poly(thiophene), then similar computational efficiency can be achieved. If the repeating unit cell requires many more atoms, such as for PCDTPT as shown in Figure 4.2b, then periodic boundary condition simulations will be significantly more expensive.

4.3.2 Side Chain Atoms Bonded Directly to the Conjugated Backbone Affect π^* Transitions

Semiconducting polymers typically contain hydrocarbon side chains that impart solubility in common organic solvents and can affect intermolecular packing. These side chains do not strongly affect intramolecular charge transport along the conjugated core, and are often removed when performing calculations to improve computational efficiency. However, it is important to understand the effect side chain atoms have on NEXAFS spectra, especially with regards to the important C 1s→ π^* transitions that are associated with the conjugated backbone and often used to probe molecular orientation.

The presence of a substituent side chain alters the bonding environment of the back-

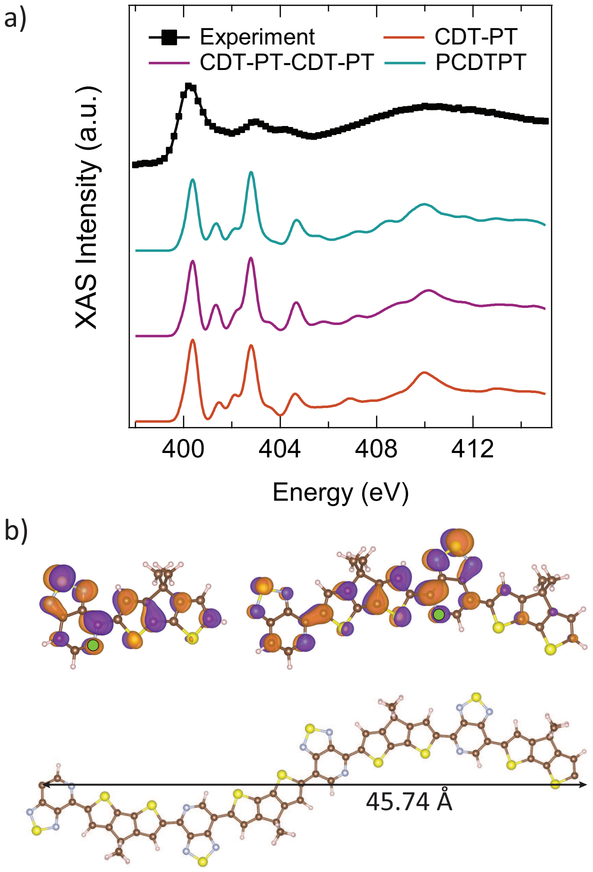

Figure 4.2: Comparison of experimental nitrogen K edge NEXAFS data of the donor-acceptor polymer PCDTPT to simulated spectra of a single CDT-PT fragment, CDT-PT-CDT-PT fragment, and an infinitely long PCDTPT model is shown in (a). Structures of the different molecular models are shown in (b). CDT-PT (top left), CDT-PT-CDT-PT (top right) and a PCDTPT model based on a CDT-PT-CDT-PT unit cell (bottom). Electron density distributions of the lowest unoccupied molecular orbitals overlay the CDT-PT and CDT-PT-CDT-PT molecular models. The excited atom is shown in green.

bone carbon atom it is directly bonded to, and this can affect NEXAFS spectra in the π^* region. It is important to include at least the first atom of the side chain (e.g. a methyl group) in the molecular model to achieve more accurate simulations. An example for sexithiophene with hydrocarbon side chains of varying length is shown in Figure 4.3. Focusing on the C 1s$\rightarrow \pi^*$ region from 284.7 eV to 286 eV, it is clear that the overall spectra (black solid traces) of sexithiophene has a split π^* feature with at least two pronounced peaks. Multiple peaks in the π^* region are also observed experimentally in the NEXAFS of sexithiophene [172]. When methyl, ethyl or hexyl substituents are attached to form sexi(3-methylthiophene), sexi(3-ethylthiophene), or sexi(3-hexylthiophene), the overall spectra in the π^* region shows less splitting, and a more subtle low-energy shoulder that more closely resembles the π^* region in experimental NEXAFS of poly(3-hexylthiophene) (P3HT), as seen in Figure 4.6. To better understand the origin of this change, contributions from individual carbon atoms at different positions on the thiophene unit are plotted (filled color traces) in Figure 4.3. It is clear that for the the carbon atom in the 3-position, when an alkyl group is bonded to it, the energy of its lowest-lying transition increases noticeably. This may be a result of the electron donating nature of the alkyl group that could raise the energy of the LUMO. The π^* manifold is similar in appearance for methyl, ethyl, and hexyl substituents (note all the carbon atoms on the attached side chains were excited). These results reveal the importance of including the first atom on a substituent side chain in models for semiconducting polymers to better reproduce NEXAFS spectra, even in the lower energy π^* region.

The probing depth of NEXAFS experiments can vary, ranging from the entire thickness of a thin film in a transmission experiment to just the top couple nanometers for electron yield, and this can affect relative peak intensities, especially for polymers with pendant side chains. Experimental studies suggest that the electron escape depth near the carbon K edge is only about 2-2.5 nm from the surface in electron yield experiments

[173, 131]. The crystalline packing distance along the side chain extent is typically a similar length scale for many conjugated polymers, for example, about 1.7 nm in P3HT [14, 12], suggesting that potentially up to only a few layers of the conjugated backbone are detected in surface sensitive NEXAFS. The side chains on these polymers, which are typically saturated hydrocarbons that are sometimes very long and/or branched in character, are expected to preferentially segregate to the film surface to minimize free energy. These surface chains are likely to be folded over and not well extended as they may alternatively be within the crystallites of the film. The prevalence of side chains at the surface means that the signal from these atoms will be enhanced in surface sensitive electron yield experiments relative to bulk measurements. Differences in relative peak intensities, for example between $\pi^*_{C=C}$ and σ^*_{C-H} transitions, may arise when comparing electron yield to transmission or fluorescence yield detection modes. Although these surface segregation effects are not accounted for in the simulations here, they are important to consider when looking at experimental data.

4.3.3 NEXAFS Simulations Help Identify Transitions

The NEXAFS spectra of many semiconducting polymers, espeically donor-acceptor polymers, can be very intricate. This is further complicated by the fact that some conjugated polymers exhibit a twist angle between subunits in the backbone. This is important because conjugated polymers tend to preferentially orient in solid state thin films, and this orientation is a critical morphological parameter to understand. In order to probe molecular orientation with polarized X-ray spectroscopy, it is first important to understand the spectra and identify specific transitions, as transitions typically used for orientation analysis have a relatively well defined transition dipole moment direction. Simulations can be very useful for understanding the nature of transition(s) represented in experimen-

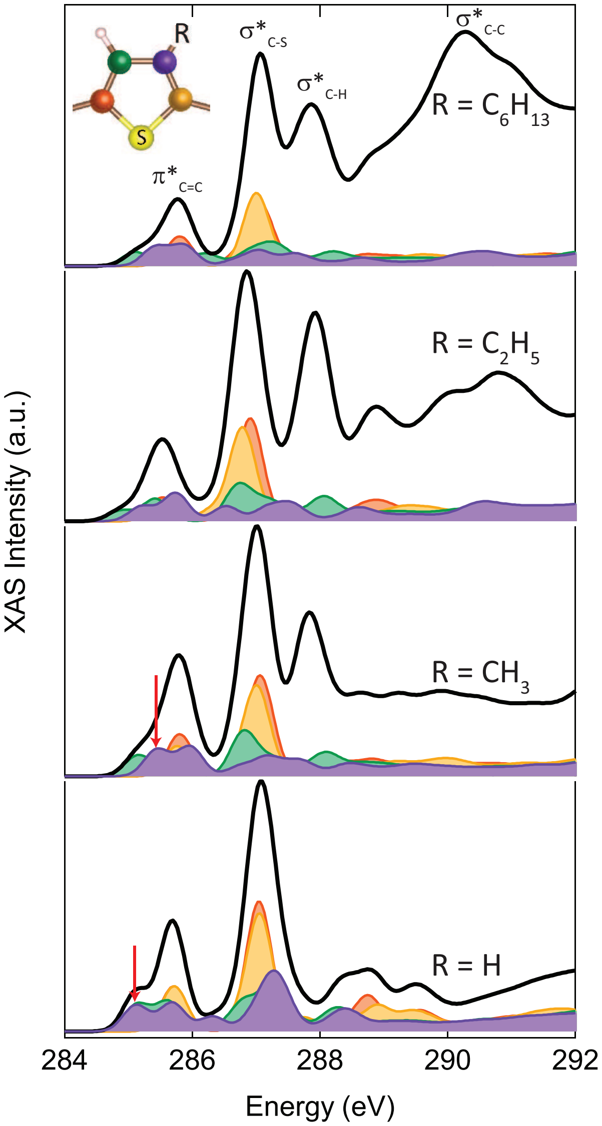

Figure 4.3: Simulated spectra of a sexithiophene model with varying side chain lengths, designated by the *R* group in the schematic. Predicted spectra from bottom to top are no side chain (R = H), methyl side chain (R = CH_3), ethyl side chain (R = C_2H_5), and hexyl side chain (R = C_6H_{13}), respectively. All of carbon atoms on the attached side chains were excited if present. The filled traces show the individual contributions from the four different carbon atoms on the thiophene units. It is clear that the lowest energy transition of the carbon atom bonded directly to the R group shifts to higher energy in the presence of an alkyl side chain.

tally observed peaks of the NEXAFS spectra. XCH calculations can reveal contributions from individual atoms, and show electron density distributions of unoccupied molecular orbitals in the presence of specific excited atoms. An example based on the predicted carbon K edge NEXAFS of the monomer of a furan-containing, diketopyrrolopyrrole-thiophene low-bandgap polymer, PDPP2FT [174], is shown in Figure 4.4.

PDPP2FT contains many distinct carbon atoms with various bonding environments. This results in numerous peaks in the experimental NEXAFS spectra, and is also reproduced in the simulated spectra in Figure 4.4a. Contributions from four different carbon atoms to the overall spectra, and their relative positions in the chemical structure, are shown in Figure 4.4a. The peaks between 284 eV and 286 eV are C 1s→ $\pi^*_{C=C}$ transitions. An example for a transition of C10 that occurs at 284.6 eV is shown in Figure 4.4b. The molecular orbital involved in this transition exhibits electron density above and below the conjugated plane, indicative of π^* character. Similarly, a significant contribution to the peak at about 287 eV is from a C 1s→ $\pi^*_{C=O}$. However, in the simulated spectra, it is apparent that the peak at 287 eV is also largely due to a C 1s→ σ^*_{C-S} transition from the C-S bond in the thiophene unit. This is seen from the molecular orbital that points along the C-S bond (Figure 4.4b). At higher energies, σ^*_{C-H} transitions are evident near 289 eV. This example shows the utility of NEXAFS predictions to help identify specific transitions involved in complicated NEXAFS spectra.

In general, it is expected that the higher the number of distinct atoms, the greater the number of observed peaks since unique bonding environments result in X-ray absorption shifts. Certainly, this seems to be the case for the materials studied here and this also applies to anticipating the number of peaks of a particular nature, e.g. $\pi^*_{C=C}$. Unique energy levels, for example degenerate MOs in organic semiconductors like phenyl-C_{61}-butyric acid methyl ester [175], may also result in multiple $\pi^*_{C=C}$ peaks. Having the ability to predict whether a single or multiple distinct peaks should be present is very

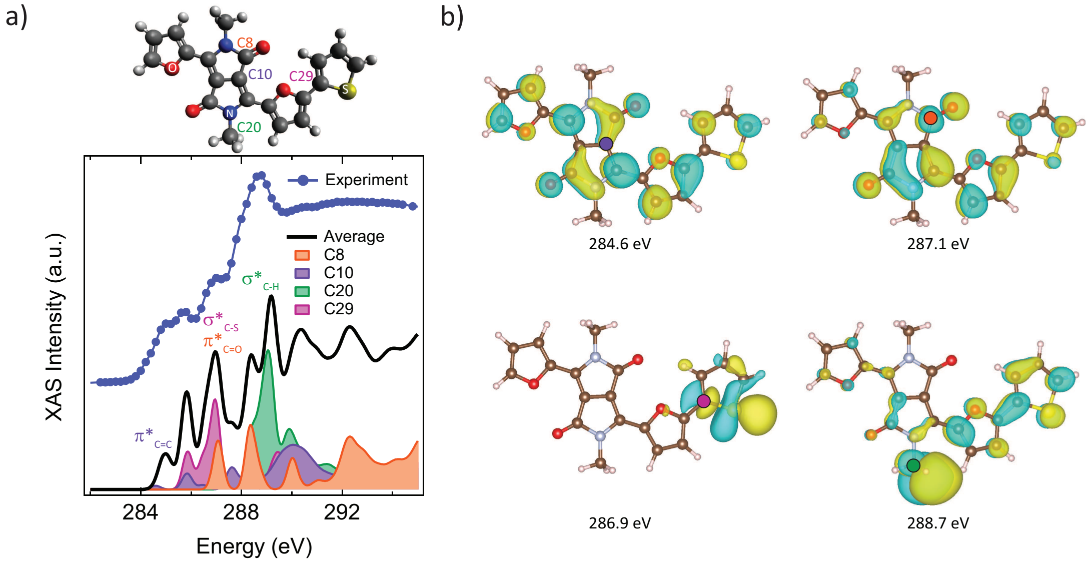

Figure 4.4: Simulated and experimental carbon K edge NEXAFS spectra of PDPP2FT. For the XCH-predicted absorption profile, contributions from four specific carbon atoms are shown in addition to the overall spectra (a). These specific atoms are labelled and color coded on the molecular structure. Electron density distributions of different unoccupied molecular orbitals with corresponding core level excitation energies are shown in (b). These allow for understanding the types of transitions involved in various peaks in the overall spectra.

advantageous to understand acquired data and quickly screen for unexpected results. For example, contamination could cover a sample but result in spectra that still resembles a polymer, as observed in a previous study [166]. This could be diagnosed by knowing the general trends to expect and simulating NEXAFS spectra ahead of time.

4.3.4 Predictions of Angle-Dependent Spectra Reveal Oriented Polymers

Semiconducting polymers due not typically form isotropic thin films. Polymers orient with their chain axis predominantly in-plane with the substrate, and the conjugated plane either mostly edge-on or face-on to the substrate. This is especially apparent in ordered or crystalline regions of the film, as revealed by wide angle X-ray scattering [14]. This preferred orientation means polarized NEXAFS spectra must be carefully considered, especially with regards to relative peak intensities which are affected by transition dipole moments that have a preferred direction. Due to the inherent anisotropic charge transport properties in most semiconducting polymers, the orientation of the polymer chains and backbones are critically linked to charge transport in thin films, making it an important parameter to control. Angle-dependent NEXAFS experiments using polarized X-rays is a common approach to studying molecular orientation in semiconducting polymers. Although general information regarding molecular orientation is typically achievable, the detailed chemical structures of many semiconducting polymers can result in complicated spectral features that can be difficult to assign with NEXAFS experiments alone. The twist angle between subunits of certain low-bandgap polymers makes accurate determination of the tilt angle much more challenging [139]. The ability to predict trends in intensity as a function of incident angle for relevant transitions, especially π^* transitions, is a necessary first step to better understanding intricate experimental results.

The XCH method can reproduce angle-dependent nitrogen K edge spectra for a model system of a highly oriented and aligned PCDTPT thin film. Previous work has shown that PCDTPT thin films cast via blade-coating onto nanogrooved susbstrates produces oriented polymers that are highly edge-on and aligned along the chain axis (or blade coating) direction [166]. Figure 4.5 shows experimental and calculated angle-dependent NEXAFS spectra for the nitrogen K edge of aligned PCDTPT. For the simulated data, an idealized system was assumed where the PCDTPT molecules are perfectly edge-on and perfectly aligned along the chain axis. Furthermore, the electric field vector was restricted to reside in the y-z plane, as shown in Figure 4.5a. This replicates the experimental traces shown in Figure 4.5b where the aligned PCDTPT sample was placed such that the incoming X-ray and electric field vector were perpendicular to the alignment or blade-coating direction. As we have previously shown, the first three peaks in the nitrogen

K edge spectra correspond to 1s→ π^* transitions [166]. The experimental data shows the intensity of these peaks increases with increasing incident angle, indicative of overall edge-on orientation, and this is well-reproduced in the simulated angle-dependent spectra shown in Figure 4.5b. Similar qualitative agreement for angle-dependent spectra near the carbon K edge of PCDTPT is achieved (Figure C.3). Comparison of data and calculated spectra at a given incident angle, for example 51°, reveals good agreement in relative intensities of the lower energy peaks, as shown in Figure C.4.

Simulated angle-dependent spectra also can reproduce experimental trends near the carbon K edge. P3HT is known to be oriented with respect to the backbone tilt, often adopting a mostly edge-on orientation, or a bimodal distribution between edge-on and face-on. Figure 4.6 shows angle-dependent PEY data for a spin coated P3HT thin film, and an overall edge-on orientation is evident by the increasing intensity of the π^* manifold (284-286 eV) with increasing incident angle. The intensity of the feature (σ^*_{C-S} and σ^*_{C-H}) near 288 eV also shows overall increasing intensity with incident angle as typically seen in P3HT [137]. The XCH-predicted angle-dependent spectra, although it assumed a perfectly edge-on and aligned geometry similar to that shown in Figure 4.5a, is able to recreate angle-dependent trends quite well. Simulated spectra are of a sexi(3-hexylthiophene) model in this case. The overall peak shape and intensity changes for the $\pi^*_{C=C}$ region are reproduced very well, supporting the idea of edge-on P3HT backbones. The angle-dependence of the $\sigma^*_{C-S}/\sigma^*_{C-H}$ features near 288 eV is much stronger in the calculated NEXAFS compared to the experimental data. Since much of the contribution to this feature is from the C-H bonds on the side chains, the stronger angle-dependence in the DFT results is presumably a result of the perfectly extended and oriented side chains in the model. Side chains are likely much more disordered, especially near the surface, in the actual thin film sample as discussed earlier. This diminished preferred orientation of the side chains would result in reduced changes in intensity vs. incident angle

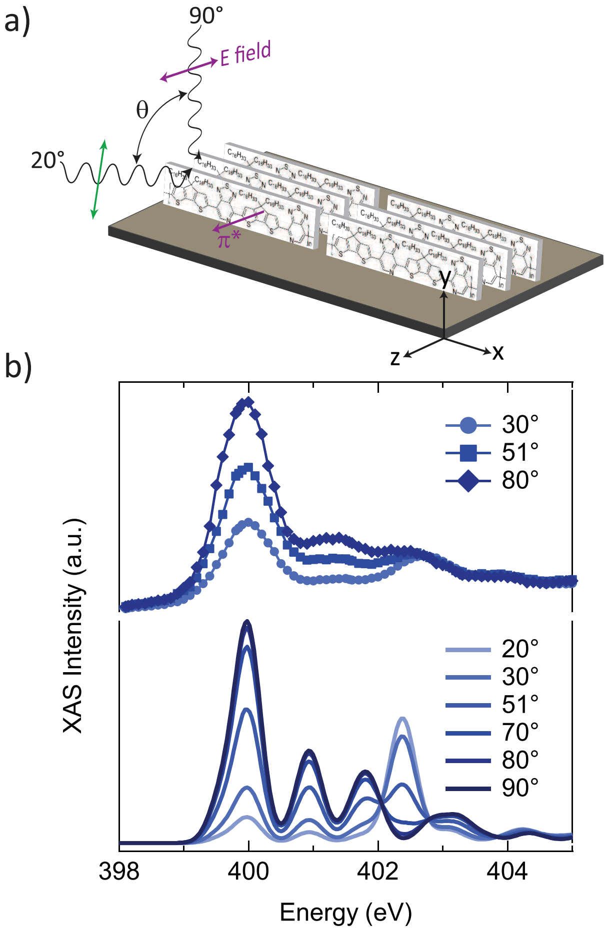

Figure 4.5: Simulated and experimental angle-dependent data for the nitrogen K edge of a model PCDTPT sample. For the calculations, the PCDTPT molecules (CDT-PT-CDT-PT) were assumed to be perfectly aligned and perfectly edge-on, as shown in (a), and the electric field vector direction changed within the y-z plane. Experimental and predicted angle-dependent spectra are shown in (b). Experimental plots shown are surface sensitive partial electron yield data for a PCDTPT sample that was aligned using blade-coating[166], which mimics the model system and geometry used for the calculations.

experimentally. Angle-dependent predictions also illustrate the importance of molecular orientation on relative peak intensities. A clear separation between the σ^*_{C-S} (287.0 eV) and σ^*_{C-H} (287.9 eV) transitions is evident in the simulated 30° trace, but the intensity of the σ^*_{C-H} dominates at angles of 55° and higher, making these transitions harder to distinguish. The predicted spectra at higher incident angles qualitatively match experimental results better. Closer inspection of these peaks in the simulated results show that for this orientation and aligned geometry, the σ^*_{C-S} transition shows the opposite trend with incident angle, i.e. its intensity decreases with increasing incident angle, compared to the σ^*_{C-H} transition. Again, keep in mind that a peak width of 0.2 eV was applied to all transitions in the simulations. This level of detail is difficult to see in the experimental spectra alone, especially since the σ^*_{C-S} and σ^*_{C-H} transitions are relatively close together and the greater intensity of the σ^*_{C-H} peak dominates, and this exemplifies the utility of combining complementary simulations with experimental data.

Orientation analysis is even more troublesome for semiconducting polymers that exhibit a tilt angle between subunits in the backbone [139], and the ability to simulate angle-dependent data will also prove useful for these more complicated molecules. [N,N-9-bis(2-octyldodecyl)naphthalene-1,4,5,8-bis(dicarboximide)-2,6-diyl]- alt-5,59-(2,29-bithiophene), P(NDIOD-T2), is a well-studied donor-acceptor polymer that is known to have a dihedral angle between the NDI donor unit and thiophene acceptor unit, thought to be about 47° [176, 177]. Experimental investigations of P(NDIOD-T2) show an overall angle-dependent intensity of the π^* peaks in the carbon K edge, and it is expected that the two outer peaks in the π^* region correspond to the NDI units, while the middle peak is due to the thiophene units [139]. NEXAFS calculations on a single repeat unit of P(NDIOD-T2) suggest that there are likely transitions in the entire π^* energy range that arise from various carbon atoms on the NDI unit, and similarly for the thiophene units (Figure C.5). Furthermore, due to the dihedral angle, transition intensities in the π^* region originating

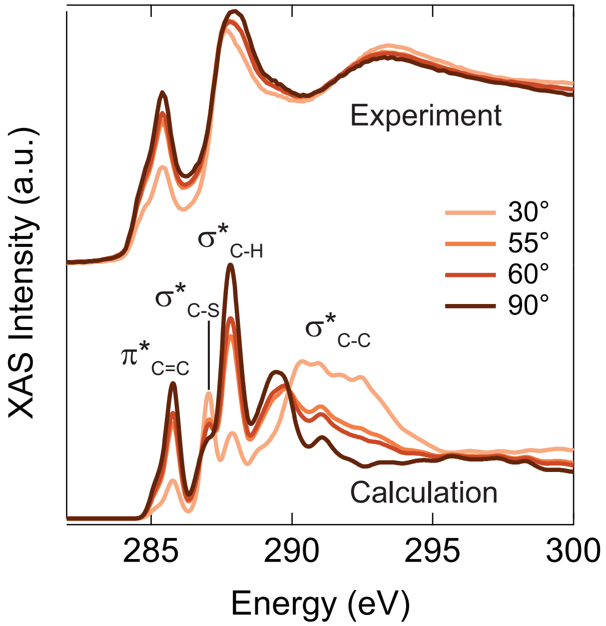

Figure 4.6: Simulated and experimental angle-dependent data for carbon K edge of P3HT. Experimental plots shown are surface sensitive partial electron yield data. Simulated spectra are for a sexi(3-hexylthiophene) model with perfect edge-on and chain axis alignment.

from atoms residing on the NDI unit will have a different angle-dependence compared to the spectra from the thiophene atoms (Figure C.5). Experimentally, these differences in angle-dependent intensities may be hard to distinguish since polymers in a sample may not have perfectly uniform alignment, and there can be a significant contribution to NEXAFS spectra from amorphous material. This emphasizes the challenges present in complicated orientation analysis with experimental data alone and the potential for complimentary simulations to help understand polymer microstructure.

The propensity of conjugated polymers to orient in the solid state demands judicious attention to polarized NEXAFS studies. Angle-dependent NEXAFS experiments are certainly a valuable tool for probing molecular orientation, and complementary simulations are integral to gaining a more complete picture. However, it is important to consider the main tendencies of semiconducting polymers, e.g. chain axis in-plane with the substrate, when comparing experiment and theory. Calculations on even highly idealized models can provide useful feedback relevant to experimental results, especially in terms of relative peak intensities. Many organic electronic applications, for example organic photovoltaics, consist of blends of organic semiconductors, and NEXAFS can be very useful in estimating composition in thin films [150, 151]. Appreciating the effects of molecular orientation, especially if polarized X-rays are used, it is also important to consider if overall orientation changes for a specific material when comparing pristine, single component samples to blend films. A change in orientation could affect analysis when spectra of pristine samples are used to estimate blend composition.

4.3.5 NEXAFS Spectroscopy Reveals the Molecular Orientation in Blade-Coated Pyridal[2,1,3]thiadiazole-Containing Conjugated Polymer Thin Films

In semiconducting polymers, transport along a conjugated polymer backbone is efficient because of the strong electronic coupling between monomers. However, it is nontrivial to align films where the fast transport direction is oriented along the direction of charge transport. Many techniques have been applied to obtain aligned films where the charge carrier mobility is maximized. Some of these methods include using a rubbed polyimide surface as an alignment layer [178, 179], directional crystallization [180], high temperature rubbing [181], and zone-casting or blade-coating methods [182, 140].

Uniaxial nanogrooved substrates can be used as a topographic guide for the alignment of polymers. Rubbing a substrate (Si/SiO_2) with a diamond lapping paper generates uniaxial nanogrooves, which are approximately 50-100 nm in width and a few nm in depth [183]. Recent work has focused on the alignment of regioregular PCDTPT [184], a donor-acceptor copolymer of a cyclopenta[2,1-b:3,4-b]dithiophene (CDT) donor unit and a [1,2,5]thiadiazolo[3,4-c]pyridine (PT) acceptor unit. In this work, a more rapid blade coating method (doctor blading) was employed to generate aligned thin-films of PCDTPT using nanogrooved substrates. We quantify the resulting alignment at both the buried substrate (bottom-side) and air (top-side) interfaces of these films using NEXAFS spectroscopy.

Charge transport in thin film transistors occurs in a thin interfacial region, on the order of one to two molecular layers, at the gate dielectric [185]. It is therefore important to study molecular orientation at such interfaces as well as the bulk. Polarization-dependent NEXAFS spectroscopy is a useful tool to probe the molecular orientation at the surface of conjugated polymer thin films [137].

In this work, we present carbon and nitrogen K edge NEXAFS spectra for PCDTPT and theoretical calculations of the spectra that help facilitate assignment of the experimental data. Using polarization-dependent NEXAFS data, we calculated the order parameters S, describing the out-of-plane orientation of the conjugated plane relative to the surface normal (i.e. “edge-on” or “face-on”), and η, describing the extent of in-plane orientation of the conjugated polymer-chain axis relative to the alignment direction). This is described in detail by Patel et al [166]. We observe that in all films the conjugated plane has a preferential “edge-on” orientation. In addition, we find significant in-plane orientation in these films demonstrating the utility of the nanogroove method to induce alignment of solution processed semiconducting polymers.

As discussed earlier, it can be difficult to assign transitions in NEXAFS spectra based on experimental data alone. The most common elemental edge used for polymers is the carbon K edge due to the large number of carbon atoms. However, the many distinct carbon atoms present in polymers can lead to complicated carbon K edge spectra that is difficult to understand. Other elemental edges can be especially useful and simpler to interpret. PCDTPT also contains nitrogen atoms, and there are only three distinct

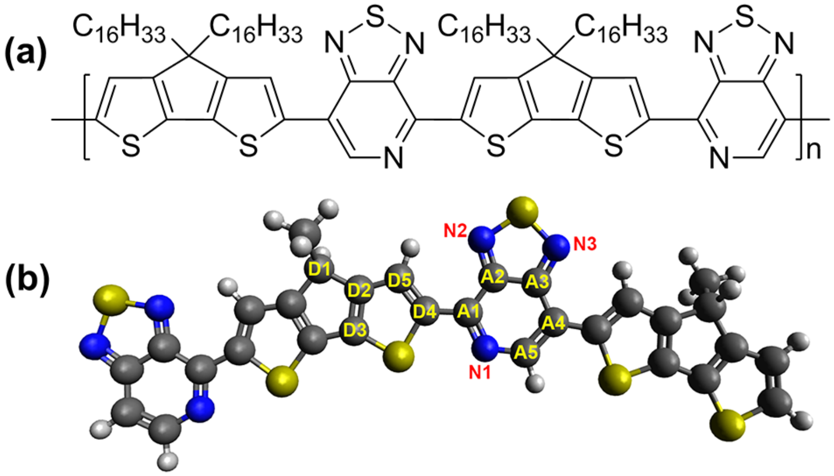

Figure 4.7: (a) Chemical structure of regioregular PCDTPT. (b) DFT-optimized structure showing PT-CDT-PT-CDT repeat unit (with methyl side chains). Each unique carbon is labeled for both the CDT unit (D1-D5) and PT unit (A1-A5). PT = [1,2,5]thiadiazolo[3,4- c]pyridine acceptor unit, and CDT = cyclopenta[2,1-b:3,4-b]-dithiophene donor unit.

nitrogen atoms on the PT acceptor unit (Figure 4.7). Due to this inherent simplicity, focus is placed on understanding contributions and transitions of the nitrogen K edge of PCDTPT, which is the basis for understanding polymer chain alignment in the blade-coated films.

Theoretical predictions of the nitrogen K edge of PCDTPT using the XCH method do a good job of reproducing the experimental data, as shown in Figure C.4. The simulated spectra can be broken down to determine which specific nitrogen atoms contribute the most to certain peaks, as shown in Figure 4.8. Furthermore, it is clear that the degree of delocalization of the unoccupied molecular orbital involved in the lowest energy transition varies significantly depending on which nitrogen atom is excited.

To help identify the nature of the transitions involved in certain peaks (e.g. π^* or σ^*), knowledge of contributions to the intensity as a function of direction of the electric field vector of the incoming X-ray is needed. This is shown in Figure 4.9. Since it is known that $\pi^*_{C=C}$ transitions point perpendicular to the conjugated plane (± z-direction in this

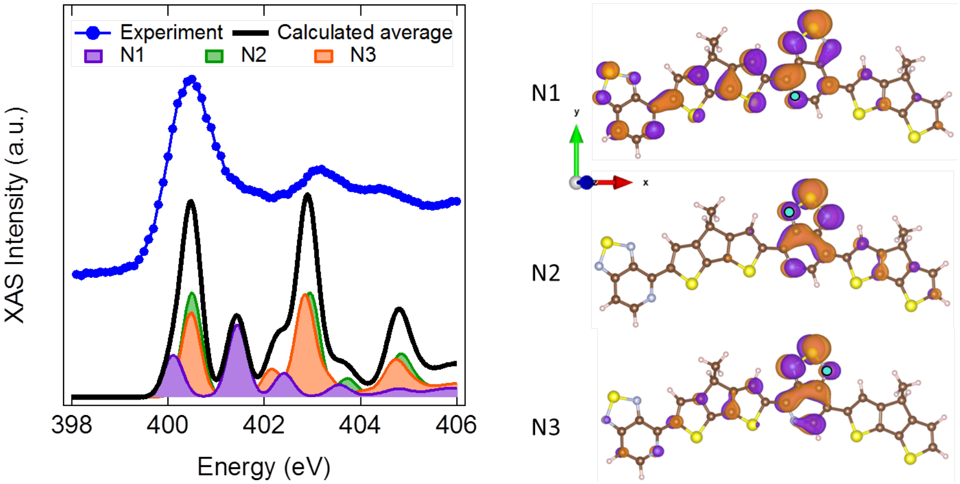

Figure 4.8: Simulated nitrogen K edge NEXAFS of PCDTPT and contributions from the three distinct nitrogen atoms on the PT acceptor unit. Molecular orbitals for the excited state corresponding to the first π-resonance of each nitrogen atom (N1 = pyridal unit, N2 and N3 = thiadiazole unit) are shown on the right.

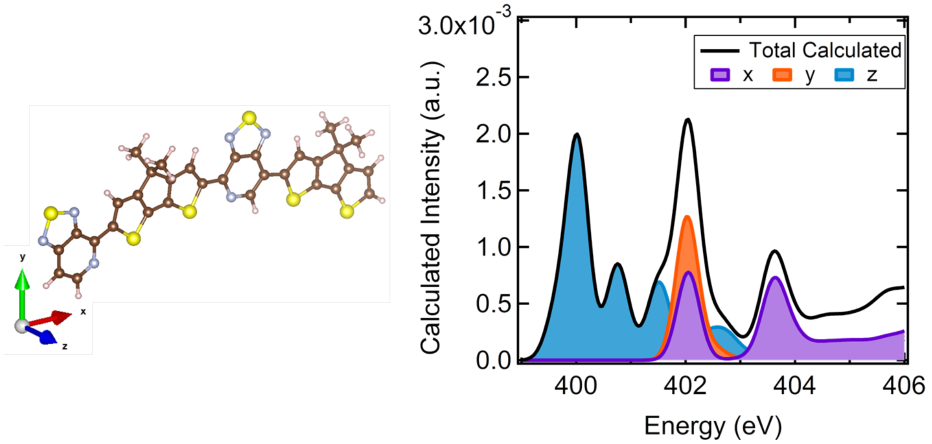

Figure 4.9: Simulated nitrogen K edge NEXAFS of PCDTPT and contributions to the intensity assuming the electric field vector points along the polymer chain axis (x), along the side chain stacking extent (y), or perpendicular to the conjugated plane (z).

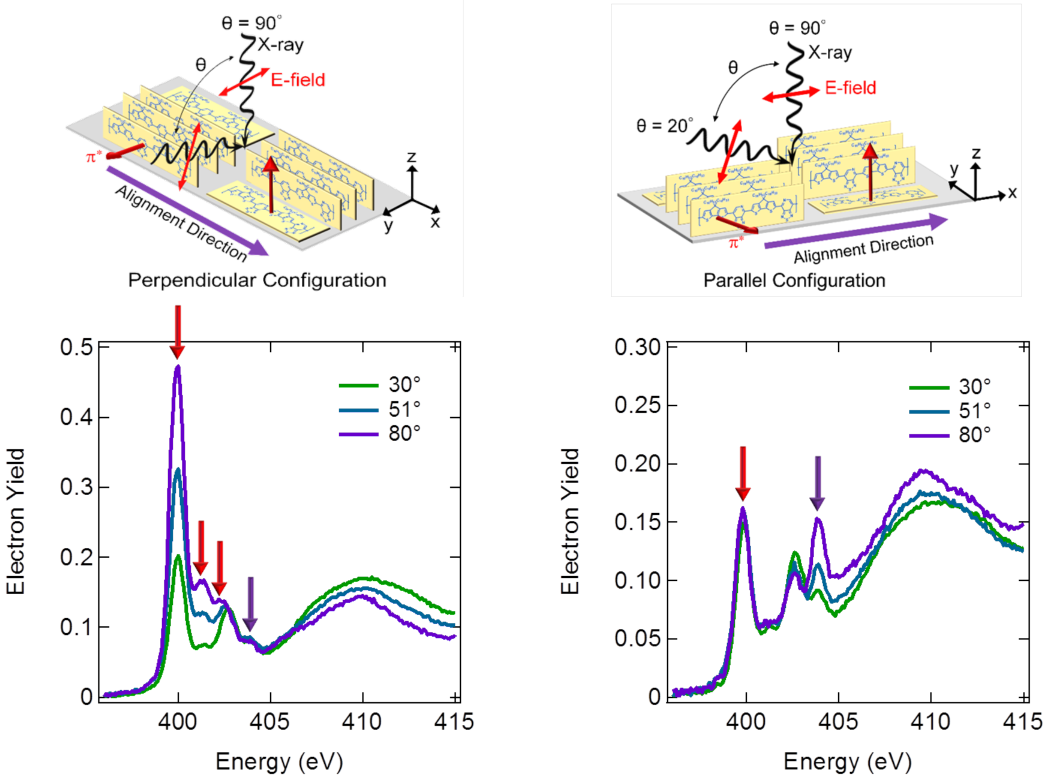

Figure 4.10: Schematics show the geometry of the perpendicular and parallel sample configurations with respect to the incoming X-ray. Angle-dependent data at the nitrogen K edge for each configuration reveals that PCDTPT polymers are edge-on and aligned along the blade-coating direction at the buried interface.

case), it is expected that the first three peaks are in fact $\pi^*_{C=C}$ transitions. Additionally, the higher energy peak around 403.5 eV seems to have a transitions dipole moment pointed primarily along the polymer chain axis.

Experimental angle-dependent NEXAFS results confirm the alignment of polymer chains at the buried interface of blade-coated PCDTPT thin films, and support the assignments determined from the predicted spectra. Angle-dependent data was collected in two sample orientation, perpendicular and parallel. In the perpendicular configuration, the electric field vector is always perpendicular to the alignment (chain axis) direction. In the parallel configuration, the electric field vector is parallel to the alignment direction at an incident angle of 90 °, and perpendicular to the alignment direction at 0 °. This is depicted schematically in Figure 4.10. In the perpendicular geometry, it is clear that the intensity of the first three peaks increases with increasing incident angle. Since these are π^* transition, this confirms that PCDTPT adopts an overall edge-on orientation. However, the higher energy backbone direction peak shows no angle-dependent change in intensity. This is expected if the polymer chains are primarily pointed along the alignment direction. In the parallel configuration, the opposite trends are seen. The π^* peaks do not change in intensity as a function of incident angle, but the intensity of the backbone direction peak increases with increasing incident angle. These results verify a high degree of polymer orientation and alignment as a result of blade-coating on nanogrooved substrates, and showcase the utility of NEXAFS simulations to assist in understanding experimental results.

4.4 Conclusion

NEXAFS spectroscopy has become an important technique to probe electronic structure and reveal morphological information, for example molecular orientation, in semiconducting polymers. Predictive power using computational methods is critical for understanding details that cannot easily be determined based on experimental data alone, allowing for improved materials characterization. However, only limited work has been done to simulate NEXAFS spectra of semiconducting polymers. Here, we have shown that the eXcited electron and Core Hole (XCH) approach, based on constrained-occupancy density functional theory, is well-suited to predict X-ray absorption spectra of semiconducting polymers at multiple elemental edges, including the carbon and nitrogen K edges. This approach takes advantage of periodic boundary conditions and can model infinitely long polymer chains, however, NEXAFS spectra are reasonably well reproduced based on models of appropriately sized molecular fragments. When modelling semiconducting polymers, it is important to include at least the first atom of the side chains bonded directly to the conjugated core, as the presence of the these substituents can noticeably shift the energy of low-lying, but very important, C 1s→ π^* transitions. In general, the number of distinct peaks in an observed NEXAFS spectra, even for a given type of transition such as $\pi^*_{C=C}$, depends on the number of distinct atoms with unique bonding environments. Simulations make it possible to readily identify the nature of these transitions by examining contributions from individual atoms and electron density distributions of molecular orbitals. Furthermore, the preferred orientation that semiconducting polymers tend to adopt in thin films necessitates the ability to calculate angle-dependent spectra on model aligned polymers. This reveals important trends in relative angle-dependent peak intensities, and is essential for a better understanding of molecular orientation, especially in systems that exhibit complicated spectral features and/or a dihedral angle between subunits in the backbone. Looking ahead, the enhanced understanding of X-ray absorption spectroscopy afforded by complementary computation will enable improvements in characterization with X-ray microscopy and resonant X-ray scattering, which are becoming increasingly popular for organic semiconductors. We hope to provide groundwork of important parameters to consider when dealing with NEXAFS data. Overall, the ability to simulate NEXAFS spectra using a method like the XCH approach that is tractable by experimentalists is essential in improving the ability to determine important electronic and structural parameters and allow for more efficient and focused synchrotron experiments on semiconducting polymers and polymers in general.

Chapter 5

Conclusions

The ability to understand and control the microstructure and morphology in the active layer of organic electronic devices is critical for further improving performance and creating the next generation of advanced materials. Proper characterization of organic semiconductor thin films requires the ability to probe a large range of length scales. Synchrotron X-ray methods are able to elucidate important morphological features, and when combined with other characterization tools, simulations, and device data a thorough understanding can be gained.

First, we examined a complex blend of a polymer (P3HT) and small molecule (DTI) applicable to solar cells that demonstrates how structure in the thin film, specifically molecular orientation, directly impacts device performance. Thermal annealing results in a significant decrease in solar cell efficiency for this material system. This is attributed to a drastic reorientation of DTI molecules in the blend upon annealing. DTI exhibits preferred directions for charge transport, and thermal annealing results in highly edge-on molecules that block vertical electron transport and limits solar cell performance.

Second, we provide an example of how the chemistry of a semiconducting polymer impacts phase separation in a polymer blend. A model polymer blend consisting of a ferroelectric polymer (PVDF-TrFE) and a semiconducting polymer (P3EPT) that can be used to form resistive switches for non-volatile memristors was studied. One of the goals for improving these types of devices is to reduce the phase separation length scales and understand the three-dimensional morphology in these thin films. By tuning the chemical structure of the side chain of the semiconducting polymer, smaller and more controllable domain sizes were achieved. Furthermore, potential enhancement of semiconducting polymer at the film surface was observed, and this is an important parameter that should be considered in the design of organic ferroelectric resistive switches.

Finally, an example of how computational modelling can characterization fo semiconducting polymers was demonstrated. First-principles simulations of X-ray absorption spectroscopy of semiconducting polymers were shown to be essential in improving understanding of experimental data and characterization abilities. The eXcited electron and Core Hole (XCH) approach, based on constrained-occupancy density functional theory, can predict X-ray absorption spectra of semiconducting polymers, make use of periodic boundary conditions, and is tractable by experimentalists. We examined a system of a blade-coated donor-acceptor polymer, and the ability to calculate the absorption spectra proved critical in identifying the nature of specific transitions to probe the alignment in these films.

Many aspects of the thin film morphology of organic semiconductors, including molecular orientation, phase separation length scales, and surface segregation, are important to understand and control to further improve the efficiency of relevant devices. This work reveals certain morphological parameters that need to be taken into account when designing the next generation of materials, and how these parameters are affected by aspects such as chemical structure and processing conditions. Furthermore, the ability to complement experimental characterization with proper simulations is critical for advancing materials discovery and development.

Appendix A

Supporting Information Chapter 2

A.1 Experimental Procedures

A.1.1 Fabrication of Photovoltaic Devices

Poly(3-hexylthiophene) (P3HT) was obtained from Rieke Metals (Sepiolid P200). DTI was synthesized as reported by Pho et al [31]. Pre-patterened ITO-coated glass substrates were cleaned by sonicating in alconox:water, water, acetone, and isopropanol sequentially for 20 mins each. The substrates were dried with a stream of N_2 and exposed to oxygen plasma for ∼5 mins. PEDOT:PSS (Clevios PVP Al 4083) was spin coated at 4000 rpm for 45 s onto the cleaned glass/ITO substrates, and dried at 160 °C for 20 min. The P3HT:DTI solutions (1:1 by weight) were prepared with a total concentration of 20 mg mL^{-1} in o-dichlorobenzene with 1-chloronaphthalene (2% by volume) and stirred at 80 °C overnight. The P3HT:DTI solution was filtered (0.45 μm PTFE filter) directly onto the substrate in a N_2 filled glove box, and the substrate was spun at 1000 rpm for 60 s and then 2000 rpm for 10 s, yielding an active layer thickness of ∼100 nm. The wet films were allowed to dry at room temperature for 20 mins. A 1 nm thick layer of

LiF followed by ~90nm of Al was thermally evaporated on top of the active layer under vacuum (¡10^{-6} torr). The active area of the devices was 0.06 cm^2, and current-voltage (J-V) characteristics were measured at 1 sun (AM 1.5G) in a N_2 filled glove box with a Xenon lamp (Newport) and a Keithley 2408 Source Measure Unit (SMU).

Electron-only diodes were fabricated in a similar way as the OPV devices. ITO-coated glass substrates were cleaned in the same way, but instead of PEDOT:PSS, a 90 nm layer of Al was thermally evaporated onto the glass/ITO substrates, followed by spin casting of the P3HT:DTI active layer. Finally, a 25 nm layer of Ca and a 90 nm layer of Al were evaporated on top of the active layer. Current-voltage measurements were performed in the dark. Hole-only diodes were fabricated similarly to the OPV devices, except a 90 nm layer of Au was evaporated onto the active layer instead of LiF/Al.

A.1.2 Differential Scanning Calorimetry (DSC)

DSC measurements were carried out on a TA Instruments DSC 2920 differential scanning calorimeter. About 4 mg of material was loaded into a Tzero aluminum pan. Each samples was first equilibrated at 25 °C, then heated to 270 °C, cooled to 0 °C, and heated again to 270 °C. All of the heating and cooling cycles were done at a rate of 10 °C/min. An empty Tzero pan was used as a reference.

A.1.3 Grazing Incidence Wide Angle X-ray Scattering (GIWAXS)

Samples were prepared for GIWAXS by spin-coating solutions of DTI or P3HT:DTI blends onto PEDOT:PSS coated Si substrates using the same deposition conditions as for the photovoltaic devices. GIWAXS experiments were performed at the Stanford Synchrotron Radiation Lightsource (SSRL) at beamline 11-3. A MAR 2300 area detector was used for 2D diffraction pattern collection. The energy of the incident beam is 12.7

keV. The angle of incidence used was 0.11° and the sample-to-detector distance was 40 cm. Samples were kept in a helium atmosphere to minimize X-ray damage and background scattering. Exposure times were typically bewteen 30 s and 120 s. Beamline 11-3 is equipped with a heating stage that allows for GIWAXS scans to be taken at temperature for *in situ* studies.

A.1.4 Near Edge X-ray Absorption Fine Structure (NEXAFS)

Samples for NEXAFS were prepared by spin-coating onto Si/PEDOT:PSS substrates, just as for GIWAXS. NEXAFS experiments were performed at beamline U7A at the National Synchrotron Light Source (NSLS). The incident X-ray beam was elliptically polarized (polarization factor = 0.85) with the electric field vector predominantly in the plane of the storage ring. The incident angle, θ, was varied between 30° and 90°, where 90° refers to an incident X-ray beam that is perpendicular to the substrate. A spherical grating monochromator was used to select soft X-rays in the range from 280 eV to 440 eV, corresponding to the carbon and nitrogen K edges. The partial electron yield (PEY) data was collected with a channeltron electron multiplier with an adjustable entrance grid bias that was set to -150 V. All experiments were done in a UHV chamber. Carbon edge PEY and fluorescence yield (FY) data were normalized by subtracting a linear pre-edge baseline and setting the edge jump to unity at 325 eV.

A.1.5 Resonant soft X-ray scattering (RSoXS)

RSoXS was performed at beamline 11.0.1.2 at the Advanced Light Source (ALS). Samples were prepared by spin coating P3HT:DTI blends onto Si/SiO$_2$/PEDOT:PSS substrates, using the same conditions as for devices, and then floating onto 1.5 mm x 1.5 mm, 100 nm thick Si$_3$N$_4$ membranes supported by a 5 mm x 5 mm Si frame

(Norcada Inc.). 2D scattering was collected in a transmission geometry with a sample-to-detector distance of 160 mm. Data was collected on an in-vacuum CCD camera (Princeton Instrument PI-MTE) cooled to -45 °C. 2D scattering data was then reduced by azimuthal averaging of the scattering data over all q values. The RSoXS profiles shown in the manuscript were taken at 284.4 eV, an energy where there is a significant absorption difference between P3HT and DTI. Details of the specifics of this beamline have been reported elsewhere [23].

A.1.6 Dynamic secondary ion mass spectrometry

Experiments were performed on a Physical Electronics 6650 Quadropole dynamic SIMS. A 2 kV O^{2+} primary ion beam at $\sim$45 nA was used and rastered over a 200μm × 200 μm area and secondary ions were only collected from the middle 15% of this area. Si/SiO_2 substrates were used with a final sample geometry of Si/SiO_2/PEDOT:PSS/P3HT:DTI/PS.

A.2 Molecular Geometry of DTI

Similar to decacyclene, DTI is found to have a gently twisted propeller geometry, as shown in Figure A.1. Considering this, it is reasonable to expect DTI molecules to stack one on top of the other. However, adjacent molecules may need to twist to reduce steric interactions.

A.3 Effect of Annealing on Device Performance

As discussed in the manuscript, thermal annealing leads to significant decreases in power conversion efficiency (PCE) of P3HT:DTI devices when annealed at 120 °C for

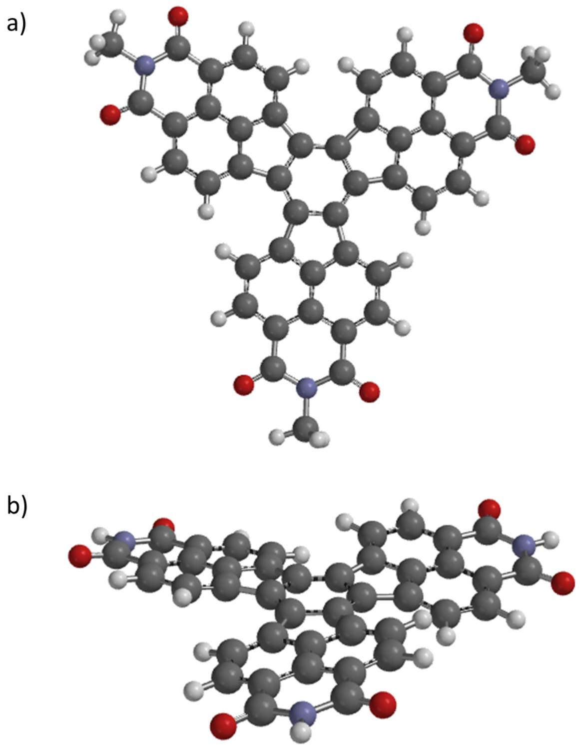

Figure A.1: Molecular geometry of DTI calculated with DFT using the B3LYP/6-31G* level of theory. The octyl side chains were replaced by methyl groups. A top-down view is shown in (a), and a side-view in (b).

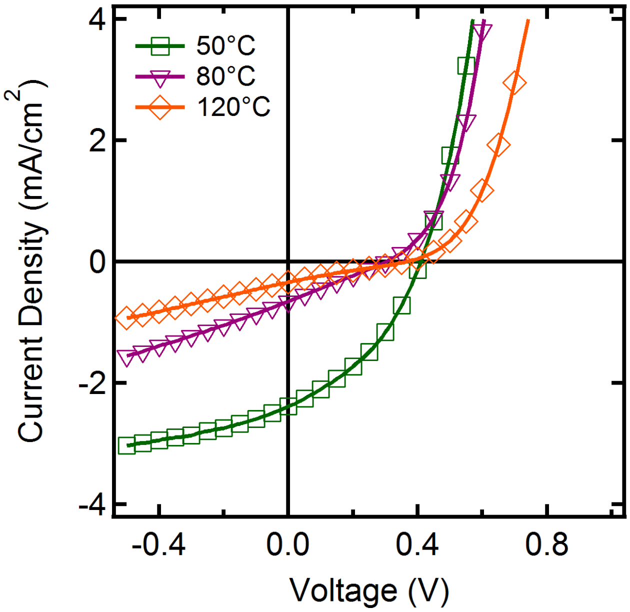

Figure A.2: Current density vs. voltage curves for P3HT:DTI solar cells annealed at 50 °C (green squares), 80 °C (purple triangles), and 120 °C (orange diamonds).

20 minutes, as shown in Figure 1. Furthermore, devices annealed at lower temperatures also exhibited diminished PCEs. For devices fabricated with a geometry of ITO/PEDOT:PSS/P3HT:DTI/Al (which has an overall lower efficiency), PCEs of 0.37%, 0.05%, and 0.03% were measured for annealing temperatures of 50 °C, 80 °C, and 120 °C, respectively (Figure A.2)

A.4 Surface Topography with Atomic Force Microscopy

AFM experiments were performed on an Asylum Research MFP 3D AFM using NanoWorld Pointprobe Al-coated noncontact mode Si cantilevers with a spring constant of 48 N/m and a resonant frequency of 190 kHz. Surface topography of pristine DTI films and P3HT:DTI blends were investigated. Height images are shown in Figure A.3. Large crystals are evident after thermal annealing of pristine DTI. However, blend films show relatively little difference in height topography beyond a slight increase in rms roughness

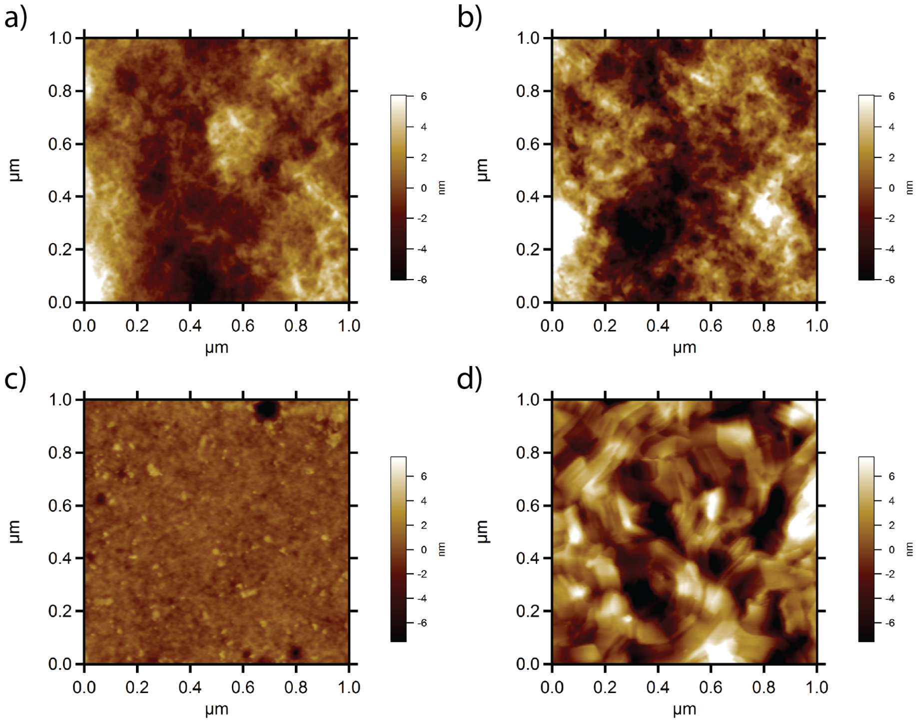

Figure A.3: AFM height images of (a) an as-cast P3HT:DTI blend film, (b) an annealed (120 °C) P3HT:DTI blend film, (c) an as-cast pristine DTI film, and (d) an annealed pristine DTI film.

from ∼2.1 nm to ∼2.8 nm for as-cast and annealed blends, respectively.

A.5 Photoluminescence Quenching

Photoluminescence (PL) quenching is commonly used to estimate the degree of charge transfer between materials in a blend upon photoexcitation. PL (Horiba FluoroMax-4 Spectrofluorometer) of as-cast and annealed P3HT:DTI blends excited at 430 nm (where absorption is dominated by DTI) and 570 nm (absorption dominated by P3HT) is shown in Figure A.5.

It is clear that the PL intensity is much less in the annealed film excited at 430 nm, suggesting improved charge transfer from DTI to P3HT upon annealing. Based on the PL spectra of the blend films and pristine P3HT and DTI, it is estimated that the PL

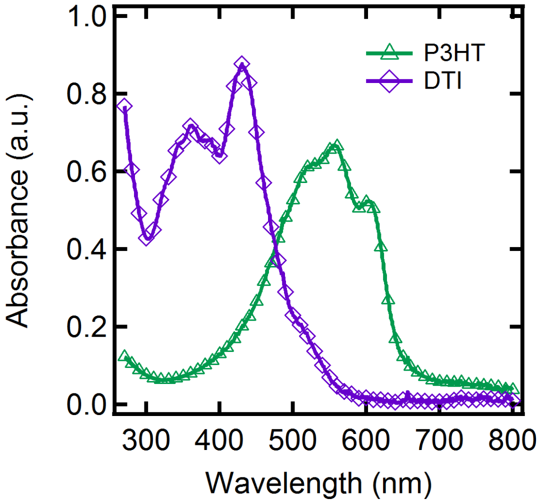

Figure A.4: UV-Vis absorption of DTI and P3HT thin films.

from DTI is 76% and 90% quenched for the as-cast and annealed P3HT:DTI blends, respectively. Although DTI crystallite size increases with annealing, enhanced charge transfer from DTI to P3HT is suggested from the increased PL quenching. This could be due to a large exciton diffusion length along the column direction of ordered columnar liquid crystals (up to about 60 nm) [62], or energy transfer from DTI to P3HT. The PL quenching of P3HT (excited at 570 nm) did not change significantly, decreasing from 60% P3HT quenching in the as-cast blend film to 53% in the annealed film. It is not surprising that charge transfer from P3HT to DTI is marginally reduced with annealing since P3HT domains become slightly larger (see Figure A.18).

A higher degree of PL quenching is typically linked to improved solar cell performance due to enhanced charge transfer. However, the annealed P3HT:DTI solar cells have much lower efficiencies. This suggests that annealing does not reduce charge transfer and separation between P3HT and DTI, but rather these separated charges cannot be extracted to the contacts due to morphological aspects including molecular orientation and domain separation.

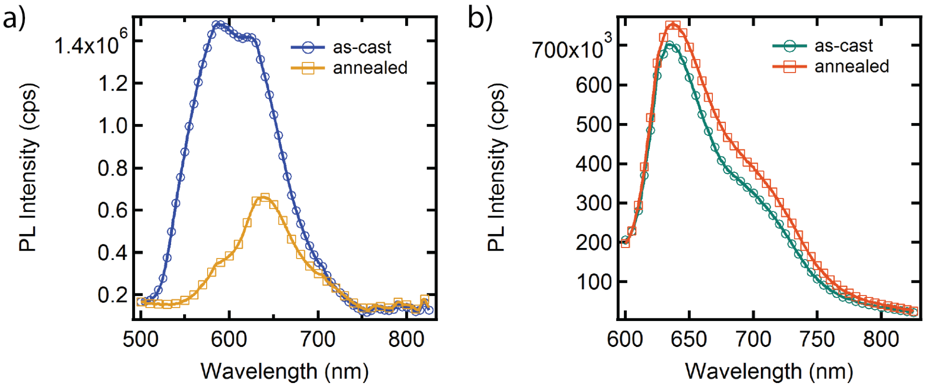

Figure A.5: Photoluminescence spectra of as-cast and annealed P3HT:DTI thin films excited at (a) 430 nm and (b) 570 nm.

A.6 Near Edge X-ray Absorption Fine Structure (NEXAFS)

A.6.1 Carbon K Edge Spectra for P3HT and DTI

Organic semiconductors, which contain mainly carbon atoms and have many double bonds, exhibit rich spectra around the carbon K edge. The PEY spectra around the carbon K edge for pristine DTI and pristine P3HT is shown in Figure A.6. Clear transitions from core electrons to π^* antibonding orbitals are visible as peaks near 285 eV. Higher energy peaks correspond to transitions to σ^* antibonding orbitals.

A.6.2 Surface Composition

An estimate of the surface composition of the P3HT:DTI blends can be determined by fitting the NEXAFS spectra of the blend film with a linear combination of the spectra from individual components. Estimates on surface composition are shown in Figure A.7. There is no drastic change in surface composition between as-cast and annealed blends, considering that the π^* peak of P3HT overlaps with one of the π^* peaks of DTI, which

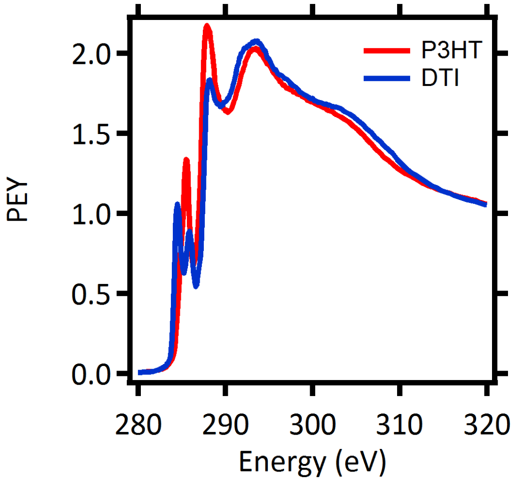

Figure A.6: PEY NEXAFS spectra for P3HT (red curve) and DTI (blue curve) at energies near the carbon K edge. The incident angle was 55°.

can complicate the fitting. Nevertheless, the result suggests the possibility that there is a slight excess of P3HT on the surface of the as-cast film, and the relative amount of P3HT on the surface decreases with annealing, as indicated in the DSIMS.

A.6.3 Probing Molecular Orientation with NEXAFS

NEXAFS experiments can probe molecular orientation due to the inherent polarization of the X-ray beam and the tunability of the incident angle. Organics often have anisotropic molecular orbitals and transitions to these orbitals can have dipole moments in a specific direction [18, 19]. A π^* transition can typically be described by a vector that is perpendicular to the conjugated ring plane. The intensity of this peak will be greatest when the electric field vector of the X-ray is aligned with the direction of the π^* transition vector, and lowest when these two vectors are perpendicular, as depicted schematically in Figure A.8.

Overall molecular orientation can be probed by changing the incident angle and tracking the total intensity of a specific transition. For different angles of the X-ray relative

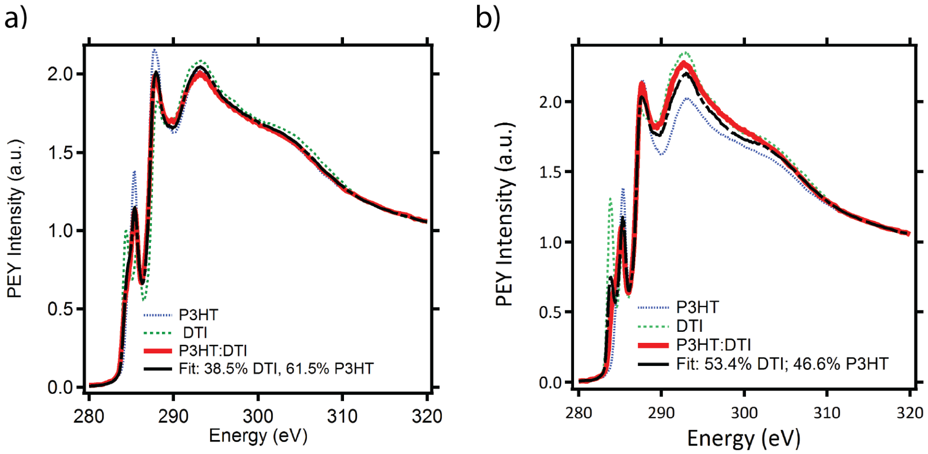

Figure A.7: Surface composition fits for (a) an as-cast P3HT:DTI blend and (b) an annealed (120 °C) P3HT:DTI blend. Fits are based on a linear combination of the spectra of pure components. The incident angle was 60°.

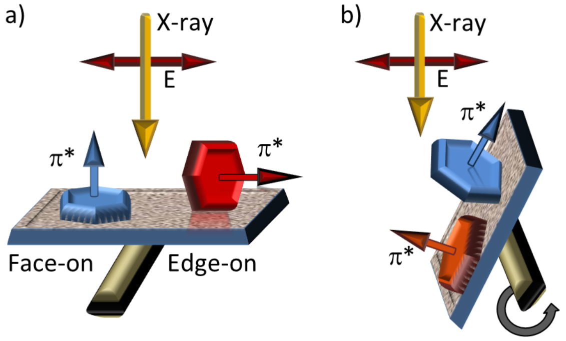

Figure A.8: Schematic depicting the effect of incident angle on the intensity of a specific transition. Molecules that have a well defined transition dipole vector (in this case a π^* transition) will have the greatest intensity of that transition at an angle when it is in-line with the electric field vector, E. Here, we see that an edge-on molecule with a π^* transition parallel to the substrate surface will have a high π^* transition intensity when (a) the incident X-ray is perpendicular to the substrate ($\theta = 90°$) and lower when (b) the incident beam is more parallel to the substrate. The opposite would be true for a face-on molecule.

to the substrate plane, θ, the PEY intensity of an X-Y bond is expected to vary linearly with $sin^2(\theta)$, as given by,

$$I_{XY}(\theta) = a_{XY} + b_{XY} sin^2(\theta).$$

Hence, molecular orientation can be quantified by plotting the total intensity vs. $sin^2(\theta)$. Based on a linear fit to this data, an orientation order parameter, S, can be determined as follows [17],

$$S = -\frac{P^{-1} b_{xy}}{3a_{xy} + (3 - P^{-1}) b_{xy}},$$

where P is the polarization factor of the X-ray beam, in this case 0.85. S ranges from +1 for a transition dipole moment along the surface normal (face-on for a π^* transition) to -1/2 for a transition dipole moment in the plane of the substrate (edge-on for a π^* transition). Since S is based on the linear best fit, it is important to have at least a few angles between 0° and 90°. An example of this type of analysis for as-cast and annealed (120 °C) DTI films is shown in Figure A.9. It is clear that the annealed DTI film has an overall much more edge-on orientation with its orientation order parameter of $S = -0.33$ compared to $S = -0.0038$ for the as-cast film.

The fluorescence yield (FY) detection mode of NEXAFS analyzes fluorescence photons that are emitted as a result of an absorption process, and relative to PEY, it is more bulk sensitive, probing about 100 nm into the film [74]. FY data was collected for pristine DTI and P3HT:DTI films. Similar to the PEY data, orientation analysis reveals that generally, the molecules become more edge-on with thermal annealing, as shown in Figure A.10. The FY spectra show a much greater intensity of the π^* transitions relative to the higher energy σ^* transitions as compared to the PEY spectra. This is likely to occur because the alkyl chains of both DTI and P3HT populate the surface of the film

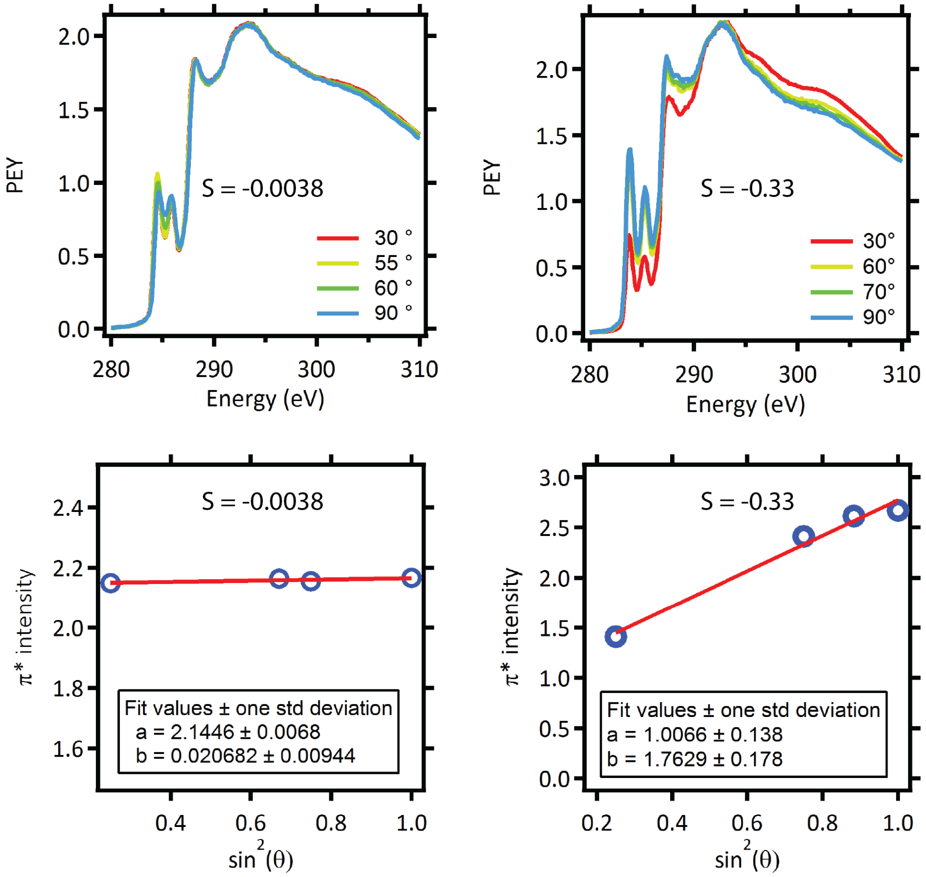

Figure A.9: PEY carbon K edge spectra taken at different incident angles for a) an as-cast DTI film and c) an annealed DTI film. The area under the π^* peaks is plotted vs. $sin^2(\theta)$ and fit to a line for b) the as-cast film and d) the annealed film.

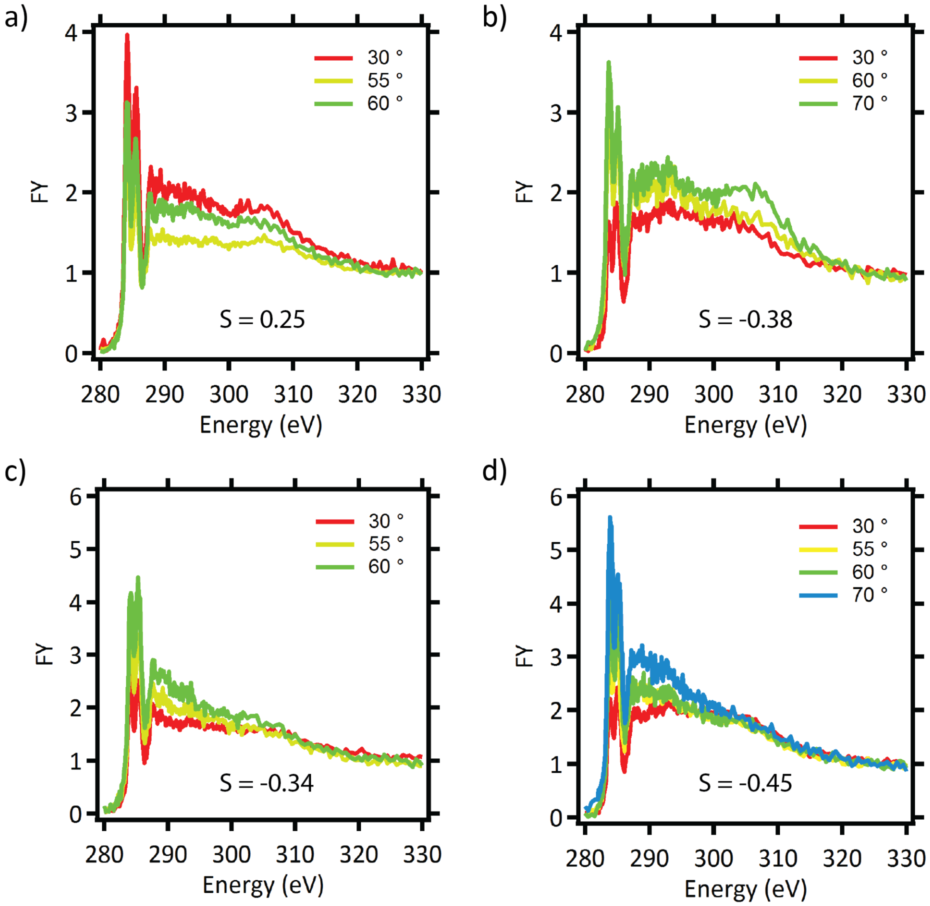

Figure A.10: FY carbon K edge spectra taken at different incident angles for a) an as-cast DTI film, b) an annealed DTI film, c) an as-cast P3HT:DTI blend, and d) an annealed P3HT:DTI blend. The values of the orientation order parameter are indicated.

to minimize surface energy. Since Auger emission is enhanced over fluorescent photon emission for carbon by over two orders of magnitude, the signal-to-noise ratio of the FY data is much less than the PEY data [186]. Overall, the values of S are more negative for the annealed and blend films based on FY compared to PEY. It is possible that the molecules have more edge-on character in the bulk compared to the surface. However, the noisier FY data means that the linear fits of I_{π^*} vs. $sin^2(\theta)$ were not as good.

A.6.4 Contribution from DTI to Overall Orientation of Blend Films

The orientation order parameter for as-cast and annealed blend films indicated a greater degree of edge-on character in the annealed blend. However, the π^* peak in the PEY data of the blends is a composite of the π^* peaks from DTI and P3HT. It is difficult to separate the contributions from P3HT and DTI since they overlap significantly. To get a sense of the relative contribution from DTI to the overall blend orientation in as-cast and annealed films, the composition, or % DTI, of the π^* peak in the blends was determined based on a linear combination of π^* peaks of the pure DTI and P3HT components. Highly edge-on molecules exhibit a large difference in total π^* intensity between incident angles of 30° and 90°, as seen in Figure A.9 for annealed DTI. Therefore, if DTI is much more edge-on relative to P3HT in the annealed film compared to the as-cast film, then the increase in % DTI of the composite π^* peaks from 30° to 90° should be greater in the annealed film. Figure A.11 shows the % DTI for different incident angles of the as-cast and annealed blends. It is clear that the annealed blend has an overall greater fraction of DTI and the increase in % DTI from 30° to 90° (35% to 55%) is greater than the as-cast blend (28% to 40%). This supports the claim that the thermally induced reorientation in the blends is mostly a result of changes in DTI.

A.7 Electron-Only and Hole-Only Diodes

Thermal annealing leads to a significant decrease in the electron current as expected based on the reorientation of the DTI molecules. However, since P3HT does not undergo the same type of reorientation, and possibly becomes more crystalline with annealing, the hole current is not expected to decrease significantly with annealing since holes travel

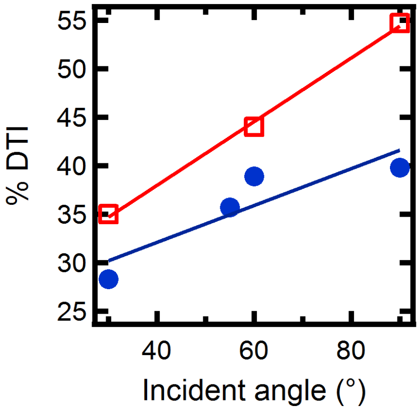

Figure A.11: % DTI as a function of incident angle for as-cast (blue circles) and annealed (red open squares) P3HT:DTI blend films. The % DTI was determined based on a linear combination of the π^* peaks of the pure P3HT and DTI components. The lines represent linear fits to the data.

predominantly through P3HT domains. Figure A.12 shows the dark J-V behavior of as-cast and annealed electron-only and hole-only diodes. It is clear that annealing leads to a significant drop in the electron current, but not in the hole current. The experimental data was fit with a Mott-Gurney relation, $J = \frac{9}{8}\mu\epsilon_0\epsilon_r\frac{V^2}{L^3}$, where μ is the mobility, ϵ_0 is the permittivity of free space, ϵ_r is the dielectric constant of the material, assumed to be 3.8, and L is the film thickness which was set to 100 nm. Using this relation, the electron and hole mobilities can be estimated. For the electron-only diode, the electron mobility decreased from $\mu_e = 4.1 \times 10^{-6}\frac{cm^2}{V \cdot s}$ to $\mu_e = 1.8 \times 10^{-7}\frac{cm^2}{V \cdot s}$ for the as-cast and annealed devices, respectively. Alternatively, the mobility in the hole-only devices did not change significantly, with a mobility of $\mu_h = 3.7 \times 10^{-5}\frac{cm^2}{V \cdot s}$ and $\mu_h = 6.9 \times 10^{-5}\frac{cm^2}{V \cdot s}$ for the as-cast and annealed devices, respectively.

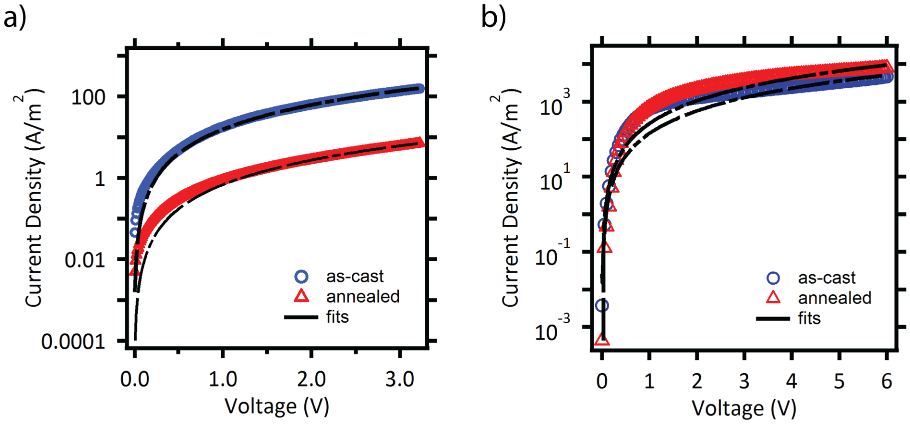

Figure A.12: J-V curves taken in the dark for (a) an electron-only and (b) a hole-only diode. Device geometry for the electron-only diode was glass/Al/P3HT:DTI/Ca/Al, and glass/ITO/PEDOT:PSS/P3HT:DTI/Au for the hole-only diode. Data was fit with a Mott-Gurney relation.

A.8 Additional GIWAXS Studies

A.8.1 Hexagonal Packing

The GIWAXS pattern of annealed DTI films shows a pattern indicative of hexagonal packing. The reciprocal space pattern of a hexagon is another hexagon that is rotated by 30°. Therefore, a hexagonal structure oriented with one of its flat sides parallel to the substrate would have a scattering pattern that includes a reflection nearly out-of-plane (close to the q_z axis), and another reflection at an angle 60° from the vertical axis. To visualize this, the 2D GIWAXS patterns can be plotted as q vs. polar angle. This is shown in Figure A.13. It is clear that the spots of high intensity for the reflection at 0.29 Å^{-1} are at polar angles near 0° and 60°, as expected for hexagonal packing.

A.8.2 *In Situ* Experiments

In situ GIWAXS experiments were done to examine the temperatures and time scales required for DTI reorientation. *In situ* experiments where the sample was incrementally

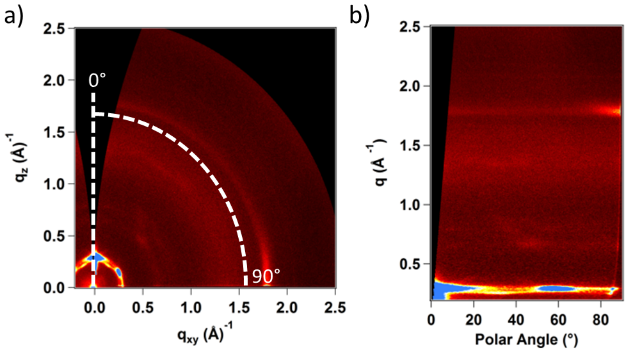

Figure A.13: (a) A typical 2D GIWAXS pattern of an annealed pristine DTI film showing intensity as a function of the in-plane and out-of-plane components of the scattering wave vector. (b) This can be transformed to show q as a function of polar angle (°).

heated, allowed to equilibrate, and then a scattering pattern taken were performed on the P3HT:DTI blend (Figure A.14). Additionally, an isothermal experiment was performed where the sample was heated to 120 °C and GIWAXS data taken over time. This is shown for a P3HT:DTI blend in Figure A.15. Note that it does take several minutes for the sample to reach 120 °C when heated from room temperature. It is clear that in the time it takes the hot plate to reach 120 °C, the characteristic hexagonal pattern and in-plane π-π stacking of annealed DTI is already apparent, and this pattern becomes more well defined with time.

Similar *in situ* GIWAXS studies, both at temperature during incremental heating and as a function of time at 120 °C, were done for pristine DTI films. *In situ* scattering at incremental temperatures reveals that, similar to the blend, the typical hexagonal pattern begins to form in the reflection at 0.29 Å^{-1} even at 40 °C, as shown in Figure A.16. This is close to the temperature where the exothermic peak on heating is observed in the DSC, suggesting again that this is a cold crystallization peak. Further heating leads to the pattern becoming more well-defined and the intensity of the π-π stacking peak becomes more concentrated in-plane. When pristine DTI is heated to 120 °C and

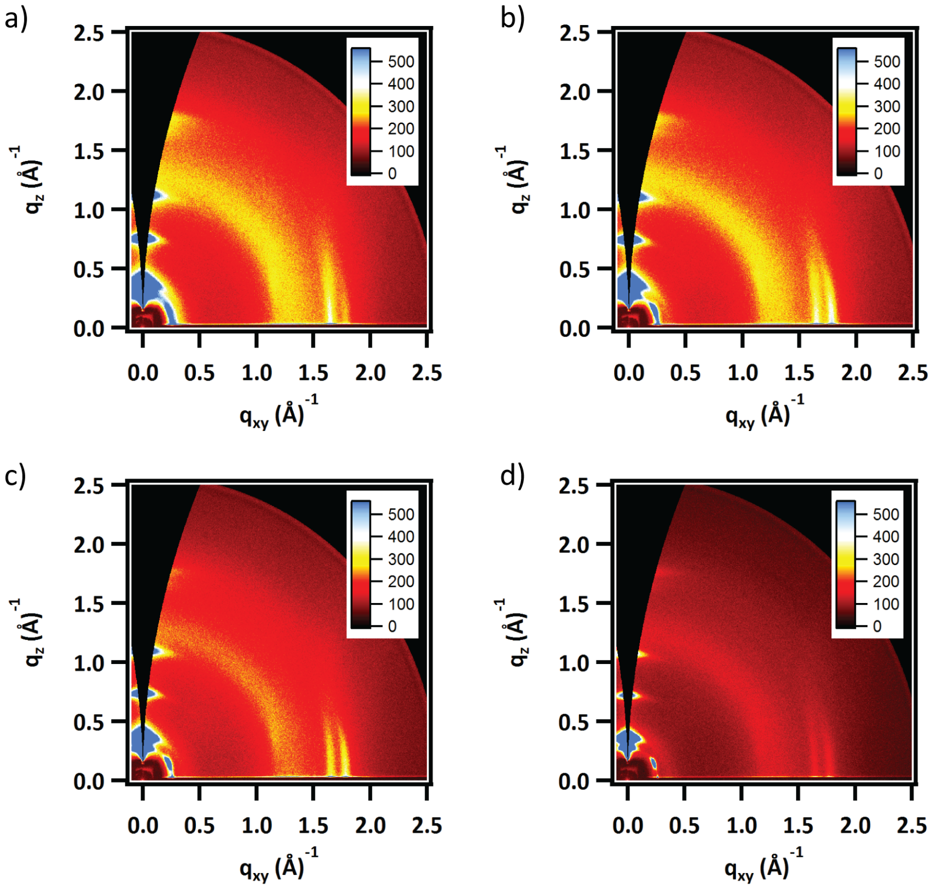

Figure A.14: *In situ* GIWAXS patterns of a P3HT:DTI blend film taken during heating at a) 60 °C, b) 70 °C, c) 80 °C, and d) 120 °C.

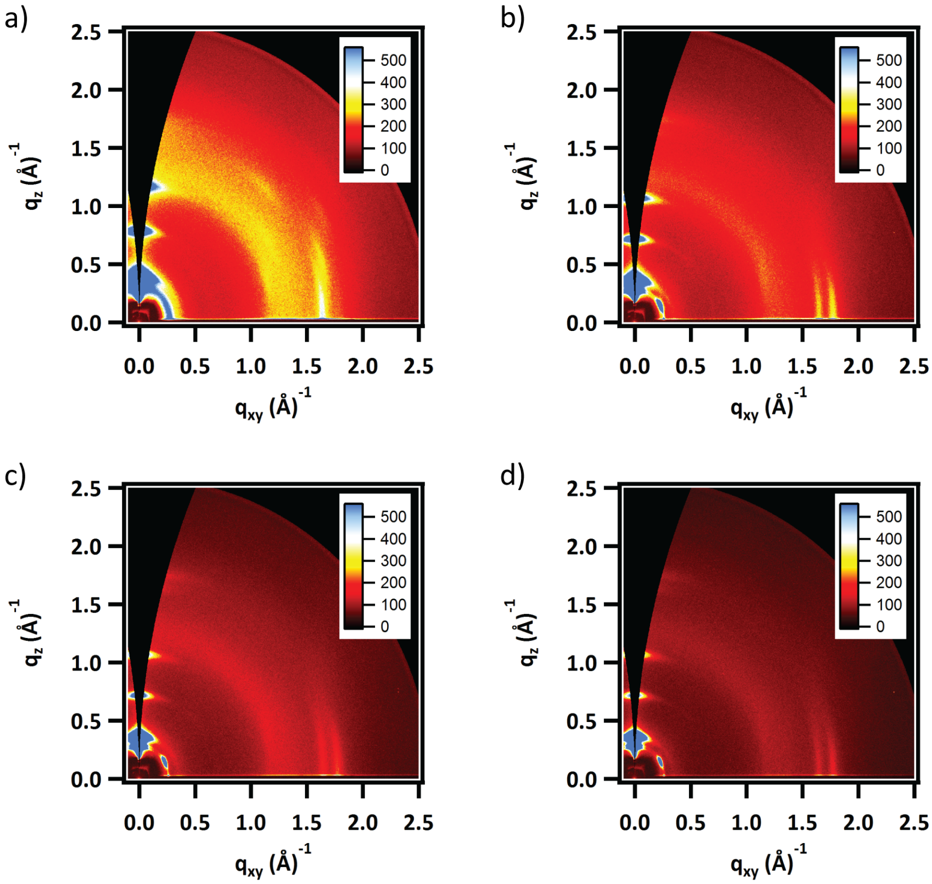

Figure A.15: *In situ* GIWAXS patterns of a P3HT:DTI blend film at a) room temperature, b) once the sample reached 120 °C, c) 6 minutes after reaching 120 °C, and d) 20 minutes after reaching 120 °C.

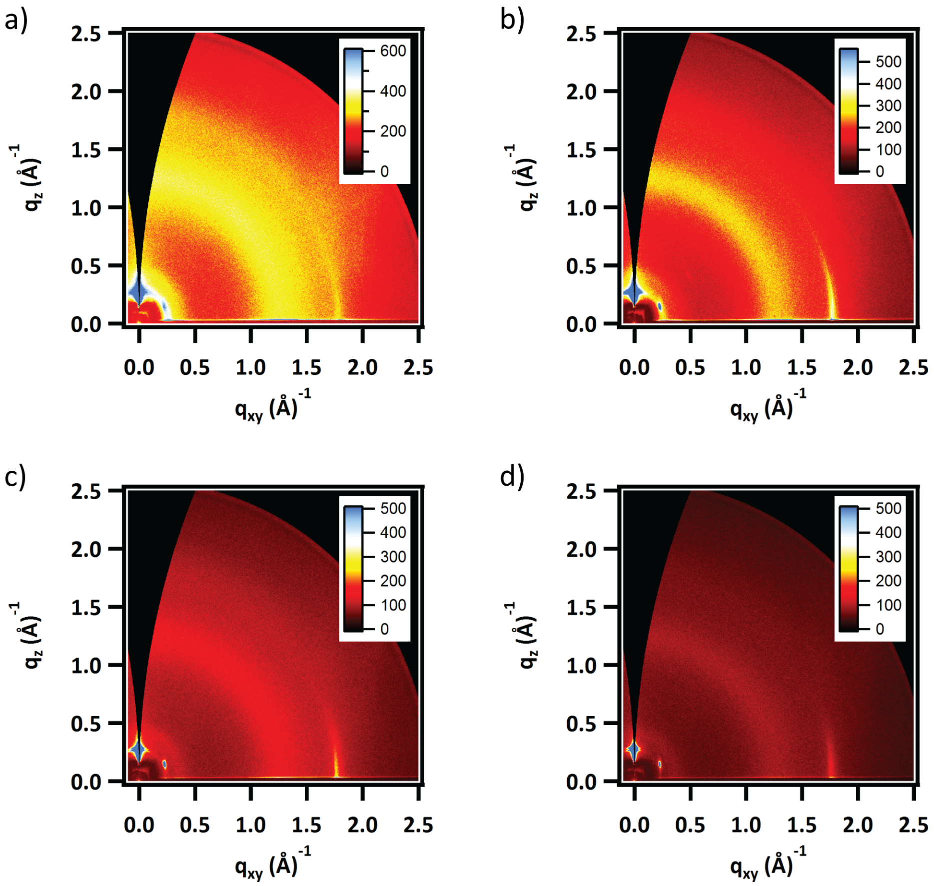

Figure A.16: *In situ* GIWAXS patterns of a pristine DTI film taken during heating at a) 40 °C, b) 60 °C, c) 80 °C, and d) 120 °C.

examined as a function of time (Figure A.17), it is again observed that by the time the sample temperature reaches 120 °C, the hexagonal reflection at 0.29 Å^{-1} and in-plane π-π stacking is already observed. Again, this pattern becomes more defined with time. *In situ* data on the pristine DTI film is similar to the P3HT:DTI blend, however, it seems that the characteristic annealed scattering pattern evolves at lower temperatures and shorter annealing times. This is suggestive that blending P3HT and DTI somewhat inhibits the kinetics of reorientation and ordering of DTI.

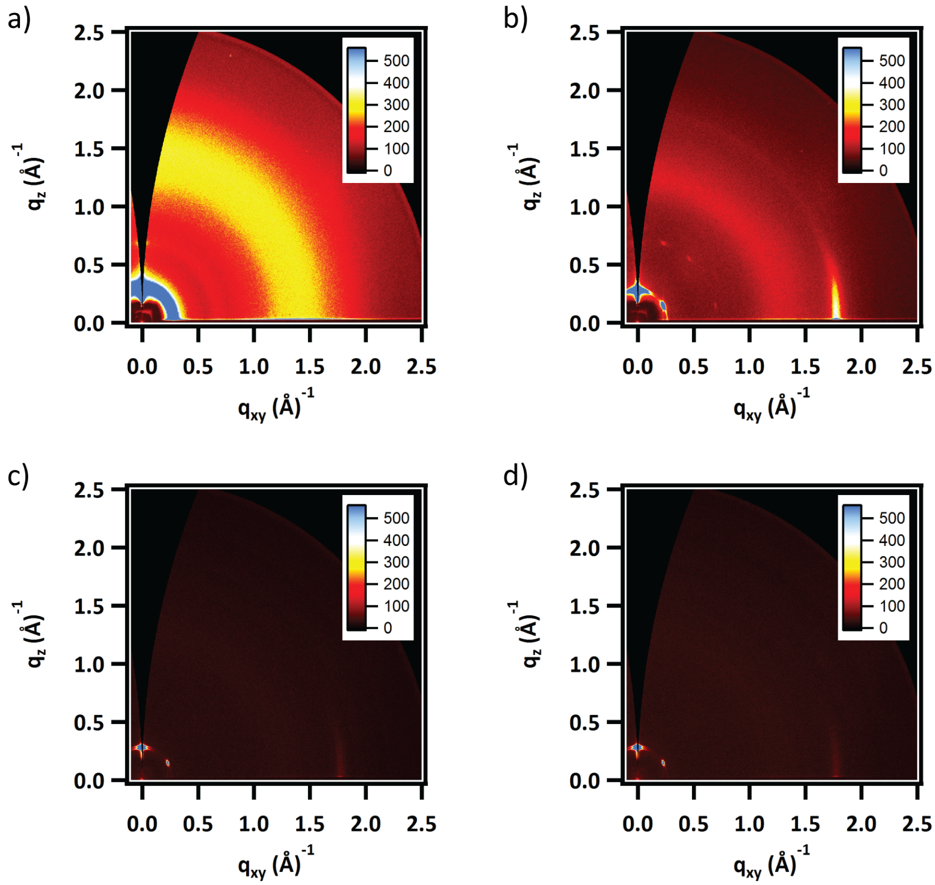

Figure A.17: *In situ* GIWAXS patterns of a pristine DTI film at a) room temperature, b) once the sample reached 120 °C, c) 10.5 minutes after reaching 120 °C, and d) 20 minutes after reaching 120 °C.

A.8.3 Correlation Lengths

X-ray scattering experiments also provide a way to probe changes and development in crystallite correlation lengths that result from annealing. The width of diffraction peaks can provide information on correlation lengths within the sample and potentially grain or crystallite sizes. The simplest way to extract information on the coherence length, L_c is through the Scherrer equation [86, 27],

$$L_c = \frac{2\pi K}{\Delta_q},$$

where K is the shape factor (typically 0.8 - 1) and Δ_q is the full width at half-maximum (FWHM) of a diffraction peak. However, care must be taken when using the Scherrer formula as it assumes that only crystalline size contributes to peak width, and ignores disorder. The results of Scherrer analysis should be considered more as correlation lengths between regions of disorder as opposed to true crystallite sizes. Nevertheless, this still provides a useful way to track changes in correlation lengths.

Peak width analysis was performed on as-cast and annealed (120 °C for 20 min) P3HT:DTI blends to estimate changes in correlation lengths and crystallite size. Scattering peaks were fit with either a Gaussian or Lorentzian line-shape in order to determine the peak position and FWHM. Fits were performed for scattering in the nearly out-of-plane direction (along q_z) for the alkyl stacking extent of DTI (centered at ~ 0.29 Å^{-1}) and the (100) reflection of P3HT (centered at ~ 0.38 Å^{-1}). This provides information on the vertical height of stacked DTI aggregates and P3HT crystallites. Additionally, the extent of in-plane π-π stacking was determined by fits along the in-plane portion (along q$_{xy}$) of the π-π stacking reflections. Representative fits are shown in Figure A.18a and A.18b. Changes in correlation lengths in the out-of-plane extent are shown in Figure A.18c, and the in-plane π-π extent in Figure A.18d.

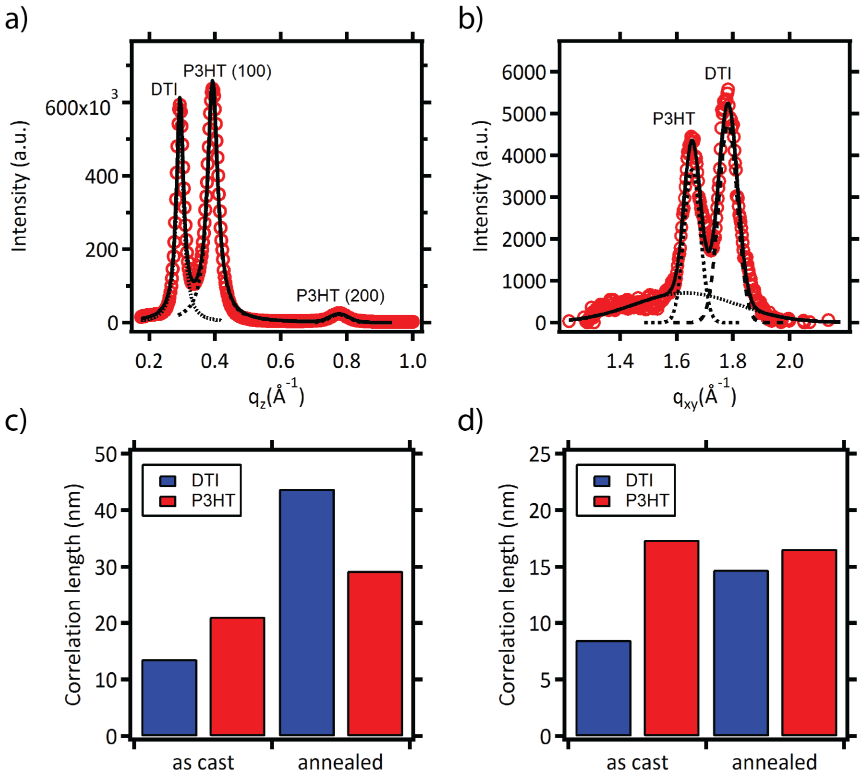

Figure A.18: Representative example of peak fitting for (a) the nearly out-of-plane scattering and (b) in-plane scattering near the π-π stacking distance for an annealed P3HT:DTI blend. Correlation lengths in the nearly out-of-plane direction determined from Scherrer analysis are shown in (c) for the hexagonal reflection of DTI and the (100) reflection of P3HT. (d) shows the in-plane π-π stacking correlation lengths for DTI and P3HT.

The most significant change in correlation length is for the out-of-plane alkyl stacking extent of DTI with thermal annealing. This suggests that annealing leads to aggregates of separate DTI columns that in total may be quite high, nearly 50 nm. On the contrary, the length of these DTI columns does not seem to change much based on the width of the π-π stacking peak, as it only varies from $\sim$8 nm to $\sim$15 nm for as-cast and annealed blends, respectively. It is possible that charge transport through separate stacks of DTI molecules can occur even if their π-π stacking directions are not perfectly parallel. Charges may still find pathways for transport in an as-cast film that consists of stacks of DTI with no preferential orientation. Peak width data suggests that annealing does not lead to a large increase in the lengths of DTI columns, so the reduced performance of annealed devices is likely mostly due to reorientation and stacking of separate DTI columns.

A.8.4 Crystallite Orientation

Crystallite orientation can be determined from 2D GIWAXS patterns based on the intensity distribution over polar angle (°) of a given reflection. Crystallites with no preferred orientation will appear as a ring of scattering in 2D scattering patterns. Figure A.19 shows the intensity distribution as a function of polar angle for the (100) reflection of P3HT and the alkyl stacking reflection for DTI located at $\sim$0.29 Å^{-1} as a function of temperature during annealing. It is clear that the intensity distribution of P3HT remains relatively constant with annealing, indicating there is little reorientation of P3HT crystallites. The characteristic hexagonal pattern of annealed DTI shows up very clearly by 70 °C.

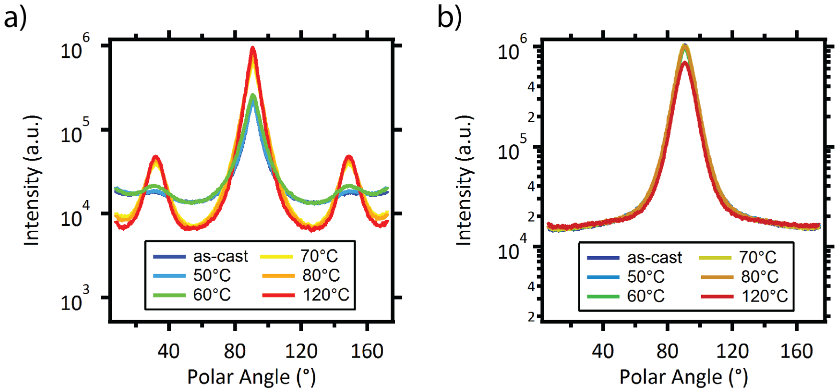

Figure A.19: Intensity distribution as a function of polar angle (°) for (a) the alkyl stacking reflection of DTI and (b) the (100) reflection for P3HT taken at various temperatures during annealing.

A.9 Thermal Transitions Probed by DSC

Additional DSC data on pristine DTI and pristine P3HT is shown in Figure A.20a. Also, a closer look at the crystallization peak of P3HT during cooling (around 200 °C) reveals that when mixed with DTI, P3HT crystallizes at a lower temperature, as seen in Figure A.20b. This suggests that DTI may also slightly inhibit the crystallization of P3HT.

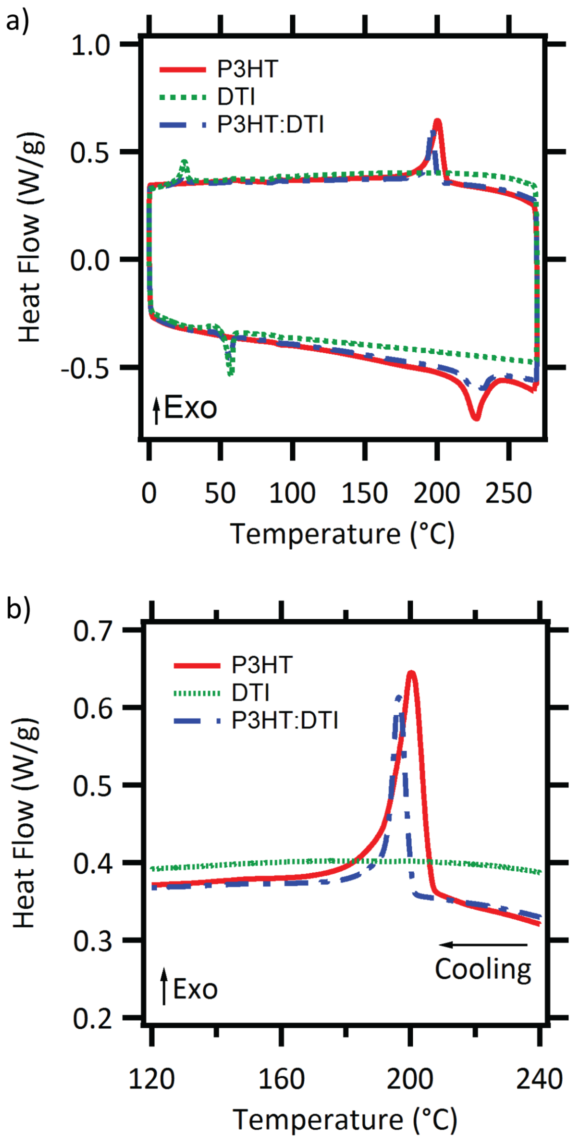

Figure A.20: (a) DSC scans of pristine P3HT (red curve), pristine DTI (green dashed curve), and a 1:1 by mass P3HT:DTI blend (blue dotted-dashed curve). A zoom in of the crystallization peak of P3HT is shown in (b). The heating and cooling rate was 10 °C/min.

Appendix B

Supporting Information Chapter 3

B.1 Experimental Methods

Poly[3-(ethyl-5-pentanoate)thiophene-2,5-diyl] (P3EPT) and poly(3-hexylthiophene) were purchased from Rieke Metals, Inc (Lincoln, NE). PVDF-TrFE (70:30) was purchased from Piezotech LLC. P3EPT, PVDF-TrFE, and P3EPT:PVDF-TrFE blend solutions were made by dissolving in 2-methyl-tetrahydrofuran at a concentration of 20 mg/mL. Thin films were fabricated by spin coating solutions at 2000 rpm for 60 s. Thermally annealed samples were heated at 135 °C for 3 hours and slowly cooled to room temperature.

Samples for GIWAXS were prepared by spin-coating solutions onto Si substrates or glass/ITO substrates using the deposition conditions stated above. GIWAXS experiments were performed at the Stanford Synchrotron Radiation Lightsource (SSRL) at beamline 11-3. A MAR 2300 area detector was used for 2D diffraction pattern collection. The energy of the incident beam is 12.7 keV. The angle of incidence used was 0.10-0.12° and the sample-to-detector distance was 40 cm. Exposure times were typically bewteen 120 s and 240 s. *In situ* GIWAXS experiments during thermal annealing were performed at beamline 7.3.3 at the Advanced Light Source (ALS). A Pilatus 2M silicon hybrid pixel detector was used for 2D data collection. The X-ray energy at beamline 7.3.3 is 10 keV, and sample-detector distance was 30 cm. An incident angle of 0.16° and a 5 s exposure time were used for the *in situ* studies. For all GIWAXS experiments, samples were placed in a helium atmosphere environment to minimize X-ray damage and background scattering.

RSoXS was performed at beamline 11.0.1.2 at the ALS. Samples were prepared by floating P3EPT:PVDF-TrFE thin films onto 1.5 mm x 1.5 mm, 100 nm thick Si_3N_4 membranes supported by a 5 mm x 5 mm Si frame (Norcada Inc.). 2D scattering was collected in a transmission geometry with a sample-to-detector distance of 160 mm. Data was collected on an in-vacuum CCD camera (Princeton Instrument PI-MTE) cooled to -45 °C. 2D scattering data was then reduced by azimuthal averaging of the scattering data over all q values. The RSoXS profiles shown were taken at 284.6 eV. Details of the specifics of this beamline have been reported elsewhere [23].

Samples for electron yield NEXAFS were prepared by spin-coating onto Si substrates. Partial electron yield NEXAFS experiments were performed at beamline U7A at the National Synchrotron Light Source (NSLS). The incident X-ray beam was elliptically polarized (polarization factor = 0.85) with the electric field vector predominantly in the plane of the storage ring. The incident angle, θ, was 55° near the magic angle. 90° refers to an incident X-ray beam that is perpendicular to the substrate. A spherical grating monochromator was used to select soft X-rays in the range from 280 eV to 340 eV, corresponding to the carbon K edge. The partial electron yield (PEY) data was collected with a channeltron electron multiplier with an adjustable entrance grid bias that was set to -150 V. All experiments were done in a UHV chamber. Carbon edge PEY data was normalized by subtracting a linear pre-edge baseline and setting the edge jump to unity at 320 eV. Transmission NEXAFS experiments were performed at beamline 11.0.1.2 at the ALS on thin films floated onto Si_3N_4 membranes.

Scanning transmission X-ray microscopy was carried out at beamline 5.3.2.2 at the Advanced Light Source. Samples were prepared by floating P3EPT, PVDF-TrFE or P3EPT:PVDF-TrFE films onto Cu TEM grids. Samples were mounted in a sample chamber that was evacuated to low pressure and refilled to about 0.3 atm of helium. The transmitted intensity was monitored using a scintillator and a photomultiplier tube. Specifics of the beamline are reported elsewhere [187, 188, 24].

AFM experiments were performed in tapping mode on an Asylum Research MFP 3D AFM using NanoWorld Pointprobe Al-coated noncontact mode Si cantilevers with a spring constant of 48 N/m and a resonant frequency of 190 kHz.

DSC measurements were carried out on a TA Instruments DSC 2920 differential scanning calorimeter. About 5 mg of material was loaded into Tzero aluminum pans. A blank Tzero pan was used as a reference. Samples were heated and cooled from 0 °C to 250 °C with a heating a cooling rate of 10 °C/min. Only one of the heating and cooling cycles is shown in the figures.

Resistive switching devices were fabricated in a nitrogen atmosphere with the following geometry: glass/ITO/P3EPT:PVDF-TrFE/Ca/Al. The polymer blend layer was deposited on the glass/ITO substrates via spin coating using the same conditions stated above. The Ca/Al top contact was thermally evaporated with thicknesses of 10 nm (Ca) and 90 nm (Al). Samples were thermally annealed at 135 °C for 3 hours. Devices were studied under vacuum in a probe station at $\sim 10^{-5}$ Torr. Current-voltage testing was performed by grounding the top contact and applying a bias to the bottom ITO contact. Poling was carried out by applying +/-20 V to the ITO contact for 2 s, where positive poling refers to a device state after +20 V were applied, and vice versa for negative poling. Devices characteristics were determined by collecting current-voltage data at a typical rate of 130 mV/s. For cyclic testing, poling at +/-20 V was applied for 10 s,

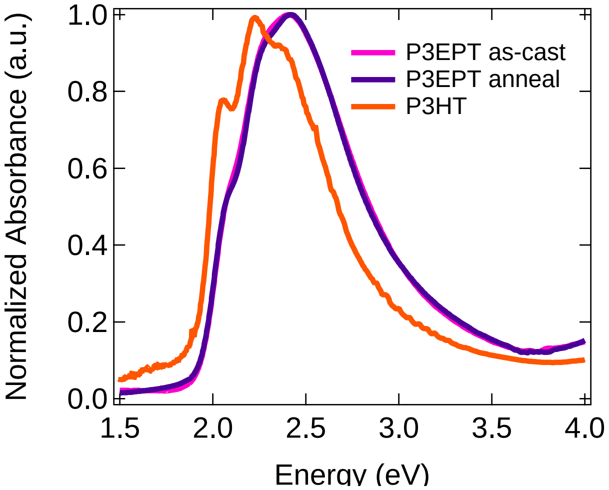

Figure B.1: UV-vis spectroscopy of thin films of (a) as-cast P3EPT, (b) P3EPT annealed at 135 °C, and (c) P3HT on glass/ITO substrates.

followed by reading at +3 V for 10 s.

B.2 UV-Vis Spectroscopy

B.3 P3EPT Mobility

B.4 Atomic Force Microscopy

AFM height images show a similar phase separated structure as seen in the phase images. Height images reveal that some of the circular P3EPT regions seem to be convex (protrude from film surface), while others are concave. These protrusions and depressions are relatively small in the 10% P3EPT blends (∼5 nm), but increase to about 15 nm and 25 nm for the 20% and 35% P3EPT blends, respectively. The total film thickness is about 200 nm for these blends.

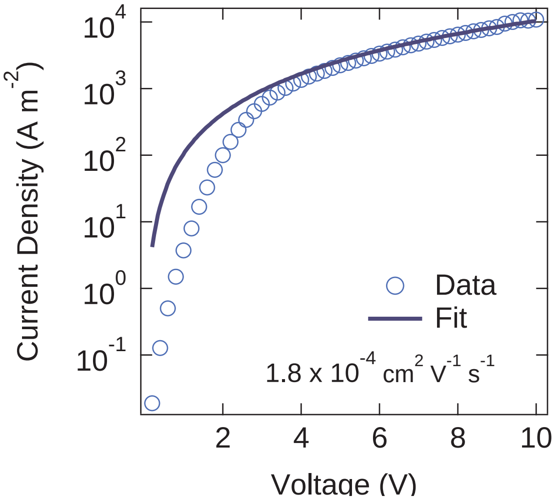

Figure B.2: Current-voltage data for a P3EPT diode and corresponding fit to a Mott-Gurney relation, $J = \frac{9}{8}\mu\epsilon_0\varepsilon\frac{V^2}{L^3}$, where ϵ_0 is the permittivity of free space, ε is the dielectric constant of the material, assumed to be 4, and L is the film thickness, 190 nm. The mobility, μ, is estimated to be $1.8 \times 10^{-4}\dfrac{cm^2}{Vs}$. The geometry of these diodes was glass/ITO/P3EPT/Ca/Al.

B.5 Grazing Incidence Wide Angle X-ray Scattering

Crystallite orientation can be probed by examining the intensity distribution as a function of polar angle for a given scattering peak. Using the (200) peak from pristine P3EPT, it is clear that there is enhanced intensity in the nearly out-of-plane direction (along q_z) and the in-plane direction (along q_{xy}) suggesting a bimodal distribution of edge-on and face-on P3EPT crystallites. The intensity vs. polar angle plot does not exclude the scattering in the wedge near q_z, which is shown in the 2D image.

B.6 Differential Scanning Calorimetry

DSC data of pure P3EPT (Figure B.5a) reveals an endothermic melting type transition upon heating at around 188 °C and an exothermic transition during cooling at about 149 °C. PVDF-TrFE (Figure B.5b) shows a melting transition at 151 °C, and

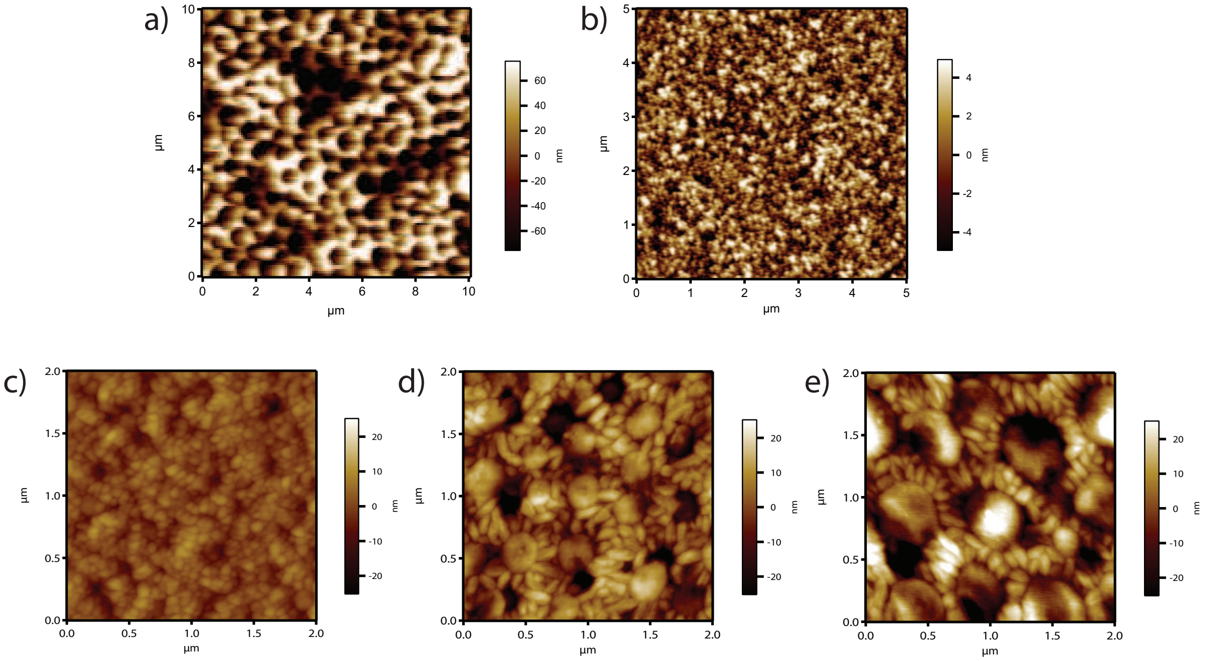

Figure B.3: 10 μm × 10 μm AFM height images of (a) 10:90 P3HT:PVDF-TrFE and (b) a 10:90 P3EPT:PVDF-TrFe blend. Zoomed in height images of (c) 10:90, (d) 20:80 and (e) 35:65 P3EPT:PVDF-TrFE blend ratios.

a main crystallization peak at 131 °C. Furthermore, the phase transitions between the ferroelectric and paraelectric phases of PVDF-TrFE occur at around 99 °C and 60 °C during heating and cooling, respectively. A 50:50 blend of P3EPT:PVDF-TrFE shows thermal transitions from both components.

B.7 Additional Data for Resistive Switches

B.8 Determining Mass Absorption for Composition Analysis via STXM

The procedure for estimating composition (wt.%) from STXM images at two different energies of the same region of the film were done as previously reported[24, 125]. The

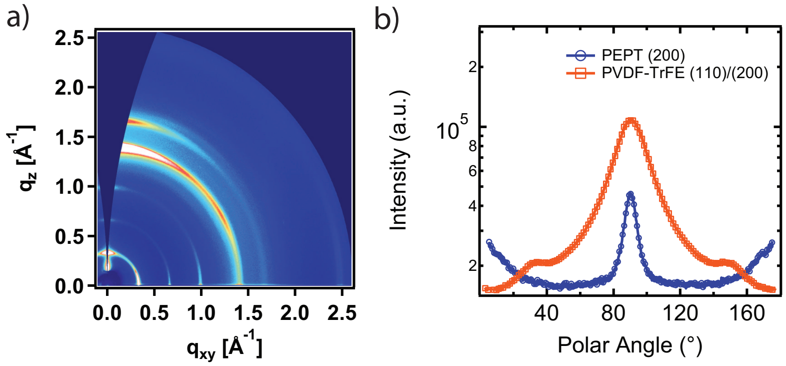

Figure B.4: (a) 2D GIWAXS pattern of a 35:65 P3EPT:PVDF-TrFE blend. (b) Intensity vs polar angle plots for a P3EPT (200) reflection and the main (110)/(200) reflection of PVDF-TrFE. These intensity distribution taken from the 2D GIWAXS patterns of the pure components.

NEXAFS spectra of the pure components need to be converted from optical density (OD), $OD = ln(I_0/I)$, to mass absorption, and this can be done by scaling the NEXAFS data to the "bare atom" mass absorption coefficient[24]. The bare atom spectrum is the mass average of the imaginary part of the measured atomic scattering factors, f_2, which are available for each element on the CXRO database. The mass absorption of the bare atom is given by

$$\mu(E) = 2r_e\lambda(E)N_A\frac{\sum_i x_i f_{2,i}(E)}{\sum_i x_i A_i}, \tag{B.1}$$

where r_e is the classical electron radius, λ the photon wavelength, N_A Avogadro's number, x_i is the number of atoms of type i, and A_i is the atomic weight. The sum in the denominator is chosen to be the molecular weight of the compound or the monomer molecular weight for a polymer. The NEXAFS data of the sample was scaled so that a post-edge value (340 eV) matched that of the mass absorption of the bare atom, as shown for P3EPT in Figure B.12. The STXM composition image was determined based on two images of the same region of the film, one at an energy where mass absorption of P3EPT and PVDF-TrFE are somewhat similar (280 eV), and another where the mass absorptions are very different (287.4 eV). This procedure is described in previous work[125].

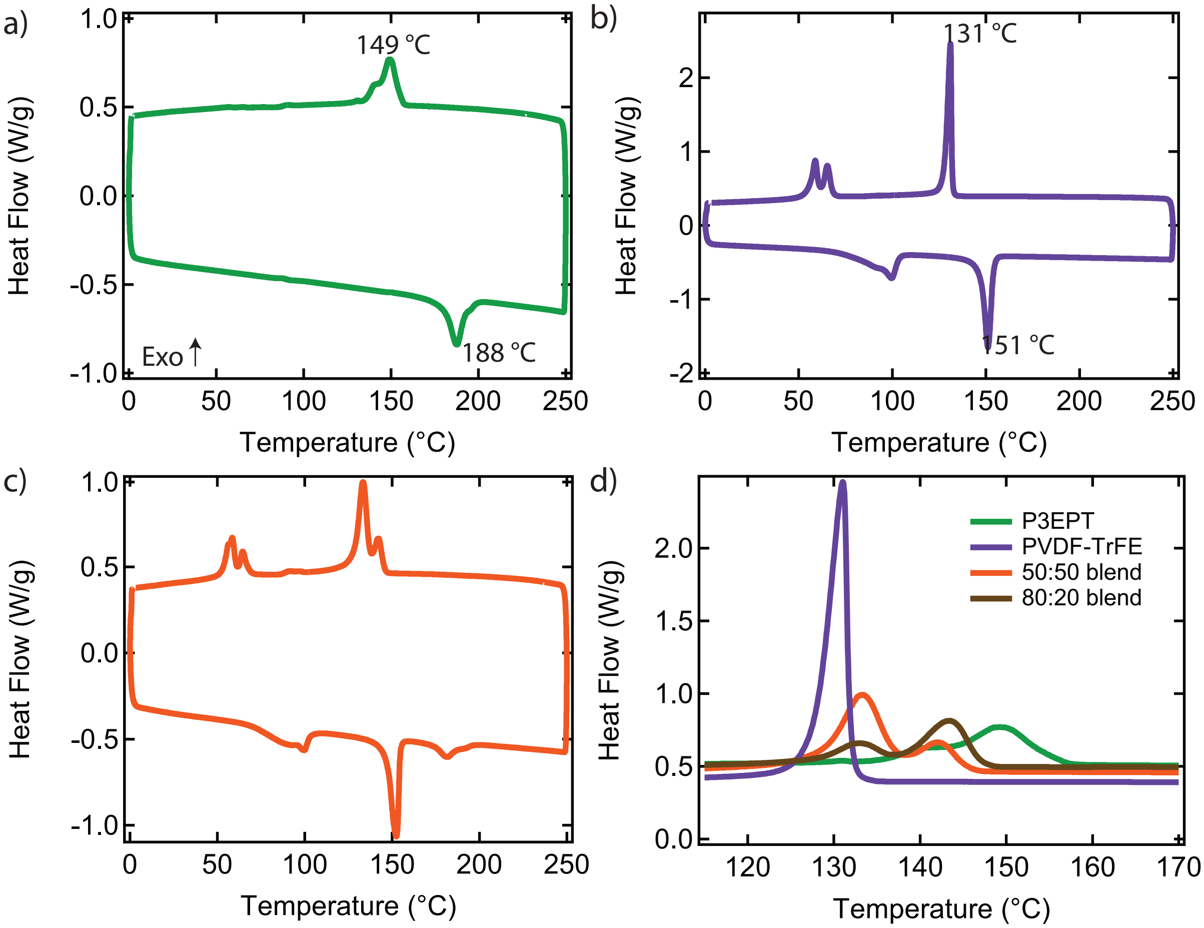

Figure B.5: Differential scanning calorimetry data for (a) pure P3EPT, (b) PVDF-TrFE and (c) and 50:50 P3EPT:PVDF-TrFE blend. A close up of the crystallization peaks plotted in (d) shows a shift in crystallization temperature for the blends relative to the pure components.

B.9 Transmission Soft X-ray Scattering

Radially averaged, Lorentz corrected ($I \times q^2$ vs. q) RSoXS profiles were fit to a combination of log-normal distribution functions to determine peak positions [189]. A representative example for the 10:90 P3EPT:PVDF-TrFE blend is shown in Figure B.14b. The raw I vs, q data is also shown in Figure B.14a.

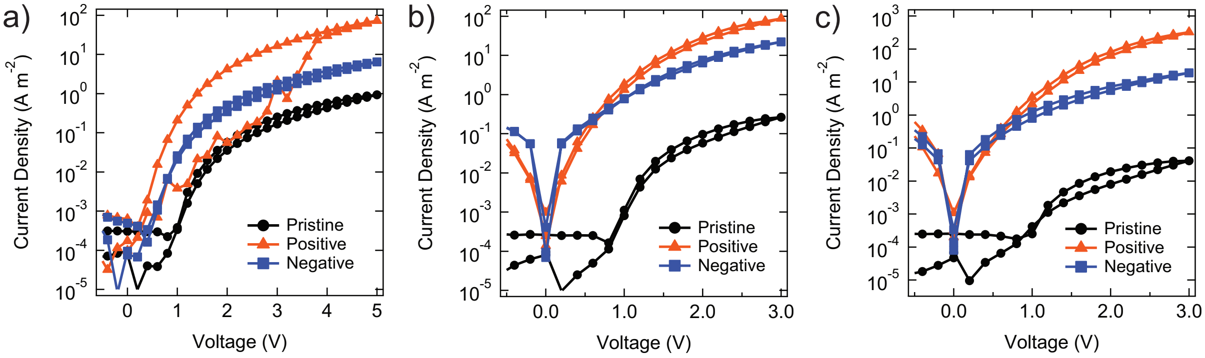

Figure B.6: P3EPT:PVDF-TrFE based resistive switches show ON and OFF poling characteristics over a variety of P3EPT ratios, including (a) 20%, (b) 35%, and (c) 50% P3EPT. Pristine refers to devices before any poling was applied.

B.10 Wide Angle X-ray Scattering

Penetration depth and intensity transmittivity were determined using well-known Fresnel equations[190, 191]. The densities, ρ, of P3EPT and PVDF-TrFE were assumed to be 1.15 g/cm^3 and 1.78 g/cm^3, respectively. The mass absorption was determined based on the tabulated values of f_2 from the CXRO database as discussed earlier and interpolated to 12.7 keV. The mass absorption of P3EPT was estimated to be 4.88 cm^2 g^{-1} and 2.6 cm^2 g^{-1} for PVDF-TrFE.

Reduced intensity vs. q plots shown in Figure B.16 were determined by integrating the intensity from the 2D scattering patterns for polar angles (χ) from 2° to 79°, where 0° corresponds to scattering along the q_{xy} direction and 90° corresponds to scattering along the q_z direction. It is known that in the grazing incidence geometry using a flat area detector, there is an inaccessible region of the Ewald sphere along q_z, so intensity along q_z cannot be considered as specular diffraction[84].

Intensity distribution as a function of χ (°) for a given reflection reveals information about crystallite orientation distribution. The Intensity vs. χ for the (200) peak of P3EPT in a P3EPT:PVDF-TrFe blend with 50 wt.% P3EPT is shown in Figure B.19. The (200) peak for 0.08°, 0.10°, and 0.12° incident angles have FWHM values of 31°,

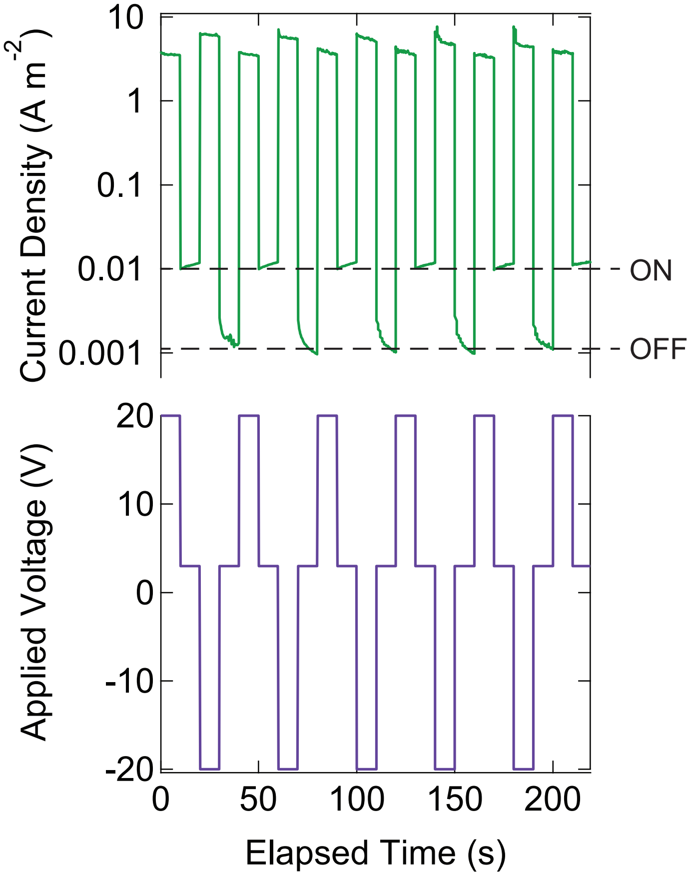

Figure B.7: Current density and corresponding applied voltage to the bottom ITO contact of a 10:90 P3EPT:PVDF-TrFE resistive switch. Devices were poled with a ±20 V pulse, and read at 3 V. The current densities of the ON and OFF states are indicated by the dotted lines.

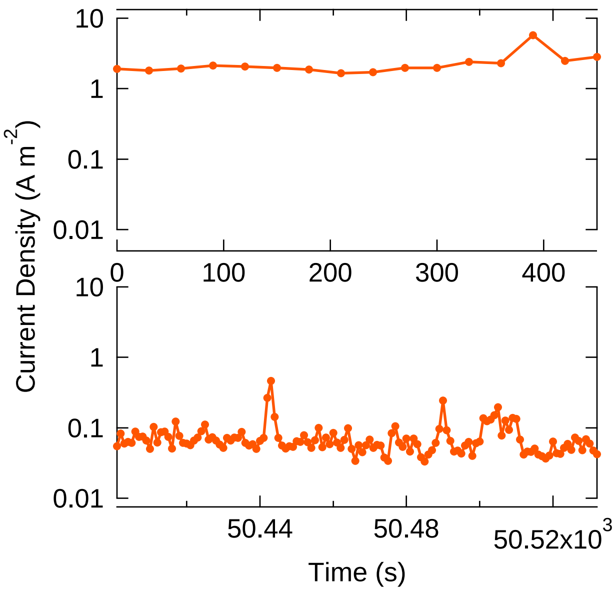

Figure B.8: Change in current density over time for a 10:90 P3EPT:PVDF-TrFE device initially positively poled (+20 V) into the ON state, then held at 0 V. The current density shown was determined by reading the device at 3 V at various times after the initial poling. The current density remains relatively constant (about 2 A/m^2) for the first several minutes following poling (top plot), and after 14 hours decreases to about 0.08 A/m^2 (bottom plot). Note that the initial reading labelled as 0 s was approximately 5 min after the device was poled.

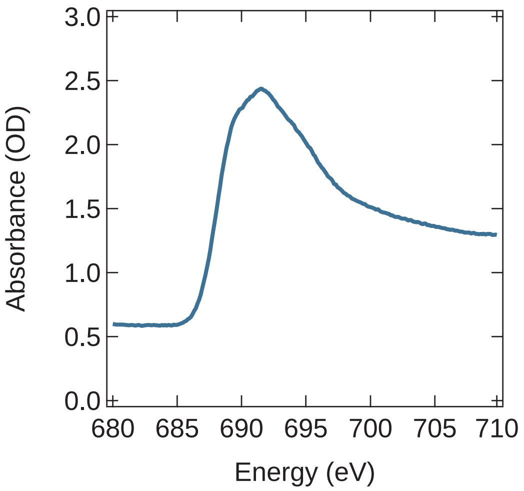

Figure B.9: Transmission NEXAFS spectra near the fluorine K edge for PVDF-TrFE. Absorbance is in optical density (OD). Absorption near these energies is selective to PVDF-TrFE since P3EPT does not contain any fluorine atoms.

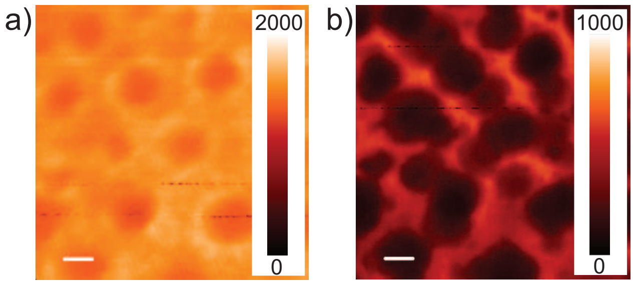

Figure B.10: STXM images of a P3EPT:PVDF-TrFE blend with 50 wt.% P3EPT taken at (a) a pre-edge energy (280 eV) where mass absorption is more similar between polymers, and (b) at 285.3 eV near the $\pi^*_{C=C}$ transition of P3EPT where absorption is dominated by P3EPT.

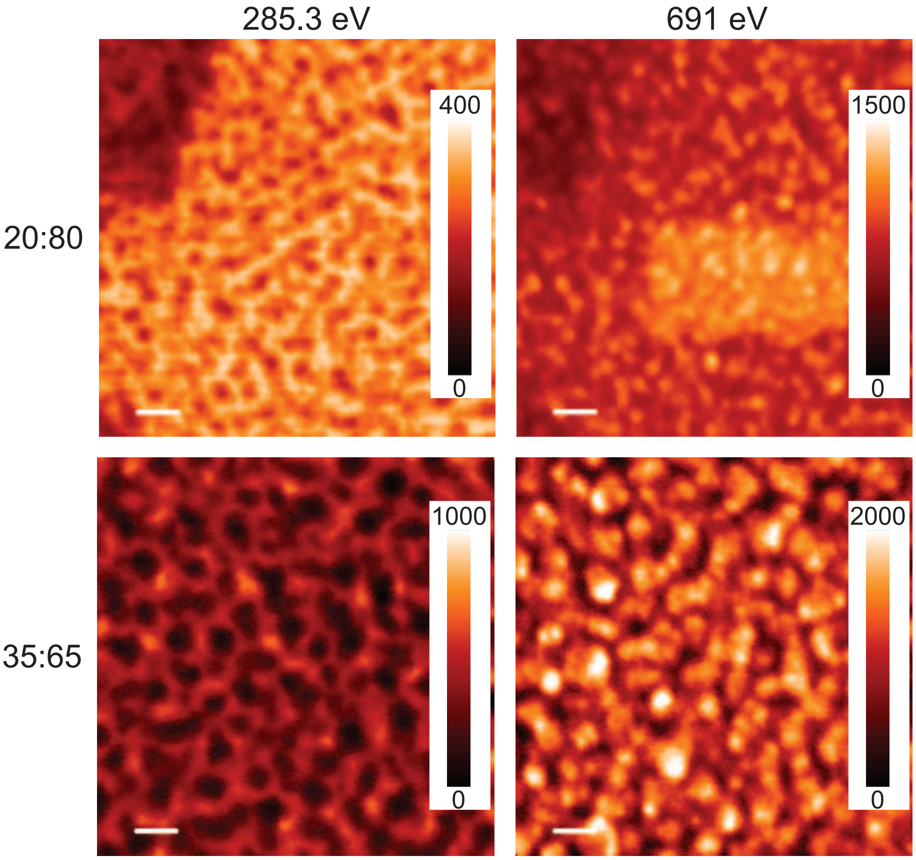

Figure B.11: STXM images of (top) a 20 wt.% P3EPT blend and (bottom) a 35 wt.% P3EPT blend. Scans at 285.3 eV (left column) are at an energy where P3EPT absorption dominates, and 691 eV (right column) is where PVDF-TrFE absorption dominates. A phase separated structures similar to the 50 wt.% P3EPT blend is evident.

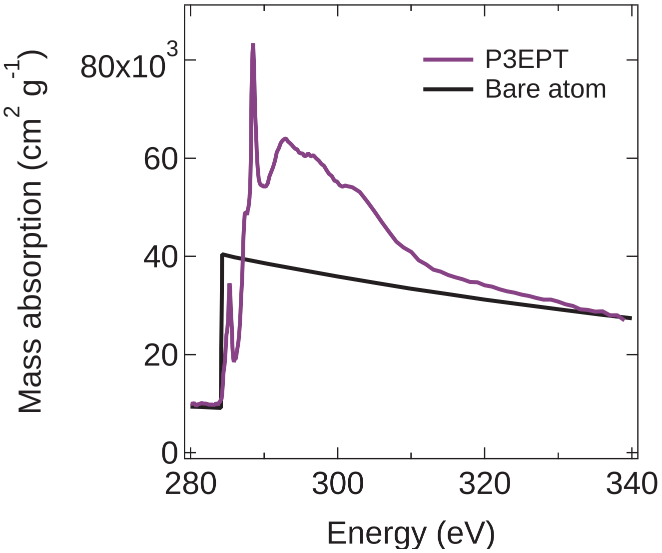

Figure B.12: The mass absorption of the materials was determined by scaling the NEXAFS spectra of each component at a post-edge value (340 eV) to match the mass absorption of the bare atom. Representative example for P3EPT is shown here.

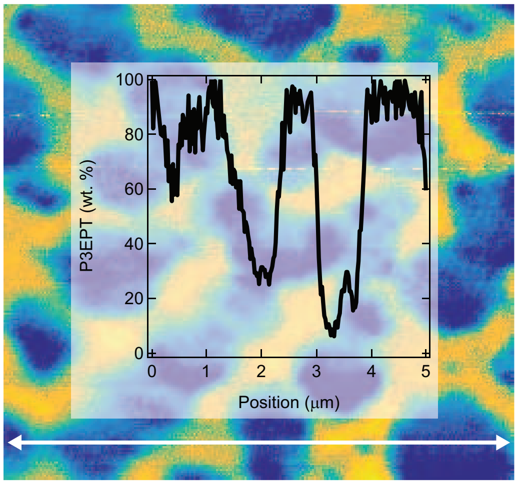

Figure B.13: Estimated P3EPT wt.% composition in a P3EPT:PVDF-TrFE blend with 50 wt.% P3EPT as a function of position along the white line indicated in the image. The image is 5x5 μm.

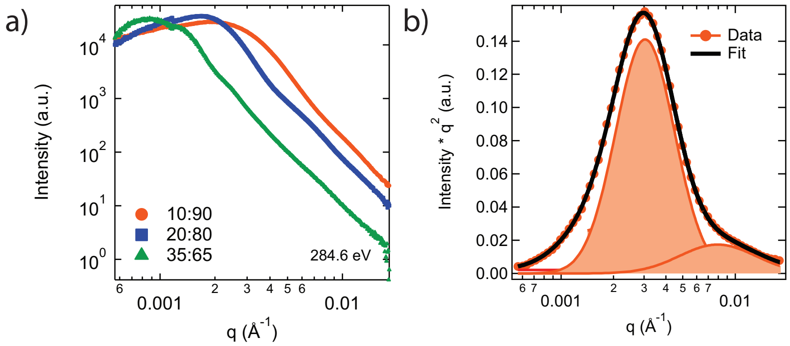

Figure B.14: (a) Intensity vs q scattering profiles P3EPT:PVDF-TrFE blends with 10 wt.%, 20 wt.% and 35 wt.% P3EPT taken at 284.6 eV. (b) Representative fit to Lorentz corrected data to determine peak positions.

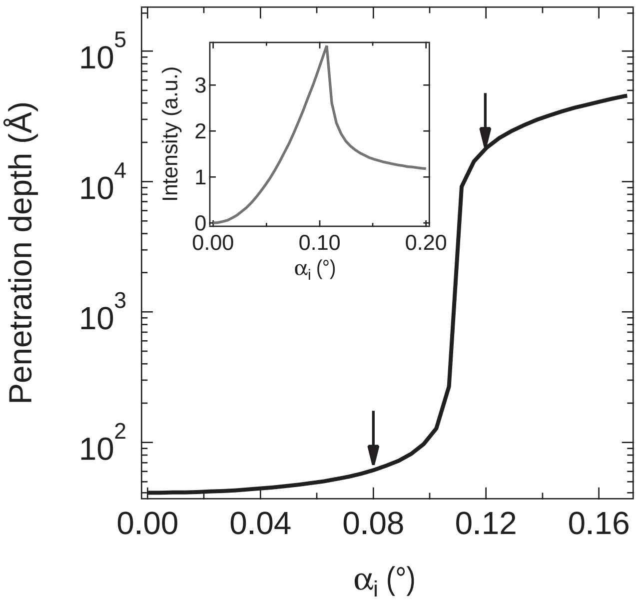

Figure B.15: Tuning the incident angle in GIWAXS experiments can be used to probe either the surface region of a thin film or more in the bulk. Estimated penetration depth as a function of incident angle for a P3EPT:PVDF-TrFE blend film is shown in (a), with the intensity transmittivity shown in the inset. The critical angle is 0.11°, similar to most polymers at this energy (12.7 keV).

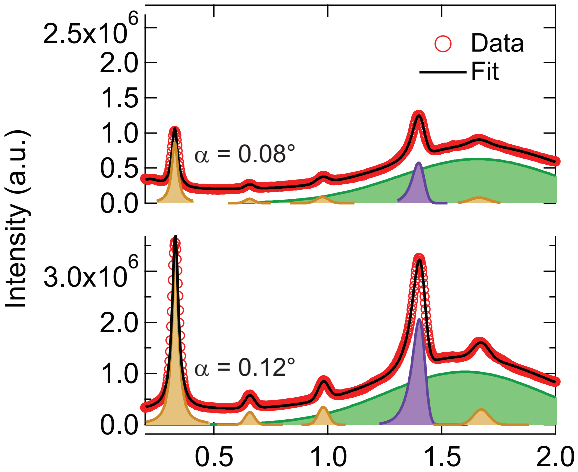

Figure B.16: Reduced intensity vs. q data for a P3EPT:PVDF-TrFE blend with 50 wt.% P3EPT at incident angles of 0.08° (top) and 0.12° (bottom). Peaks were fit using a Gaussian or Lorentzian lineshape. An exponentially modified Gaussian was used to fit the PVDF-TrFE peak as it is noticeably asymmetric in character. A constant background (not shown) was assumed. The peaks corresponding to reflections from P3EPT are shown in gold, PVDF-TrFE in purple, and amorphous scattering in green. The ratio of the area of the PVDF-TrFE peak to that of the P3EPT (100) peak is about 0.9 for both 0.08° and 0.12° incident angles.

32° and 30°, respectively. This suggests that the orientation distribution of crystallites close to the film surface (0.08°) is not significantly different than crystallite orientation through the bulk of the film (0.12°).

B.11 *In situ* Thermal Annealing and Wide Angle X-ray Scattering

GIWAXS patterns were collected at temperature for a 50 wt.% P3EPT blend film that was heated from room temperature to 200 °C then cooled back down. A heating and cooling rate of 10 °C/min was used. Clear changes in the crystalline nature of the film occurs at temperatures corresponding to thermal transitions in PVDF-TrFE and P3EPT. During heating, these transitions include a ferroparaelectric transition in the range of 80-

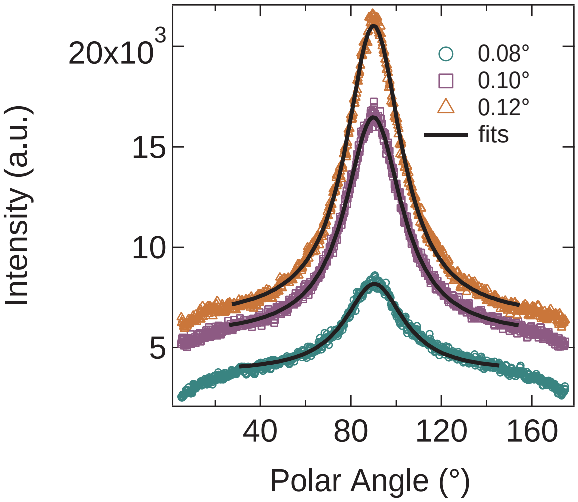

Figure B.17: Intensity vs. polar angle (°) of the P3EPT (200) peak for a P3EPT:PVDF-TrFE blend with 50 wt.% P3EPT at different incident angles shows orientation distribution for crystallites closer to the surface vs. in the bulk. Peaks were fit to Lorentzian line shapes.

100 °C, melting of PVDF-TrFE at around 152 °C, and melting of P3EPT near 180 °C. Recrystallization of P3EPT and PVDF-TrFE occur during cooling at around 142 °C and 133 °C, respectively, and another ferroparaelectric transition in the 70-50 °C range.

B.12 Water Contact Angle

Preliminary static water contact angle experiments were performed on annealed P3EPT, PVDF-TrFE, and P3EPT:PVDF-TrFE thin films. Droplet volumes used were 10 μL. Assuming the contact angle of a P3EPT:PVDF-TrFE blend film varies linearly between the values of the pure components, the fraction of P3EPT at the film surface was estimated based on the contact angle of the blends. The surface P3EPT content was estimated to be 71%, 75%, 79%, and 88% for the 10 wt.% (14.7 vol.%), 20 wt.% (27.9 vol.%), 35 wt.% (45.5 vol.%) and 50 wt.% (60.8 vol.%) P3EPT blend films, respectively. This is relatively similar to the surface composition values determined by PEY NEXAFS.

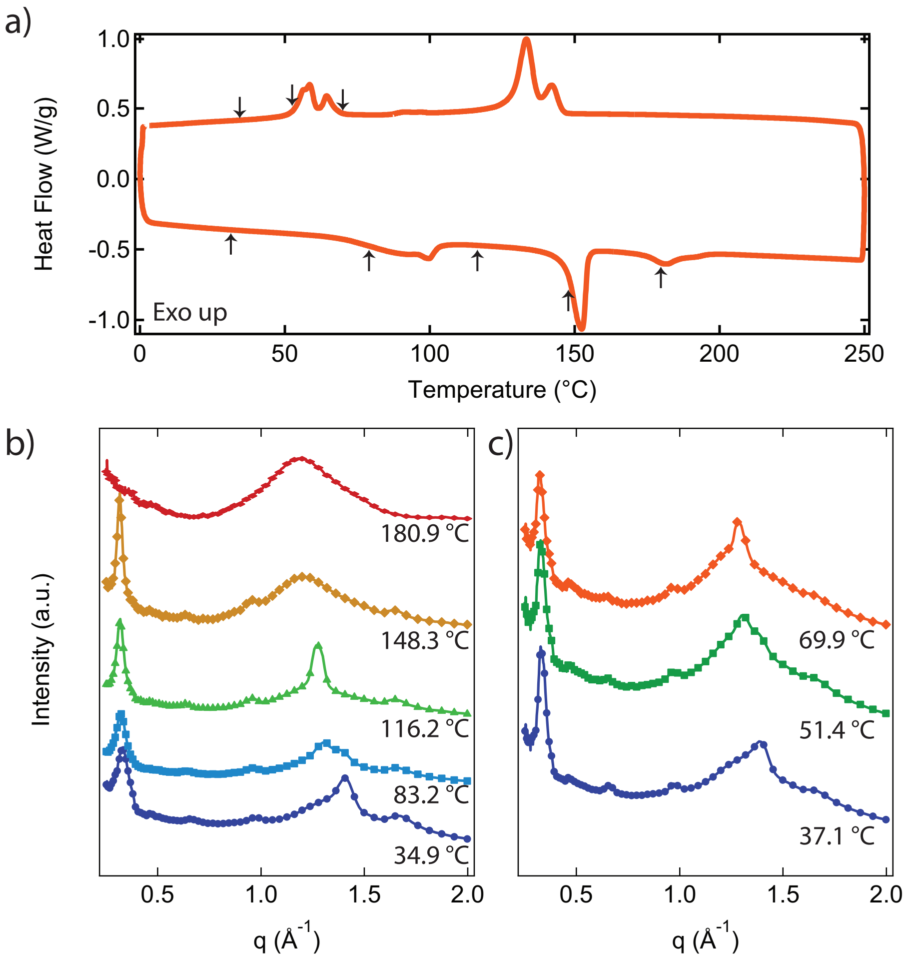

Figure B.18: Reduced Intensity vs. q GIWAXS data for the temperatures shown in Figure B.19. A corresponding differential scanning calorimetry (DSC) curve for a P3EPT:PVDF-TrFE blend with 50 wt.% P3EPT is shown in (a), and arrows indicate approximate points where scattering patterns were taken. Scattering profiles of a 50 wt.% P3EPT thin film at various temperatures are shown (b) during heating and (c) during cooling.

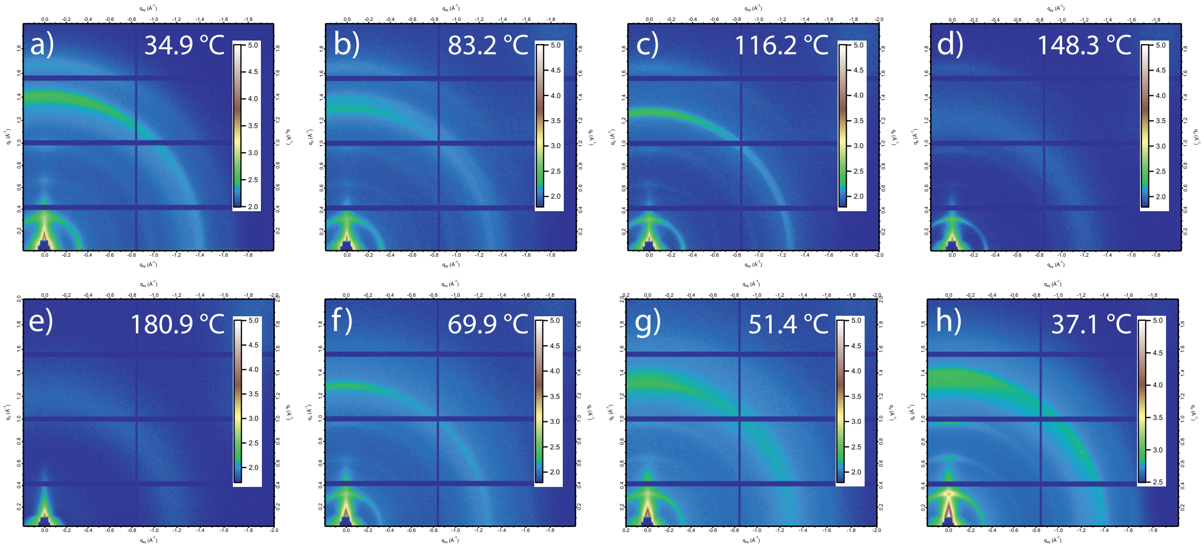

Figure B.19: Two-dimensional GIWAXS patterns of a P3EPT-PVDF-TrFE blend thin film with 50 wt.% P3EPT taken at various temperatures during annealing and cooling of the same sample. Several scattering patterns during heating are shown: (a) at 34.9 °C, (b) 83.2 °C near a phase transition of PVDF-TrFE, (c) 116.2 °C, (d) 148.3 °C close to the melting point of PVDF-TrFE, and (e) 180.9 °C near the melting point of P3EPT. Scattering images shown during cooling are (f) 69.9 °C reveals the reformation of crystallites of P3EPT and PVDF-TrFE, (g) 51.4 °C near a phase transition of PVDF-TrFE, and (h) cooled further to 37.1 °C.

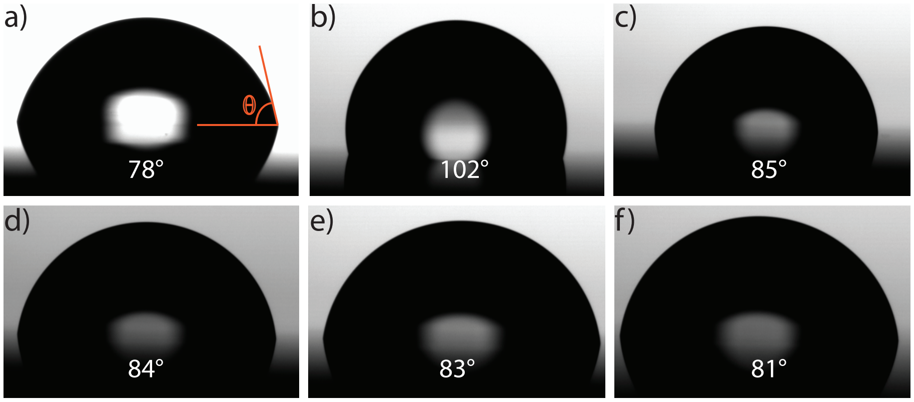

Figure B.20: Representative static water contact angle images for (a) P3EPT, (b) PVDF-TrFE, (c) a 10 wt.% P3EPT blend, (d) a 20 wt.% P3EPT blend, (e) a 35 wt.% P3EPT blend, and (f) a 50 wt.% P3EPT blend. The measured contact angles (indicated on the images) are 78°, 102°, 85°, 84°, 83°, and 81° for (a) through (f), respectively.

Appendix C

Supporting Information Chapter 4

C.1 Additional Information for Experimental and Computational Methods

Polymer fragments were modelled using Gaussian 09 [192]. An example of the sexithiophene-based unit cell used for simulations of poly(thiophene) is shown in Figure C.1.

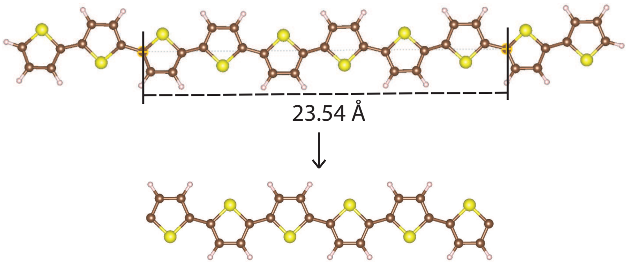

Figure C.1: Schematic of determining unit cell lengths for XCH calculations of infinitely long polymer chains. Example shown is for a thiophene chain.

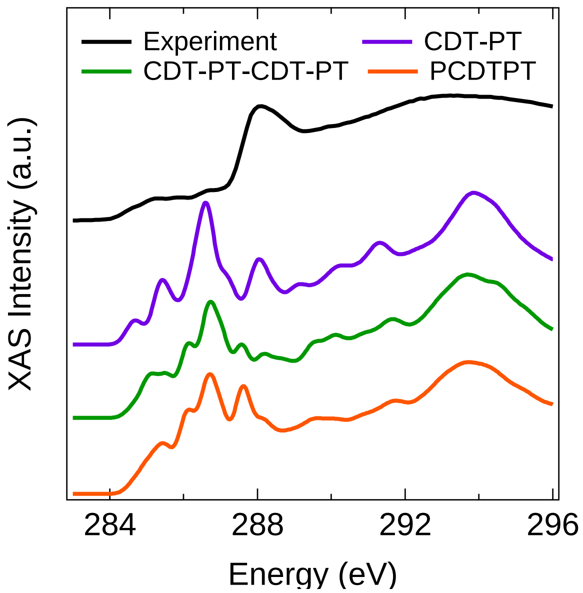

Figure C.2: Comparison of experimental carbon K edge NEXAFS data of the donor-acceptor polymer PCDTPT to simulated spectra of a single CDT-PT fragment, CDT-PT-CDT-PT fragment, and a PCDTPT model.

C.2 Simulated and Experimental Spectra of Donor-Acceptor Polymers

Additional NEXAFS data and simulations for PCDTPT, P(NDIOD-T2), and a furan-containing, diketopyrrolopyrrole-thiophene low-bandgap polymer PDPP2FT [174] are shown below.

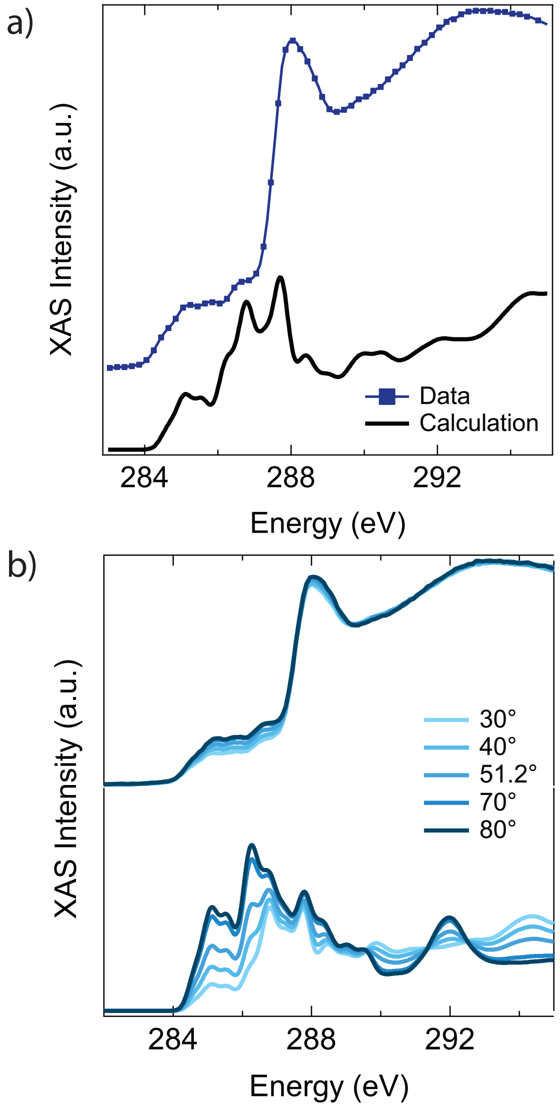

Figure C.3: Experimental and simulated (CDT-PT-CDT-PT fragment) carbon K edge data for PCDTPT is shown in (a). The qualitative trend in angle-dependent dependent data in the π^* region can be reproduced with calculations, as shown in (b). Experimental partial electron yield angle dependent data for an aligned PCDTPT sample is shown in the top portion of the graph, and simulated angle-dependant spectra assuming perfectly edge-on and aligned PCDTPT molecules is shown in the lower region.

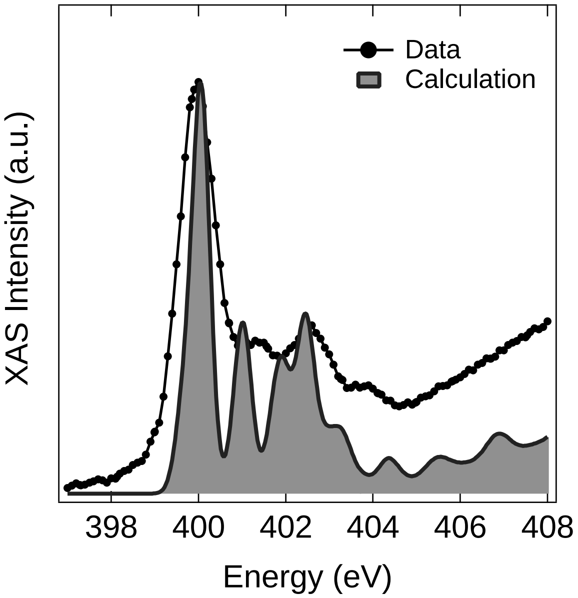

Figure C.4: Experimental vs simulated nitrogen K edge spectra at an incident angle of 51.2° of an aligned PCDTPT sample. Good agreement in relative intensities of the first few peaks is evident.

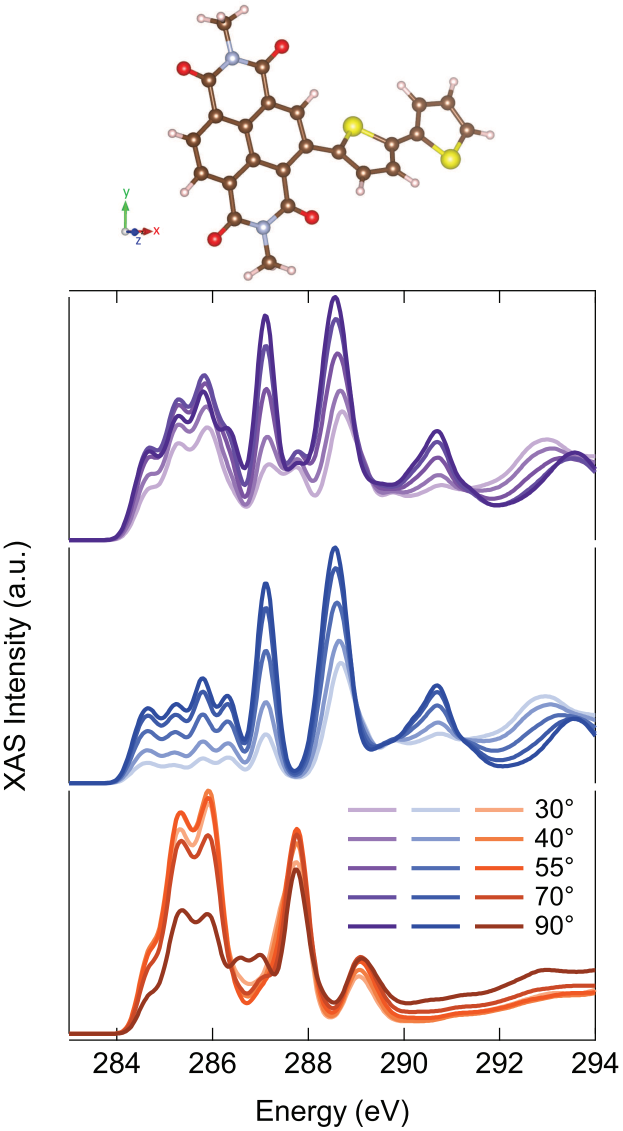

Figure C.5: DFT-optimized structure of P(NDIOD-T2) reveals a twist, or dihedral angle, between the NDI unit and the thiophene units. Simulated angle-dependent spectra in the C 1s→ π^* region are shown in the plot. The NDI unit was assumed to be perfectly edge-on, i.e. aligned with the y-axis. The angle-dependent spectra of carbon atoms only on the NDI unit are shown in the blue traced in the middle region of the plot. Angle-dependent spectra of thiophene atoms are shown as the orange traces in the lower region of the plot.

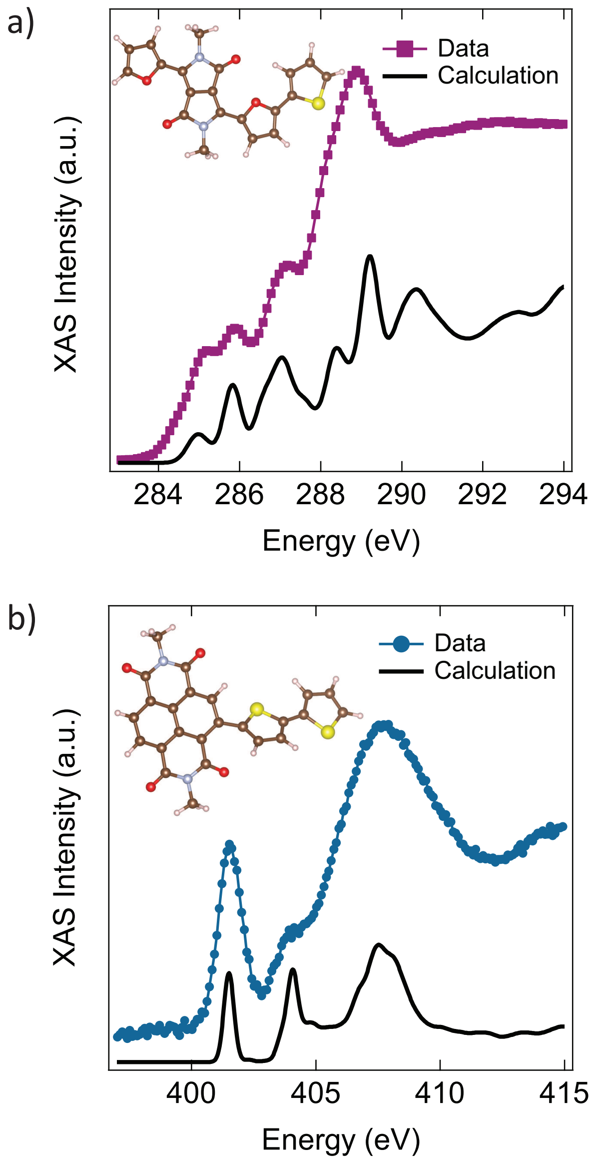

Figure C.6: Comparison of experimental and simulated spectra for donor-acceptor polymers. The carbon K edge spectra of PDPP2FT (structure shown in inset) is shown in (a). Nitrogen K edge spectra of P(NDIOD-T2) is shown in (b).

Bibliography

[1] M. He, F. Qiu, and Z. Lin, *Towards high-performance polymer-based thermoelectric materials*, *Energy Environ. Sci.* **6** (2013) 1352–1361.

[2] S. Holliday, J. E. Donaghey, and I. McCulloch, *Advances in charge carrier mobilities of semiconducting polymers used in organic transistors*, *Chem. Mater.* **26** (2014), no. 1 647–663, [http://pubs.acs.org/doi/pdf/10.1021/cm402421p].

[3] A. C. Arias, J. D. MacKenzie, I. McCulloch, J. Rivnay, and A. Salleo, *Materials and applications for large area electronics: Solution-based approaches*, *Chem. Rev.* **110** (2010), no. 1 3–24, [http://pubs.acs.org/doi/pdf/10.1021/cr900150b].

[4] A. Facchetti, *π-conjugated polymers for organic electronics and photovoltaic cell applications*, *Chem. Mater.* **23** (2011), no. 3 733–758, [http://pubs.acs.org/doi/pdf/10.1021/cm102419z].

[5] L. Dou, J. You, Z. Hong, Z. Xu, G. Li, R. A. Street, and Y. Yang, *25th anniversary article: A decade of organic/polymeric photovoltaic research*, *Adv. Mater.* **25** (2013), no. 46 6642–6671.

[6] P. Heremans, G. H. Gelinck, R. Müller, K.-J. Baeg, D.-Y. Kim, and Y.-Y. Noh, *Polymer and organic nonvolatile memory devices*, *Chem. Mater.* **23** (2011), no. 3 341–358, [http://pubs.acs.org/doi/pdf/10.1021/cm102006v].

[7] R. C. G. Naber, K. Asadi, P. W. M. Blom, D. M. de Leeuw, and B. de Boer, *Organic nonvolatile memory devices based on ferroelectricity*, *Adv. Mater.* **22** (2010), no. 9 933–945.

[8] M. Mas-Torrent and C. Rovira, *Role of molecular order and solid-state structure in organic field-effect transistors*, *Chem. Rev.* **111** (2011), no. 8 4833–4856, [http://pubs.acs.org/doi/pdf/10.1021/cr100142w].

[9] M. L. Chabinyc, M. F. Toney, R. J. Kline, I. McCulloch, and M. Heeney, *X-ray scattering study of thin films of poly(2,5-bis(3-alkylthiophen-2-yl)thieno[3,2-b]thiophene)*, *J. Am. Chem. Soc.* **129** (2007), no. 11 3226–3237, [http://pubs.acs.org/doi/pdf/10.1021/ja0670714].

[10] D. M. DeLongchamp, B. M. Vogel, Y. Jung, M. C. Gurau, C. A. Richter, O. A. Kirillov, J. Obrzut, D. A. Fischer, S. Sambasivan, L. J. Richter, and E. K. Lin, *Variations in semiconducting polymer microstructure and hole mobility with spin-coating speed*, *Chem. Mater.* **17** (2005), no. 23 5610–5612, [http://pubs.acs.org/doi/pdf/10.1021/cm0513637].

[11] P. Dhagat, H. M. Haverinen, R. J. Kline, Y. Jung, D. A. Fischer, D. M. DeLongchamp, and G. E. Jabbour, *Influence of dielectric surface chemistry on the microstructure and carrier mobility of an n-type organic semiconductor*, *Adv. Funct. Mater.* **19** (2009), no. 15 2365–2372.

[12] M. A. Brady, G. M. Su, and M. L. Chabinyc, *Recent progress in the morphology of bulk heterojunction photovoltaics*, *Soft Matter* **7** (2011) 11065–11077.

[13] R. Noriega, J. Rivnay, K. Vandewal, F. P. V. Koch, N. Stingelin, P. Smith, M. F. Toney, and A. Salleo, *A general relationship between disorder, aggregation and charge transport in conjugated polymers*, *Nat. Mater.* **12** (2013) 1038–1044.

[14] J. Rivnay, S. C. B. Mannsfeld, C. E. Miller, A. Salleo, and M. F. Toney, *Quantitative determination of organic semiconductor microstructure from the molecular to device scale*, *Chem. Rev.* **112** (2012) 5488–5519, [http://pubs.acs.org/doi/pdf/10.1021/cr3001109].

[15] H. Ade and A. P. Hitchcock, *Nexafs microscopy and resonant scattering: Composition and orientation probed in real and reciprocal space*, *Polymer* **49** (2008), no. 3 643 – 675.

[16] J. Stöhr, *NEXAFS Spectroscopy.* Springer Series in Surface Sciences. Springer, 1992.

[17] J. Genzer, E. J. Kramer, and D. A. Fischer, *Accounting for auger yield energy loss for improved determination of molecular orientation using soft x-ray absorption spectroscopy*, *J. Appl. Phys.* **92** (2002), no. 12 7070–7079.

[18] P. Mach, R. Pindak, A.-M. Levelut, P. Barois, H. T. Nguyen, H. Baltes, M. Hird, K. Toyne, A. Seed, J. W. Goodby, C. C. Huang, and L. Furenlid, *Structures of chiral smectic-C mesophases revealed by polarization-analyzed resonant x-ray scattering*, *Phys. Rev. E* **60** (1999) 6793–6802.

[19] M. Mezger, B. Jérôme, J. B. Kortright, M. Valvidares, E. M. Gullikson, A. Giglia, N. Mahne, and S. Nannarone, *Molecular orientation in soft matter thin films studied by resonant soft x-ray reflectivity*, *Phys. Rev. B* **83** (2011) 155406.

[20] C. Wang, D. H. Lee, A. Hexemer, M. I. Kim, W. Zhao, H. Hasegawa, H. Ade, and T. P. Russell, *Defining the nanostructured morphology of triblock copolymers*

using resonant soft x-ray scattering, *Nano Lett.* **11** (2011), no. 9 3906–3911, [http://dx.doi.org/10.1021/nl2020526].

[21] C. R. McNeill and H. Ade, *Soft x-ray characterisation of organic semiconductor films*, *J. Mater. Chem. C* **1** (2013) 187–201.

[22] B. A. Collins, J. E. Cochran, H. Yan, E. Gann, C. Hub, R. Fink, C. Wang, T. Schuettfort, C. R. McNeill, M. L. Chabinyc, and H. Ade, *Polarized x-ray scattering reveals non-crystalline orientational ordering in organic films*, *Nat. Mater.* **11** (2012) 536–543.

[23] E. Gann, A. T. Young, B. A. Collins, H. Yan, J. Nasiatka, H. A. Padmore, H. Ade, A. Hexemer, and C. Wang, *Soft X-ray scattering facility at the advanced light source with real-time data processing and analysis*, *Rev. Sci. Instrum.* **83** (2012), no. 4 045110.

[24] B. A. Collins and H. Ade, *Quantitative compositional analysis of organic thin films using transmission NEXAFS spectroscopy in an x-ray microscope*, *J. Electron. Spectrosc. Relat. Phenom.* **185** (2012), no. 57 119 – 128.

[25] C. R. McNeill, B. Watts, L. Thomsen, W. J. Belcher, N. C. Greenhamand, and P. C. Dastoor, *Nanoscale quantitative chemical mapping of conjugated polymer blends*, *Nano Lett.* **6** (2006), no. 6 1202–1206, [http://dx.doi.org/10.1021/nl060583w].

[26] G. A. Johansson, T. Tyliszczak, G. E. Mitchell, M. H. Keefe, and A. P. Hitchcock, *Three-dimensional chemical mapping by scanning transmission X-ray spectromicroscopy*, *J. Synchrotron Radiat.* **14** (2007), no. 5 395–402.

[27] D.-M. Smilgies, *Scherrer grain-size analysis adapted to grazing-incidence scattering with area detectors*, *J. Appl. Crystallogr.* **42** (2009), no. 6 1030–1034.

[28] M. A. Green, K. Emery, Y. Hishikawa, W. Warta, and E. D. Dunlop, *Solar cell efficiency tables (version 41)*, *Prog. Photovolt: Res. Appl.* **21** (2013), no. 1 1–11.

[29] M. T. Dang, L. Hirsch, G. Wantz, and J. D. Wuest, *Controlling the morphology and performance of bulk heterojunctions in solar cells. lessons learned from the benchmark poly(3-hexylthiophene):[6,6]-phenyl-c61-butyric acid methyl ester system*, *Chem. Rev.* **113** (2013), no. 0 3734–3765, [http://pubs.acs.org/doi/pdf/10.1021/cr300005u].

[30] P. Sonar, J. P. F. Lim, and K. L. Chan, *Organic non-fullerene acceptors for organic photovoltaics*, *Energy Environ. Sci.* **4** (2011) 1558–1574.

[31] T. V. Pho, F. M. Toma, M. L. Chabinyc, and F. Wudl, *Self-assembling decacyclene triimides prepared through a regioselective hextuple friedelcrafts carbamylation*, *Angew. Chem. Int. Ed.* **52** (2013), no. 5 1446–1451.

[32] J. T. Bloking, X. Han, A. T. Higgs, J. P. Kastrop, L. Pandey, J. E. Norton, C. Risko, C. E. Chen, J.-L. Brédas, M. D. McGehee, and A. Sellinger, *Solution-processed organic solar cells with power conversion efficiencies of 2.5% using benzothiadiazole/imide-based acceptors*, *Chem. Mater.* **23** (2011), no. 24 5484–5490, [http://pubs.acs.org/doi/pdf/10.1021/cm203111k].

[33] Y. Fang, A. K. Pandey, A. M. Nardes, N. Kopidakis, P. L. Burn, and P. Meredith, *A narrow optical gap small molecule acceptor for organic solar cells*, *Adv. Energy Mater.* **3** (2013), no. 1 54–59.

[34] C. B. Nielsen, E. Voroshazi, S. Holliday, K. Cnops, B. P. Rand, and I. McCulloch, *Efficient truxenone-based acceptors for organic photovoltaics*, *J. Mater. Chem. A* **1** (2013) 73–76.

[35] X. Zhang, Z. Lu, L. Ye, C. Zhan, J. Hou, S. Zhang, B. Jiang, Y. Zhao, J. Huang, S. Zhang, Y. Liu, Q. Shi, Y. Liu, and J. Yao, *A potential perylene diimide dimer-based acceptor material for highly efficient solution-processed non-fullerene organic solar cells with 4.03% efficiency*, *Adv. Mater.* **25** (2013) 5791–5797.

[36] E. Zhou, J. Cong, K. Hashimoto, and K. Tajima, *Control of miscibility and aggregation via the material design and coating process for high-performance polymer blend solar cells*, *Adv. Mater.* (2013) DOI: 10.1002/adma.201303170.

[37] T. Earmme, Y.-J. Hwang, N. M. Murari, S. Subramaniyan, and S. A. Jenekhe, *All-polymer solar cells with 3.3% efficiency based on naphthalene diimide-selenophene copolymer acceptor*, *J. Am. Chem. Soc.* **135** (2013), no. 40 14960–14963, [http://pubs.acs.org/doi/pdf/10.1021/ja4085429].

[38] D. Mori, H. Benten, I. Okada, H. Ohkita, and S. Ito, *Low-bandgap donor/acceptor polymer blend solar cells with efficiency exceeding 4%*, *Adv. Energy Mater.* **4** (2013) DOI: 10.1002/aenm.201301006.

[39] P. Cheng, L. Ye, X. Zhao, J. Hou, Y. Li, and X. Zhan, *Binary additives synergistically boost the efficiency of all-polymer solar cells up to 3.45%*, *Energy Environ. Sci.* (2013) DOI: 10.1039/C3EE43041C.

[40] Y. Zhang, A. K. Pandey, K. Tandy, G. K. Dutta, P. L. Burn, P. Meredith, E. B. Namdas, and S. Patil, *Channel II photocurrent quantification in narrow optical gap polymer-fullerene solar cells with complimentary acceptor absorption*, *Appl. Phys. Lett.* **102** (2013), no. 22 223302.

[41] I. A. Howard, F. Laquai, P. E. Keivanidis, R. H. Friend, and N. C. Greenham, *Perylene tetracarboxydiimide as an electron acceptor in organic solar cells: A study of charge generation and recombination*, *J. Phys. Chem C* **113** (2009), no. 50 21225–21232, [http://pubs.acs.org/doi/pdf/10.1021/jp907633g].

[42] S. D. Dimitrov and J. R. Durrant, *Materials design considerations for charge generation in organic solar cells*, *Chem. Mater.* **26** (2014) 616–630, [http://pubs.acs.org/doi/pdf/10.1021/cm402403z].

[43] M. T. Dang, L. Hirsch, and G. Wantz, *P3HT:PCBM, best seller in polymer photovoltaic research*, *Adv. Mater.* **23** (2011), no. 31 3597–3602.

[44] J. Peet, M. L. Senatore, A. J. Heeger, and G. C. Bazan, *The role of processing in the fabrication and optimization of plastic solar cells*, *Adv. Mater.* **21** (2009), no. 14-15 1521–1527.

[45] A. J. Moulé and K. Meerholz, *Morphology control in solution-processed bulk-heterojunction solar cell mixtures*, *Adv. Funct. Mater.* **19** (2009), no. 19 3028–3036.

[46] D. M. Ho and R. A. Pascal, *Decacyclene: a molecular propeller with helical crystals*, *Chem. Mater.* **5** (1993), no. 9 1358–1361, [http://pubs.acs.org/doi/pdf/10.1021/cm00033a029].

[47] T. Kimura, H. Koizumi, H. Kinoshita, and T. Ichikawa, *Formation of decacyclene nanowire by rapid vapor deposition*, *Jpn. J. Appl. Phys.* **46** (2007), no. 2 703–707.

[48] L. Schmidt-Mende, A. Fechtenkötter, K. Müllen, E. Moons, R. H. Friend, and J. D. MacKenzie, *Self-organized discotic liquid crystals for high-efficiency organic photovoltaics*, *Science* **293** (2001), no. 5532 1119–1122, [http://www.sciencemag.org/content/293/5532/1119.full.pdf].

[49] M. D. Watson, A. Fechtenkötter, and K. Müllen, *Big is beautiful- "aromaticity" revisited from the viewpoint of macromolecular and supramolecular benzene chemistry*, *Chem. Rev.* **101** (2001), no. 5 1267–1300, [http://pubs.acs.org/doi/pdf/10.1021/cr990322p].

[50] E. Charlet, E. Grelet, P. Brettes, H. Bock, H. Saadaoui, L. Cisse, P. Destruel, N. Gherardi, and I. Seguy, *Ultrathin films of homeotropically aligned columnar liquid crystals on indium tin oxide electrodes*, *Appl. Phys. Lett.* **92** (2008), no. 2 024107.

[51] E. Grelet, S. Dardel, H. Bock, M. Goldmann, E. Lacaze, and F. Nallet, *Morphology of open films of discotic hexagonal columnar liquid crystals as probed by grazing incidence x-ray diffraction*, *Eur. Phys. J. E Soft Matter* **31** (2010) 343–349.

[52] G. Schweicher, G. Gbabode, F. Quist, O. Debever, N. Dumont, S. Sergeyev, and Y. H. Geerts, *Homeotropic and planar alignment of discotic liquid crystals: The role of the columnar mesophase*, *Chem. Mater.* **21** (2009), no. 24 5867–5874, [http://pubs.acs.org/doi/pdf/10.1021/cm902634r].

[53] H. Iino, J. ichi Hanna, R. J. Bushby, B. Movaghar, B. J. Whitaker, and M. J. Cook, *Very high time-of-flight mobility in the columnar phases of a discotic liquid crystal*, *Appl. Phys. Lett.* **87** (2005), no. 13 132102.

[54] D. Adam, P. Schuhmacher, J. Simmerer, L. Haussling, K. Siemensmeyer, K. H. Etzbachi, H. Ringsdorf, and D. Haarer, *Fast photoconduction in the highly ordered columnar phase of a discotic liquid crystal*, *Nature* **371** (1994), no. 6493 141–143.

[55] A. Bayer, J. Kopitzke, F. Noll, A. Seifert, and J. H. Wendorff, *Polymer dispersed discotics: Structure, dynamics, and optoelectronic properties*, *Macromolecules* **34** (2001), no. 11 3600–3606, [http://pubs.acs.org/doi/pdf/10.1021/ma001470g].

[56] K. Hirota, K. Tajima, and K. Hashimoto, *Physicochemical study of discotic liquid crystal decacyclene derivative and utilization in polymer photovoltaic devices*, *Synt. Met.* **157** (2007), no. 67 290 – 296.

[57] W. Ma, C. Yang, X. Gong, K. Lee, and A. J. Heeger, *Thermally stable, efficient polymer solar cells with nanoscale control of the interpenetrating network morphology*, *Adv. Funct. Mater.* **15** (2005), no. 10 1617–1622.

[58] X. Yang, J. Loos, S. C. Veenstra, W. J. H. Verhees, M. M. Wienk, J. M. Kroon, M. A. J. Michels, and R. A. J. Janssen, *Nanoscale morphology of high-performance polymer solar cells*, *Nano Lett.* **5** (2005), no. 4 579–583, [http://pubs.acs.org/doi/pdf/10.1021/nl048120i].

[59] Y. Zhou, L. Ding, K. Shi, Y.-Z. Dai, N. Ai, J. Wang, and J. Pei, *A non-fullerene small molecule as efficient electron acceptor in organic bulk heterojunction solar cells*, *Adv. Mater.* **24** (2012), no. 7 957–961.

[60] Y. Lin, P. Cheng, Y. Li, and X. Zhan, *A 3D star-shaped non-fullerene acceptor for solution-processed organic solar cells with a high open-circuit voltage of 1.18 V*, *Chem. Commun.* **48** (2012) 4773–4775.

[61] S. M. Abdullah, Z. Ahmad, F. Aziz, and K. Sulaiman, *Investigation of VOPcPhO as an acceptor material for bulk heterojunction solar cells*, *Org. Electron.* **13** (2012), no. 11 2532 – 2537.

[62] L. Cisse, P. Destruel, S. Archambeau, I. Seguy, P. Jolinat, H. Bock, and E. Grelet, *Measurement of the exciton diffusion length in discotic columnar liquid crystals: Comparison between homeotropically oriented and non-oriented samples*, *Chem. Phys. Lett.* **476** (2009), no. 13 89 – 91.

[63] R. A. L. Jones, L. J. Norton, E. J. Kramer, R. J. Composto, R. S. Stein, T. P. Russell, A. Mansour, A. Karim, G. P. Felcher, M. H. Rafailovich, J. Sokolov, X. Zhao, and S. A. Schwarz, *The form of the enriched surface layer in polymer blends*, *Europhys. Lett.* **12** (1990), no. 1 41.

[64] R. A. L. Jones, E. J. Kramer, M. H. Rafailovich, J. Sokolov, and S. A. Schwarz, *Surface enrichment in an isotopic polymer blend*, *Phys. Rev. Lett.* **62** (1989) 280–283.

[65] L. J. Norton, E. J. Kramer, F. S. Bates, M. D. Gehlsen, R. A. L. Jones, A. Karim, G. P. Felcher, and R. Kleb, *Neutron reflectometry study of surface segregation in an isotopic poly(ethylenepropylene) blend: Deviation from mean-field theory*, *Macromolecules* **28** (1995), no. 25 8621–8628, [http://pubs.acs.org/doi/pdf/10.1021/ma00129a022].

[66] N. Shin, J. Kang, L. J. Richter, V. M. Prabhu, R. J. Kline, D. A. Fischer, D. M. DeLongchamp, M. F. Toney, S. K. Satija, D. J. Gundlach, B. Purushothaman, J. E. Anthony, and D. Y. Yoon, *Vertically segregated structure and properties of small molecule-polymer blend semiconductors for organic thin-film transistors*, *Adv. Funct. Mater.* **23** (2013), no. 3 366–376.

[67] J. Kang, N. Shin, D. Y. Jang, V. M. Prabhu, and D. Y. Yoon, *Structure and properties of small molecule-polymer blend semiconductors for organic thin film transistors*, *J. Am. Chem. Soc.* **130** (2008), no. 37 12273–12275, [http://pubs.acs.org/doi/pdf/10.1021/ja804013n].

[68] A. Kumar, M. A. Baklar, K. Scott, T. Kreouzis, and N. Stingelin-Stutzmann, *Efficient, stable bulk charge transport in crystalline/crystalline semiconductor-insulator blends*, *Adv. Mater.* **21** (2009), no. 44 4447–4451.

[69] S. Goffri, C. Müller, N. Stingelin-Stutzmann, D. W. Brieby, C. P. Radano, J. W. Andreasen, R. Thompson, R. A. J. Janssen, M. M. Nielsen, P. Smith, and H. Sirringhaus, *Multicomponent semiconducting polymer systems with low crystallization-induced percolation threshold*, *Nat. Mater.* **5** (2006) 950–956.

[70] H. Wang, M. Shah, V. Ganesan, M. L. Chabinyc, and Y.-L. Loo, *Tail state-assisted charge injection and recombination at the electron-collecting interface of P3HT:PCBM bulk-heterojunction polymer solar cells*, *Adv. Energy Mater.* **2** (2012), no. 12 1447–1455.

[71] H. Wang, E. D. Gomez, J. Kim, Z. Guan, C. Jaye, D. A. Fischer, A. Kahn, and Y.-L. Loo, *Device characteristics of bulk-heterojunction polymer solar cells are independent of interfacial segregation of active layers*, *Chem. Mater.* **23** (2011), no. 8 2020–2023, [http://pubs.acs.org/doi/pdf/10.1021/cm200320u].

[72] D. S. Germack, C. K. Chan, R. J. Kline, D. A. Fischer, D. J. Gundlach, M. F. Toney, L. J. Richter, and D. M. DeLongchamp, *Interfacial segregation in polymer/fullerene blend films for photovoltaic devices*, *Macromolecules* **43** (2010), no. 8 3828–3836, [http://pubs.acs.org/doi/pdf/10.1021/ma100027b].

[73] N. D. Treat, J. A. N. Malik, O. Reid, L. Yu, S. Christopher G, G. Rumbles, C. J. Hawker, M. L. Chabinyc, P. Smith, and N. Stingelin, *Microstructure formation in molecular and polymer semiconductors assisted by nucleation agents*, *Nat. Mater.* **12** (2013) 628–633.

[74] G. Hähner, *Near edge X-ray absorption fine structure spectroscopy as a tool to probe electronic and structural properties of thin organic films and liquids*, *Chem. Soc. Rev.* **35** (2006) 1244–1255.

[75] J. Stöhr and M. Samant, *Liquid crystal alignment by rubbed polymer surfaces: a microscopic bond orientation model*, *J. Electron Spectrosc. Relat. Phenom.* **98-99** (1999) 189 – 207.

[76] A. Salleo, R. J. Kline, D. M. DeLongchamp, and M. L. Chabinyc, *Microstructural characterization and charge transport in thin films of conjugated polymers*, *Adv. Mater.* **22** (2010), no. 34 3812–3838.

[77] W. E. Wallace, D. A. Fischer, K. Efimenko, W.-L. Wu, and J. Genzer, *Polymer chain relaxation: Surface outpaces bulk*, *Macromolecules* **34** (2001), no. 15 5081–5082, [http://pubs.acs.org/doi/pdf/10.1021/ma002075t].

[78] L. R. Pattison, A. Hexemer, E. J. Kramer, S. Krishnan, P. M. Petroff, and D. A. Fischer, *Probing the ordering of semiconducting fluorene-thiophene copolymer surfaces on rubbed polyimide substrates by near edge X-ray absorption fine structure*, *Macromolecules* **39** (2006), no. 6 2225–2231, [http://pubs.acs.org/doi/pdf/10.1021/ma0521912].

[79] D. M. DeLongchamp, R. J. Kline, and A. Herzing, *Nanoscale structure measurements for polymer-fullerene photovoltaics*, *Energy Environ. Sci.* **5** (2012) 5980–5993.

[80] C. R. McNeill, *Imaging the domain structure of organic semiconductor films*, *J. Polym. Sci. Part B Polym. Phys.* **49** (2011), no. 13 909–919.

[81] D. M. DeLongchamp and R. J. Kline, *Characterization of Order and Orientation in Semiconducting Polymers*, pp. 27–66. Wiley-VCH Verlag GmbH & Co. KGaA, 2012.

[82] J. T. Rogers, K. Schmidt, M. F. Toney, G. C. Bazan, and E. J. Kramer, *Time-resolved structural evolution of additive-processed bulk heterojunction solar cells*, *J. Am. Chem. Soc.* **134** (2012), no. 6 2884–2887, [http://pubs.acs.org/doi/pdf/10.1021/ja2104747].

[83] W. Chen, M. P. Nikiforov, and S. B. Darling, *Morphology characterization in organic and hybrid solar cells*, *Energy Environ. Sci.* **5** (2012) 8045–8074.

[84] J. L. Baker, L. H. Jimison, S. Mannsfeld, S. Volkman, S. Yin, V. Subramanian, A. Salleo, A. P. Alivisatos, and M. F. Toney, *Quantification of thin film crystallographic orientation using x-ray diffraction with an area detector*, *Langmuir* **26** (2010), no. 11 9146–9151, [http://pubs.acs.org/doi/pdf/10.1021/la904840q]. PMID: 20361783.

[85] N. D. Treat, M. A. Brady, G. Smith, M. F. Toney, E. J. Kramer, C. J. Hawker, and M. L. Chabinyc, *Interdiffusion of PCBM and P3HT reveals miscibility in a photovoltaically active blend*, *Adv. Energy Mater.* **1** (2011), no. 1 82–89.

[86] P. Scherrer *Gottinger Nachrichten Math. Phys* **2** (1918) 98–100.

[87] K. Asadi, P. de Bruyn, P. W. M. Blom, and D. M. de Leeuw, *Origin of the efficiency enhancement in ferroelectric functionalized organic solar cells*, *Appl. Phys. Lett.* **98** (2011), no. 18 183301.

[88] Y. Yuan, Z. Xiao, B. Yang, and J. Huang, *Arising applications of ferroelectric materials in photovoltaic devices*, *J. Mater. Chem. A* **2** (2014) 6027–6041.

[89] Y. Yuan, T. J. Reece, P. Sharma, S. Poddar, S. Ducharme, A. Gruverman, Y. Yang, and J. Huang, *Efficiency enhancement in organic solar cells with ferroelectric polymers*, *Nat. Mater.* **10** (2011) 296–302.

[90] Y. Yuan, P. Sharma, Z. Xiao, S. Poddar, A. Gruverman, S. Ducharme, and J. Huang, *Understanding the effect of ferroelectric polarization on power conversion efficiency of organic photovoltaic devices*, *Energy Environ. Sci.* **5** (2012) 8558–8563.

[91] K. S. Nalwa, J. A. Carr, R. C. Mahadevapuram, H. K. Kodali, S. Bose, Y. Chen, J. W. Petrich, B. Ganapathysubramanian, and S. Chaudhary, *Enhanced charge separation in organic photovoltaic films doped with ferroelectric dipoles*, *Energy Environ. Sci.* **5** (2012) 7042–7049.

[92] S.-T. Han, Y. Zhou, and V. A. L. Roy, *Towards the development of flexible non-volatile memories*, *Adv. Mater.* **25** (2013), no. 38 5425–5449.

[93] Q.-D. Ling, D.-J. Liaw, C. Zhu, D. S.-H. Chan, E.-T. Kang, and K.-G. Neoh, *Polymer electronic memories: Materials, devices and mechanisms*, *Prog. Polym. Sci.* **33** (2008), no. 10 917 – 978.

[94] K. Asadi, M. Li, P. W. Blom, M. Kemerink, and D. M. de Leeuw, *Organic ferroelectric opto-electronic memories*, *Mater. Today* **14** (2011), no. 12 592 – 599.

[95] A. J. Lovinger, *Ferroelectric polymers*, *Science* **220** (1983) 1115–1121.

[96] F. Baltá Calleja, A. Arche, T. Ezquerra, C. Cruz, F. Batallán, B. Frick, and E. Cabarcos, *Structure and properties of ferroelectric copolymers of poly(vinylidene fluoride)*, in *Structure in Polymers with Special Properties* (H.-G. Zachmann, ed.), vol. 108 of *Adv. Polym. Sci.*, pp. 1–48. Springer Berlin Heidelberg, 1993.

[97] K. Asadi, D. M. de Leeuw, B. de Boer, and P. W. M. Blom, *Organic non-volatile memories from ferroelectric phase-separated blends*, *Nat. Mater.* **7** (2008) 547–550.

[98] K. Asadi, T. G. de Boer, P. W. M. Blom, and D. M. de Leeuw, *Tunable injection barrier in organic resistive switches based on phase-separated ferroelectricsemiconductor blends*, *Adv. Funct. Mater.* **19** (2009), no. 19 3173–3178.

[99] M. Kemerink, K. Asadi, P. W. Blom, and D. M. de Leeuw, *The operational mechanism of ferroelectric-driven organic resistive switches*, *Org. Electron.* **13** (2012), no. 1 147 – 152.

[100] V. Khikhlovskyi, R. Wang, A. J. J. M. van Breemen, G. H. Gelinck, R. A. J. Janssen, and M. Kemerink, *Nanoscale organic ferroelectric resistive switches*, *J. Phys. Chem. C* **118** (2014), no. 6 3305–3312, [http://pubs.acs.org/doi/pdf/10.1021/jp409757m].

[101] A. van Breemen, T. Zaba, V. Khikhlovskyi, J. Michels, R. Janssen, M. Kemerink, and G. Gelinck, *Surface directed phase separation of semiconductor ferroelectric polymer blends and their use in non-volatile memories*, *Adv. Funct. Mater.* **25** (2015), no. 2 278–286.

[102] T. Araki, H. Ade, J. M. Stubbs, D. C. Sundberg, G. E. Mitchell, J. B. Kortright, and A. L. D. Kilcoyne, *Resonant soft x-ray scattering from structured polymer nanoparticles*, *Appl. Phys. Lett.* **89** (2006), no. 12 124106.

[103] B. Henke, E. Gullikson, and J. Davis, *X-ray interactions: Photoabsorption, scattering, transmission, and reflection at E = 50-30,000 eV, Z = 1-92*, *Atomic Data and Nuclear Data Tables* **54** (1993), no. 2 181 – 342.

[104] H. Ade, X. Zhang, S. Cameron, C. Costello, J. Kirz, and S. Williams, *Chemical contrast in X-ray microscopy and spatially resolved XANES spectroscopy of organic specimens*, *Science* **258** (1992), no. 5084 972–975, [http://www.sciencemag.org/content/258/5084/972.full.pdf].

[105] K. Asadi, H. J. Wondergem, R. S. Moghaddam, C. R. McNeill, N. Stingelin, B. Noheda, P. W. M. Blom, and D. M. de Leeuw, *Spinodal decomposition of blends of semiconducting and ferroelectric polymers*, *Adv. Funct. Mater.* **21** (2011), no. 10 1887–1894.

[106] L. Nougaret, H. G. Kassa, R. Cai, T. Patois, B. Nysten, A. J. J. M. van Breemen, G. H. Gelinck, D. M. de Leeuw, A. Marrani, Z. Hu, and A. M. Jonas, *Nanoscale design of multifunctional organic layers for low-power high-density memory devices*, *ACS Nano* **8** (2014), no. 4 3498–3505, [http://pubs.acs.org/doi/pdf/10.1021/nn406503g].

[107] M. Li, N. Stingelin, J. J. Michels, M.-J. Spijkman, K. Asadi, R. Beerends, F. Biscarini, P. W. M. Blom, and D. M. de Leeuw, *Processing and low voltage switching of organic ferroelectric phase-separated bistable diodes*, *Adv. Funct. Mater.* **22** (2012), no. 13 2750–2757.

[108] M. A. Khan, U. S. Bhansali, M. N. Almadhoun, I. N. Odeh, D. Cha, and H. N. Alshareef, *High-performance ferroelectric memory based on phase-separated films of polymer blends*, *Adv. Funct. Mater.* **24** (2013), no. 10 1372–1381.

[109] J. S. Noland, N. N.-C. Hsu, R. Saxon, and J. M. Schmitt, *Compatible High Polymers: Poly(vinylidene fluoride) Blends with Homopolymers of Methyl and Ethyl Methacrylate*, vol. 99, ch. 3, pp. 15–28. 1971. http://pubs.acs.org/doi/pdf/10.1021/ba-1971-0099.ch002.

[110] M. Li, N. Stingelin, J. J. Michels, M.-J. Spijkman, K. Asadi, K. Feldman, P. W. M. Blom, and D. M. de Leeuw, *Ferroelectric phase diagram of PVDF:PMMA*, *Macromolecules* **45** (2012), no. 18 7477–7485, [http://pubs.acs.org/doi/pdf/10.1021/ma301460h].

[111] M. Li, H. J. Wondergem, M.-J. Spijkman, K. Asadi, I. Katsouras, P. W. M. Blom, and D. M. de Leeuw, *Revisiting the delta-phase of poly(vinylidene fluoride) for solution-processed ferroelectric thin films*, *Nat. Mater.* **12** (2013) 433–438.

[112] S. J. Kang, Y. J. Park, I. Bae, K. J. Kim, H.-C. Kim, S. Bauer, E. L. Thomas, and C. Park, *Printable ferroelectric PVDF/PMMA blend films with ultralow roughness for low voltage non-volatile polymer memory*, *Adv. Funct. Mater.* **19** (2009), no. 17 2812–2818.

[113] V. Ho, B. W. Boudouris, and R. A. Segalman, *Tuning polythiophene crystallization through systematic side chain functionalization*, *Macromolecules* **43** (2010), no. 19 7895–7899, [http://pubs.acs.org/doi/pdf/10.1021/ma101697m].

[114] T. J. Prosa, M. J. Winokur, and R. D. McCullough, *Evidence of a novel side chain structure in regioregular poly(3-alkylthiophenes)*, *Macromolecules* **29** (1996), no. 10 3654–3656, [http://pubs.acs.org/doi/pdf/10.1021/ma951510u].

[115] G. M. Su, T. V. Pho, N. D. Eisenmenger, C. Wang, F. Wudl, E. J. Kramer, and M. L. Chabinyc, *Linking morphology and performance of organic solar cells based on decacyclene triimide acceptors*, *J. Mater. Chem. A* **2** (2014) 1781–1789.

[116] H. J. Jung, J. Chang, Y. J. Park, S. J. Kang, B. Lotz, J. Huh, and C. Park, *Shear-induced ordering of ferroelectric crystals in spin-coated thin poly(vinylidene fluoride-co-trifluoroethylene) films*, *Macromolecules* **42** (2009), no. 12 4148–4154, [http://pubs.acs.org/doi/pdf/10.1021/ma900422n].

[117] V. Causin, C. Marega, A. Marigo, L. Valentini, and J. M. Kenny, *Crystallization and melting behavior of poly(3-butylthiophene), poly(3-octylthiophene), and poly(3-dodecylthiophene)*, *Macromolecules* **38** (2005), no. 2 409–415, [

[118] T. J. Prosa, M. J. Winokur, J. Moulton, P. Smith, and A. J. Heeger, *X-ray structural studies of poly(3-alkylthiophenes): an example of an inverse comb*, *Macromolecules* **25** (1992), no. 17 4364–4372, [http://pubs.acs.org/doi/pdf/10.1021/ma00043a019].

[119] X. Xiao, Z. Hu, Z. Wang, and T. He, *Study on the single crystals of poly(3-octylthiophene) induced by solvent-vapor annealing*, *J. Phys. Chem. B* **113** (2009), no. 44 14604–14610, [http://pubs.acs.org/doi/pdf/10.1021/jp9064505].

[120] L. H. Jimison, A. Salleo, M. L. Chabinyc, D. P. Bernstein, and M. F. Toney, *Correlating the microstructure of thin films of poly[5,5-bis(3-dodecyl-2-thienyl)-2,2-bithiophene] with charge transport: Effect of dielectric surface energy and thermal annealing*, *Phys. Rev. B* **78** (2008) 125319.

[121] D. M. DeLongchamp, R. J. Kline, E. K. Lin, D. Fischer, L. J. Richter, L. A. Lucas, M. Heeney, I. McCulloch, and J. E. Northrup, *High carrier mobility polythiophene thin films: Structure determination by experiment and theory*, *Adv. Mater.* **19** (2007), no. 6 833–837.

[122] B. Watts, T. Schuettfort, and C. R. McNeill, *Mapping of domain orientation and molecular order in polycrystalline semiconducting polymer films with soft X-ray microscopy*, *Adv. Funct. Mater.* **21** (2011), no. 6 1122–1131.

[123] G. M. Su, E. Lim, A. R. Jacobs, E. J. Kramer, and M. L. Chabinyc, *Polymer side chain modification alters phase separation in ferroelectric-semiconductor polymer blends for organic memory*, *ACS Macro Lett.* **3** (2014), no. 12 1244–1248, [http://dx.doi.org/10.1021/mz5005647].

[124] C. R. McNeill, K. Asadi, B. Watts, P. W. M. Blom, and D. M. de Leeuw, *Structure of phase-separated ferroelectric/semiconducting polymer blends for organic non-volatile memories*, *Small* **6** (2010), no. 4 508–512.

[125] B. A. Collins, Z. Li, J. R. Tumbleston, E. Gann, C. R. McNeill, and H. Ade, *Absolute measurement of domain composition and nanoscale size distribution explains performance in PTB7:PC71BM solar cells*, *Adv. Energy Mater.* **3** (2013), no. 1 65–74.

[126] J.-S. Kim, P. K. H. Ho, C. E. Murphy, and R. H. Friend, *Phase separation in polyfluorene-based conjugated polymer blends: Lateral and vertical analysis of blend spin-cast thin films*, *Macromolecules* **37** (2004), no. 8 2861–2871, [http://dx.doi.org/10.1021/ma035750i].

[127] J. Chappell, D. G. Lidzey, P. C. Jukes, A. M. Higgins, R. L. Thompson, S. O'Connor, I. Grizzi, R. Fletcher, J. O'Brien, M. Geoghegan, and R. A. L. Jones, *Correlating structure with fluorescence emission in phase-separated conjugated-polymer blends*, *Nat. Mater.* **2** (2003) 616–621.

[128] A. M. Higgins, S. J. Martin, R. L. Thompson, J. Chappell, M. Voigt, D. G. Lidzey, R. A. L. Jones, and M. Geoghegan, *Surface segregation and self-stratification in blends of spin-cast polyfluorene derivatives*, *J. Phys.: Condens. Matter* **17** (2005), no. 8 1319–1328.

[129] G. Li Destri, T. F. Keller, M. Catellani, F. Punzo, K. D. Jandt, and G. Marletta, *Crystalline monolayer ordering at substrate/polymer interfaces in poly(3-hexylthiophene) ultrathin films*, *Macromol. Chem. Phys.* **212** (2011), no. 9 905–914.

[130] M. Morra, C. Della Volpe, and S. Siboni, *Polymer Interfaces and Emulsions.* CRC Press, 1999.

[131] K. E. Sohn, M. D. Dimitriou, J. Genzer, D. A. Fischer, C. J. Hawker, and E. J. Kramer, *Determination of the electron escape depth for NEXAFS spectroscopy*, *Langmuir* **25** (2009), no. 11 6341–6348, [http://dx.doi.org/10.1021/la803951y].

[132] B. J. Factor, T. P. Russell, and M. F. Toney, *Surface-induced ordering of an aromatic polyimide*, *Phys. Rev. Lett.* **66** (Mar, 1991) 1181–1184.

[133] B. J. Factor, T. P. Russell, and M. F. Toney, *Grazing incidence X-ray scattering studies of thin films of an aromatic polyimide*, *Macromolecules* **26** (1993), no. 11 2847–2859, [http://dx.doi.org/10.1021/ma00063a033].

[134] L. A. Perez, P. Zalar, L. Ying, K. Schmidt, M. F. Toney, T.-Q. Nguyen, G. C. Bazan, and E. J. Kramer, *Effect of backbone regioregularity on the structure and orientation of a donor-acceptor semiconducting copolymer*, *Macromolecules* **47** (2014), no. 4 1403–1410, [http://dx.doi.org/10.1021/ma4019679].

[135] W. C. Tsoi, S. J. Spencer, L. Yang, A. M. Ballantyne, P. G. Nicholson, A. Turnbull, A. G. Shard, C. E. Murphy, D. D. C. Bradley, J. Nelson, and J.-S. Kim, *Effect of crystallization on the electronic energy levels and thin film morphology of P3HT:PCBM blends*, *Macromolecules* **44** (2011), no. 8 2944–2952, [http://dx.doi.org/10.1021/ma102841e].

[136] S. Sweetnam, K. R. Graham, G. O. Ngongang Ndjawa, T. Heumüller, J. A. Bartelt, T. M. Burke, W. Li, W. You, A. Amassian, and M. D. McGehee, *Characterization of the polymer energy landscape in polymer:fullerene bulk heterojunctions with pure and mixed phases*, *J. Am. Chem. Soc.* **136** (2014), no. 40 14078–14088, [http://dx.doi.org/10.1021/ja505463r].

[137] D. M. DeLongchamp, R. J. Kline, D. A. Fischer, L. J. Richter, and M. F. Toney, *Molecular characterization of organic electronic films*, *Adv. Mater.* **23** (2011), no. 3 319–337.

[138] U. Aygül, H. Peisert, D. Batchelor, U. Dettinger, M. Ivanovic, A. Tournebize, S. Mangold, M. Förster, I. Dumsch, S. Kowalski, S. Allard, U. Scherf, and T. Chassé, *Molecular orientation in polymer/fullerene blend films and the influence of annealing*, *Solar Energy Materials & Solar Cells* **128** (2014) 119 – 125.

[139] E. Gann, C. R. McNeill, M. Szumilo, H. Sirringhaus, M. Sommer, S. Maniam, S. J. Langford, and L. Thomsen, *Near-edge X-ray absorption fine-structure spectroscopy of naphthalene diimide-thiophene co-polymers*, *J. Chem. Phys.* **140** (2014), no. 16 164710.

[140] T. Schuettfort, L. Thomsen, and C. R. McNeill, *Observation of a distinct surface molecular orientation in films of a high mobility conjugated polymer*, *J. Am. Chem. Soc.* **135** (2013), no. 3 1092–1101, [http://dx.doi.org/10.1021/ja310240q].

[141] G. D. Scholes and G. Rumbles, *Excitons in nanoscale systems*, *Nat. Mater.* **5** (2006) 683–696.

[142] E. Hendry, J. M. Schins, L. P. Candeias, L. D. A. Siebbeles, and M. Bonn, *Efficiency of exciton and charge carrier photogeneration in a semiconducting polymer*, *Phys. Rev. Lett.* **92** (2004) 196601.

[143] M. Gliboff, D. Sulas, D. Nordlund, D. W. deQuilettes, P. D. Nguyen, G. T. Seidler, X. Li, and D. S. Ginger, *Direct measurement of acceptor group localization on donor-acceptor polymers using resonant auger spectroscopy*, *J. Phys. Chem. C* **118** (2014), no. 10 5570–5578, [http://dx.doi.org/10.1021/jp412150j].

[144] D. A. Outka, J. Stöhr, J. Rabe, J. D. Swalen, and H. H. Rotermund, *Orientation of arachidate chains in langmuir-blodgett monolayers on Si(111)*, *Phys. Rev. Lett.* **59** (Sep, 1987) 1321–1324.

[145] D. A. Outka, J. Stöhr, J. P. Rabe, and J. D. Swalen, *The orientation of langmuir-blodgett monolayers using NEXAFS*, *J. Chem. Phys.* **88** (1988), no. 6 4076–4087.

[146] G. Hähner, M. Kinzler, C. Wöll, M. Grunze, M. K. Scheller, and L. S. Cederbaum, *Near edge X-ray-absorption fine-structure determination of alkyl-chain orientation: Breakdown of the "building-block" scheme*, *Phys. Rev. Lett.* **67** (1991) 851–854.

[147] L. G. M. Pettersson, H. Ågren, B. L. Schürmann, A. Lippitz, and W. E. S. Unger, *Assembly and decomposition of building blocks to analyze polymer NEXAFS spectra*, *Int. J. Quantum Chem.* **63** (1997), no. 3 749–765.

[148] V. Carravetta, H. Ågren, L. G. M. Pettersson, and O. Vahtras, *Near-edge core photoabsorption in polyenes*, *J. Chem. Phys.* **102** (1995), no. 14 5589–5597.

[149] L. J. Gamble, B. Ravel, D. A. Fischer, and D. G. Castner, *Surface structure and orientation of PTFE films determined by experimental and FEFF8-calculated NEXAFS spectra*, *Langmuir* **18** (2002), no. 6 2183–2189, [http://dx.doi.org/10.1021/la011258l].

[150] M. D. Dimitriou, Z. Zhou, H.-S. Yoo, K. L. Killops, J. A. Finlay, G. Cone, H. S. Sundaram, N. A. Lynd, K. P. Barteau, L. M. Campos, D. A. Fischer, M. E. Callow, J. A. Callow, C. K. Ober, C. J. Hawker, and E. J. Kramer, *A general approach to controlling the surface composition of poly(ethylene oxide)-based block copolymers for antifouling coatings*, *Langmuir* **27** (2011), no. 22 13762–13772, [http://dx.doi.org/10.1021/la202509m].

[151] W. van Zoelen, R. N. Zuckermann, and R. A. Segalman, *Tunable surface properties from sequence-specific polypeptoidpolystyrene block copolymer thin films*, *Macromolecules* **45** (2012), no. 17 7072–7082, [http://dx.doi.org/10.1021/ma3009806].

[152] H. Ågren, V. Carravetta, O. Vahtras, and L. G. M. Pettersson, *Orientational probing of polymeric thin films by NEXAFS: Calculations on polytetrafluoroethylene*, *Phys. Rev. B* **51** (Jun, 1995) 17848–17855.

[153] J. Stöhr, D. A. Outka, K. Baberschke, D. Arvanitis, and J. A. Horsley, *Identification of C-H resonances in the k-shell excitation spectra of gas-phase, chemisorbed, and polymeric hydrocarbons*, *Phys. Rev. B* **36** (1987) 2976–2979.

[154] E. Aziz, A. Vollmer, S. Eisebitt, W. Eberhardt, P. Pingel, D. Neher, and N. Koch, *Localized charge transfer in a molecularly doped conducting polymer*, *Adv. Mater.* **19** (2007), no. 20 3257–3260.

[155] D. Prendergast and G. Galli, *X-ray absorption spectra of water from first principles calculations*, *Phys. Rev. Lett.* **96** (2006) 215502.

[156] C. D. Pemmaraju, R. Copping, S. Wang, M. Janousch, S. J. Teat, T. Tyliszcak, A. Canning, D. K. Shuh, and D. Prendergast, *Bonding and charge transfer in nitrogen-donor uranyl complexes: Insights from NEXAFS spectra*, *Inorg. Chem.* **53** (2014), no. 21 11415–11425, [http://dx.doi.org/10.1021/ic501107a].

[157] J. S. Uejio, C. P. Schwartz, R. J. Saykally, and D. Prendergast, *Effects of vibrational motion on core-level spectra of prototype organic molecules*, *Chem. Phys. Lett.* **467** (2008) 195 – 199.

[158] C. P. Schwartz, J. S. Uejio, R. J. Saykally, and D. Prendergast, *On the importance of nuclear quantum motions in near edge X-ray absorption fine structure spectroscopy of molecules*, *J. Chem. Phys.* **130** (2009), no. 18 184109.

[159] M. Bagge-Hansen, B. C. Wood, T. Ogitsu, T. M. Willey, I. C. Tran, A. Wittstock, M. M. Biener, M. D. Merrill, M. A. Worsley, M. Otani, C.-H. Chuang, D. Prendergast, J. Guo, T. F. Baumann, T. van Buuren, J. Biener, and J. R. I. Lee, *Potential-induced electronic structure changes in supercapacitor electrodes observed by in operando soft X-ray spectroscopy*, *Adv. Mater.* **27** (2015), no. 9 1512–1518.

[160] B. J. Schultz, V. Lee, J. Price, C. Jaye, P. S. Lysaght, D. A. Fischer, D. Prendergast, and S. Banerjee, *Near-edge x-ray absorption fine structure spectroscopy studies of charge redistribution at graphene/dielectric interfaces*, *J. Vac. Sci. Technol. B* **30** (2012), no. 4 041205.

[161] A. H. England, A. M. Duffin, C. P. Schwartz, J. S. Uejio, D. Prendergast, and R. J. Saykally, *On the hydration and hydrolysis of carbon dioxide*, *Chem. Phys. Lett.* **514** (2011), no. 46 187 – 195.

[162] P. Jiang, D. Prendergast, F. Borondics, S. Porsgaard, L. Giovanetti, E. Pach, J. Newberg, H. Bluhm, F. Besenbacher, and M. Salmeron, *Experimental and theoretical investigation of the electronic structure of Cu2O and CuO thin films on Cu(110) using X-ray photoelectron and absorption spectroscopy*, *J. Chem. Phys.* **138** (2013), no. 2 –.

[163] J. P. Perdew, K. Burke, and M. Ernzerhof, *Generalized gradient approximation made simple*, *Phys. Rev. Lett.* **77** (1996) 3865–3868.

[164] A. J. Cohen, P. Mori-Sánchez, and W. Yang, *Fractional charge perspective on the band gap in density-functional theory*, *Phys. Rev. B* **77** (Mar, 2008) 115123.

[165] P. Mori-Sánchez, A. J. Cohen, and W. Yang, *Localization and delocalization errors in density functional theory and implications for band-gap prediction*, *Phys. Rev. Lett.* **100** (Apr, 2008) 146401.

[166] S. N. Patel, G. M. Su, C. Luo, M. Wang, L. A. Perez, D. A. Fischer, D. Prendergast, G. C. Bazan, A. J. Heeger, M. L. Chabinyc, and E. J. Kramer, *NEXAFS spectroscopy reveals the molecular orientation in blade-coated pyridal[2,1,3]thiadiazole-containing conjugated polymer thin films*, *Macromolecules* **48** (2015), no. 18 6606–6616, [http://dx.doi.org/10.1021/acs.macromol.5b01647].

[167] J.-L. Brédas, D. Beljonne, and V. C. J. Cornil, *Charge-transfer and energy-transfer processes in pi-conjugated oligomers and polymers: A molecular picture*, *Chem. Rev.* **104** (2004) 4971–5004, [http://dx.doi.org/10.1021/cr040084k].

[168] J. Ma, S. Li, , and Y. Jiang, *A time-dependent DFT study on band gaps and effective conjugation lengths of polyacetylene, polyphenylene, polypentafulvene, polycyclopentadiene, polypyrrole, polyfuran, polysilole, polyphosphole, and polythiophene*, *Macromolecules* **35** (2002), no. 3 1109–1115, [http://dx.doi.org/10.1021/ma011279m].

[169] T. Huser, M. Yan, and L. J. Rothberg, *Single chain spectroscopy of conformational dependence of conjugated polymer photophysics*, *Proc. Natl. Acad. Sci.* **97** (2000), no. 21 11187–11191, [http://www.pnas.org/content/97/21/11187.full.pdf].

[170] R. H. Friend, D. D. C. Bradley, and P. D. Townsend, *Photo-excitation in conjugated polymers*, *J. Phys. D: Appl. Phys.* **20** (1987), no. 11 1367.

[171] R. S. Kularatne, H. D. Magurudeniya, P. Sista, M. C. Biewer, and M. C. Stefan, *Donor-acceptor semiconducting polymers for organic solar cells*, *J. Polym. Sci. A Polym. Chem.* **51** (2013), no. 4 743–768.

[172] M. Oehzelt, S. Berkebile, G. Koller, J. Ivanco, S. Surnev, and M. Ramsey, *Sexithiophene on Cu(110) and Cu(110)-(2x1)O: An STM and NEXAFS study*, *Surf. Sci.* **603** (2009), no. 2 412 – 418.

[173] L.-L. Chua, M. Dipankar, S. Sivaramakrishnan, X. Gao, D. Qi, A. T. S. Wee, , and P. K. H. Ho, *Large damage threshold and small electron escape depth in X-ray absorption spectroscopy of a conjugated polymer thin film*, *Langmuir* **22** (2006), no. 20 8587–8594, [http://dx.doi.org/10.1021/la060974q].

[174] C. H. Woo, P. M. Beaujuge, T. W. Holcombe, O. P. Lee, and J. M. J. Fréchet, *Incorporation of furan into low band-gap polymers for efficient solar cells*, *J. Am. Chem. Soc.* **132** (2010), no. 44 15547–15549, [http://dx.doi.org/10.1021/ja108115y].

[175] I. E. Brumboiu, A. Anselmo, B. Brena, A. Dzwilewski, K. Svensson, and E. Moons, *Near-edge X-ray absorption fine structure study of the C60-derivative PCBM*, *Chem. Phys. Lett.* **568 - 569** (2013) 130 – 134.

[176] T. Schuettfort, S. Huettner, S. Lilliu, J. E. Macdonald, L. Thomsen, and C. R. McNeill, *Surface and bulk structural characterization of a high-mobility electron-transporting polymer*, *Macromolecules* **44** (2011), no. 6 1530–1539, [http://dx.doi.org/10.1021/ma102451b].

[177] D. Fazzi, M. Caironi, and C. Castiglioni., *Quantum-chemical insights into the prediction of charge transport parameters for a naphthalenetetracarboxydiimide-based copolymer with enhanced electron mobility*, *J. Am. Chem. Soc.* **133** (2011), no. 47 19056–19059, [http://dx.doi.org/10.1021/ja208824d].

[178] M. Grell, M. Redecker, K. S. Whitehead, D. D. C. Bradley, M. Inbasekaran, and E. P. Woo, *Monodomain alignment of thermotropic fluorene copolymers*, *Liq. Cryst.* **26** (1999), no. 9 1403–1407, [http://dx.doi.org/10.1080/026782999204084].

[179] H. Sirringhaus, R. J. Wilson, R. H. Friend, M. Inbasekaran, W. Wu, E. P. Woo, M. Grell, and D. D. C. Bradley, *Mobility enhancement in conjugated polymer field-effect transistors through chain alignment in a liquid-crystalline phase*, *Appl. Phys. Lett.* **77** (2000), no. 3 406–408.

[180] L. H. Jimison, M. F. Toney, I. McCulloch, M. Heeney, and A. Salleo, *Polymer charge transport: Charge-transport anisotropy due to grain boundaries in directionally crystallized thin films of regioregular poly(3-hexylthiophene)*, *Adv. Mater.* **21** (2009), no. 16 1568–1572.

[181] L. Biniek, S. Pouget, D. Djurado, E. Gonthier, K. Tremel, N. Kayunkid, E. Zaborova, N. Crespo-Monteiro, O. Boyron, N. Leclerc, S. Ludwigs, and M. Brinkmann, *High-temperature rubbing: A versatile method to align conjugated polymers without alignment substrate*, *Macromolecules* **47** (2014), no. 12 3871–3879, [http://dx.doi.org/10.1021/ma500762x].

[182] D. M. DeLongchamp, R. J. Kline, Y. Jung, D. S. Germack, E. K. Lin, A. J. Moad, L. J. Richter, M. F. Toney, M. Heeney, and I. McCulloch, *Controlling the orientation of terraced nanoscale ribbons of a poly(thiophene) semiconductor*, *ACS Nano* **3** (2009), no. 4 780–787, [http://dx.doi.org/10.1021/nn800574f].

[183] H.-R. Tseng, H. Phan, C. Luo, M. Wang, L. A. Perez, S. N. Patel, L. Ying, E. J. Kramer, T.-Q. Nguyen, G. C. Bazan, and A. J. Heeger, *High-mobility field-effect transistors fabricated with macroscopic aligned semiconducting polymers*, *Adv. Mater.* **26** (2014), no. 19 2993–2998.

[184] L. Ying, B. B. Y. Hsu, H. Zhan, G. C. Welch, P. Zalar, L. A. Perez, E. J. Kramer, T.-Q. Nguyen, A. J. Heeger, W.-Y. Wong, and G. C. Bazan, *Regioregular pyridal[2,1,3]thiadiazole ∂i-conjugated copolymers*, *J. Am. Chem. Soc.* **133** (2011), no. 46 18538–18541, [http://dx.doi.org/10.1021/ja207543g].

[185] H. Sirringhaus, *Device physics of solution-processed organic field-effect transistors*, *Adv. Mater.* **17** (2005), no. 20 2411–2425.

[186] Z. Bao and J. Locklin, *Organic Field-Effect Transistors.* CRC Press, 2007.

[187] T. Warwick, H. Ade, D. Kilcoyne, M. Kritscher, T. Tylisczcak, S. Fakra, A. Hitchcock, P. Hitchcock, and H. Padmore, *A new bend-magnet beamline for scanning transmission X-ray microscopy at the Advanced Light Source*, *J. Synchrotron Radiat.* **9** (2002), no. 4 254–257.

[188] A. L. D. Kilcoyne, T. Tyliszczak, W. F. Steele, S. Fakra, P. Hitchcock, K. Franck, E. Anderson, B. Harteneck, E. G. Rightor, G. E. Mitchell, A. P. Hitchcock, L. Yang, T. Warwick, and H. Ade, *Interferometer-controlled scanning transmission X-ray microscopes at the Advanced Light Source*, *J. Synchrotron Radiat.* **10** (2003), no. 2 125–136.

[189] W. Ma, J. R. Tumbleston, L. Ye, C. Wang, J. Hou, and H. Ade, *Quantification of nano- and mesoscale phase separation and relation to donor and acceptor quantum efficiency, Jsc, and FF in polymer:fullerene solar cells*, *Adv. Mater.* **26** (2014), no. 25 4234–4241.

[190] J. Als-Nielsen and D. McMorrow, *Elements of Modern X-ray Physics.* Wiley, 2 ed., 2011.

[191] J. Daillant and A. Gibaud, eds., *X-ray and Neutron Reflectivity.* Springer, Berlin Heidelberg, 2009.

[192] M. J. Frisch, G. W. Trucks, H. B. Schlegel, G. E. Scuseria, M. A. Robb, J. R. Cheeseman, G. Scalmani, V. Barone, B. Mennucci, G. A. Petersson, H. Nakatsuji, M. Caricato, X. Li, H. P. Hratchian, A. F. Izmaylov, J. Bloino, G. Zheng, J. L. Sonnenberg, M. Hada, M. Ehara, K. Toyota, R. Fukuda, J. Hasegawa, M. Ishida, T. Nakajima, Y. Honda, O. Kitao, H. Nakai, T. Vreven, J. A. Montgomery, Jr., J. E. Peralta, F. Ogliaro, M. Bearpark, J. J. Heyd, E. Brothers, K. N. Kudin, V. N. Staroverov, R. Kobayashi, J. Normand, K. Raghavachari, A. Rendell, J. C. Burant, S. S. Iyengar, J. Tomasi, M. Cossi, N. Rega, J. M. Millam, M. Klene, J. E. Knox, J. B. Cross, V. Bakken, C. Adamo, J. Jaramillo, R. Gomperts, R. E. Stratmann, O. Yazyev, A. J. Austin, R. Cammi, C. Pomelli, J. W. Ochterski, R. L. Martin, K. Morokuma, V. G. Zakrzewski, G. A. Voth, P. Salvador, J. J. Dannenberg, S. Dapprich, A. D. Daniels, . Farkas, J. B. Foresman, J. V. Ortiz, J. Cioslowski, and D. J. Fox, "Gaussian 09 revision d.01." Gaussian Inc. Wallingford CT 2009.